SIMULATION OF OPTICAL DIPOLE TRAPPING OF COLD CO MOLECULES

Doctoral Candidate

Maurizio Verde

Supervisor

Dr. Gabriele Santambrogio

Coordinator

Prof. Francesco Cataliotti

2016/2019

Contents

Abstract

Ultracold matter offers a unique capability to probe fundamental physics and to develop new quantum technologies. In this perspective, ultracold molecules are extremely attractive, thanks to their complex spectra and their large electric dipole moment. They are expected to have a fundamental impact on many fields of fundamental science, ranging from particles physics beyond the standard model, to ultracold chemistry and novel quantum phases in many-body complex quantum systems. At the same time, they promise impressive advances as platforms for long-range quantum simulators or quantum processors. Despite these appealing horizons, up to date only few molecular species have been produced down to the ultracold regime and none of them have been so far optically trapped in their absolute ground state, in the perspective of sympathetic cooling with widely available ultracold atoms. In this thesis we explore the feasibility of a new method of producing ultracold molecules. We focus on the very appealing idea to load ground state CO molecules into an optical dipole trap realized by a high power laser, given our expertise to load CO molecules produced via supersonic cooling into a chip Stark decelerator. The idea is to use this decelerator in combination with an electric field barrier to stop molecules in the vacuum, where they are driven to their absolute ground state and then trapped in the focal spot of a high-power laser. The optical dipole trap could be therefore used as an effective optical tweezer to put cold trapped molecules within a sample of ultracold atoms. Here, we aim to discuss the experimental feasibility of this optical trapping scheme as a first step towards sympathetic cooling. We develop complex simulations to explore how the different experimental parameters affect the trapping probability, in order to find the optimal conditions under which to perform the experiment.

Chapter 1

Ultracold molecules for new physics and technology

1.1 Fundamental science

High-precision measurements have always played a leading role in the discovery of new physics, by revealing tiny deviations between theoretical predictions and experimental data. Atomic spectroscopy led to the discovery of new structures and phenomena, such as the fine and hyperfine structures, the Lamb shift and the Stark and Zeeman effects, and from its birth its precision and accuracy never stopped to increase. During the last decades, the advent of laser cooling techniques led to the widespread availability of ultracold atoms, which in turn gave rise to an astonishing improvement of atomic spectroscopy. For example, it led to some of the current most precise measurements of fundamental constants of nature [1–8] with strict constraints on their possible time variations [9–13]. Further, it tested quantum electrodynamics (QED), a cornerstone of the standard model of particle physics, which is now one of the most stringently tested theories in modern physics. The success of atomic high-precision spectroscopy triggered the interest for the use of molecules. However, their much more complex spectra generally prevent laser cooling, which requires closed two-levels systems to extract thermal energy. Therefore, spectroscopic measurements for molecules are worse by more than three orders of magnitudes, as compared to those obtained by atoms, which at present reach relative accuracies of parts in 10^{18} [14].

1.1.1   High-precision spectroscopy

High-resolution molecular spectroscopy measures the energy states, in order to compare them with the theoretical predictions based on the single molecule Hamiltonian. The molecular density is therefore required to be sufficiently low, so that each molecule can be considered as an isolated system.

Molecules are already used for the most sensitive tests of the magnitude of the electron electric dipole moment (EDM) [15]. The interaction between the electron EDM and the extremely large internal electric field of fully polarized molecules is about five orders of magnitude greater than what is achievable in atoms. Interferometric techniques involving such interaction energy can therefore infer a constraint on the value of the electron EDM. Its determination appears particularly interesting since its non-vanishing value would result in a violation of the time-inversion symmetry and consequently a violation of CP symmetry, if the CPT theorem is assumed to hold. Therefore, a non-zero value of electron EDM would have a huge impact on the physics beyond the standard model, for example by explaining the amount of matter-antimatter asymmetry observed in the universe [15–20].

Further, molecular spectra are highly sensitive to two fundamental dimensionless constants, the fine-structure constant $\alpha = \frac{e^2}{\hbar c}$ and the electron-to-proton mass ratio $\beta = \frac{m_e}{m_p}$. The first governs the strength of electromagnetic interaction. The second depends on the strength of strong interaction because the proton mass results from the interaction between their elementary building blocks: gluons and quarks. Electronic and vibrational transitions involve, respectively, the fine-structure constant and the electron-to-proton mass ratio, so that when both kinds of transitions are probed at the same time, one is essentially comparing clocks built from two fundamentally different interactions. It is therefore interesting to assess whether α, β or their ratio depends on time [21, 22]. Another intriguing topic is that of parity violation. It can be addressed by measuring the energy shifts arising from the weak interaction between electrons and nuclei, and ultracold diatomic molecules have been proposed as excellent candidates due to the enhanced sensitivity of their rovibrational spectra to nuclear effects [23, 24]. Otherwise, the same issue can be studied by using chiral molecules, which are expected to show a small difference between the spectra of their enantiomers [25].

1.1.2   Ultracold chemistry

Ultracold atoms allowed for the discovery of Feshbach resonances, by which cross sections in atomic gases can be manipulated by using external magnetic field [26–30]. Basically, the

effect of magnetic field on atomic energy dominates on the translational energy. Therefore, their scattering cross sections can be controlled and largely enhanced by quantum threshold phenomena, which manifest as quantum tunneling-induced reactions. Likewise, but with many more degrees of freedom, scattering cross sections between ultracold molecules could be controlled with static and optical fields by various mechanisms. For example, it has been shown that molecule–molecule scattering at ultracold regime is dominated by magnetically tunable zero-energy scattering resonances, similar to the Feshbach ones [31]. Moreover, as the density of these molecular resonances is large and their properties change with the internal excitation of molecules, one can expect that ultracold molecules could be ideal candidates for studies of controlled chemistry, with the development of novel tools to control chemical reactions. Ultracold molecules may then have a broad impact on the study of chemistry in a completely new way, which could enable the characterization and control of molecular interactions with unprecedented precision and which may potentially lead to fundamental discoveries.

1.1.3 Condensed matter

Ultracold atoms revolutionized condensed matter physics by means of Bose-Einstein condensates and degenerate Fermi gases. Molecules, especially polar molecules with permanent electric dipole moments, have unique perspectives as systems with long-range and anisotropic interactions, in sharp contrast to the short-range interaction of Bose-Einstein condensates and degenerate Fermi gases. The strong dipole-dipole interaction between polar molecules adds new aspects to the physics of ultracold quantum matter, thus providing the opportunity to study novel many-body quantum systems. Moreover, their dipole moments could be controlled by external electric fields, allowing to tune interactions between molecules. For example, by tuning the interaction between ultracold polar molecules arranged in an optical lattice potential, one could control a rich set of quantum phases or even create new types of quantum phases, as super-solids systems [32, 33]. Moreover, if ultracold fermionic molecules are considered, one could study novel molecular superfluids [34, 35] or engineer effective spin–spin interactions [36, 37]. All these possibilities could led to discovery new phenomena in condensed matter physics and they could be the basis to create highly versatile quantum platforms with tunable behaviour useful for quantum simulators.

1.2 Technological interest

Molecular rovibrational structure leads to long coherence time and high electric dipole moments give rise to strong, long-range, anisotropic dipole interactions, which can be finely tuned by using external electric fields. These features make molecules excellent candidates to implement highly flexible quantum simulators and quantum computers. The first idea of quantum simulator comes from Feynman [38], who proposed the idea of a universal quantum computer being able to simulate whatever quantum phenomena. Nowadays, in literature, the two terms quantum simulator and quantum computer generally refer to different topics. Quantum simulators usually refer to many-body quantum systems which simulate other complex quantum systems, while a quantum computer is just a quantum system, implementing a particular algorithm to solve a problem of interest.

1.2.1 Quantum simulator

In order to predict the behaviour or to understand the properties of many-body quantum systems one could perform simulations on a classical computer. However, because of their exceedingly complexity, many fully quantum aspects still remain inaccessible by classical computation. A possible solution comes from quantum simulators, which directly simulate many-body quantum systems rather than performing inefficient digital computations. Ultracold matter is generally needed to exploit purely quantum phenomena. Ultracold atoms can be used but they manifest great limits as they cannot simulate a large variety of condensed-matter models, because of their short-range contact interactions. Instead, the uniqueness of dipole interactions make ultracold polar molecules much more promising candidates and, thanks to their long-range, anisotropic and tunable dipole interaction, they have been proposed as key elements for quantum simulators. The idea is to use ultracold polar molecules in an optical lattice as an engineered system, in which, by changing external fields, its Hamiltonian is made to match that of the interesting many-body quantum system, in order to directly access its behaviour and properties [39–45].

1.2.2 Quantum information processing

The idea of a quantum computer is intellectually very attractive [46–48] and it promises huge computational advantages [49–51]. Its implementation relies on the availability of interacting qubits to process quantum information. Great expectations come from ultracold polar molecules, which have been suggested as ideal platform for quantum information

processing [52–56]. Ultracold polar molecules combine the advantages of atoms with new desirable features, including their long-lived rovibrational states, suitable to encode quantum information, and their long-range dipole interaction, useful for conditional logic operations, which require strong interactions between the constituent qubits. Their interaction can be then manipulated by using static, microwave or laser fields, whose precision technology is highly developed and can be integrated with microelectronic circuits. Thus, ultracold polar molecules could provide new tools for coherent quantum control beyond those available for atoms. For example, different molecules could be entangled by controlling the coupling between their internal states. Otherwise, as the speed of conditional logic operations is proportional to the strength of the interaction, their long-range, strong dipole coupling could lead to engineer fast logic gates between remote qubits, thus opening promising perspectives towards large networks of qubits.

1.3   Molecular cooling: the state of the art

When we speak of cold or ultracold matter, we are dealing to two different range of temperature, the first referring to temperature 1 mK $< T_c < 1$ K, while the second denoting lower temperature $T_{uc} < 1$ mK. So far, ultracold matter has been mostly obtained for atoms by using laser cooling techniques, which exploit their simple electronic structure to remove thermal energy by scattering photons. This method cannot easily be extended to molecules because of their complex rovibrational spectra, although huge progress in this direction has recently been reported.

1.3.1   Cold molecules

So far, most common techniques to prepare cold molecules are supersonic adiabatic cooling, buffer gas cooling and various kinds of molecular decelerators. The first two methods allow the production of very intense molecular beams cooled down to hundreds of mK, while molecular decelerators reach lower temperatures (few mK) with the drawback of a much smaller density.

Supersonic adiabatic cooling

The first cooling technique to reach temperatures below 1 K, was the supersonic adiabatic expansion, initially proposed in 1951 [57, 58]. As described in some details afterward in

this thesis, it consists of the cooling arising from the adiabatic expansion from a high-pressure chamber into the vacuum. Thermodynamics accounts for the conversion of the molecular internal energy into kinetic energy in such a way that the final result is a supersonic beam of cold molecules with a forward velocity between 200 and 900 m/s. The achievable translational temperature is down to 100 mK [59], while the rotational and vibrational temperatures are slightly higher. More precisely, rotational temperature is very effectively cooled down to about few K, while vibrations are less efficiently cooled. This method is widely available regardless of the considered molecular species, and we use it to produce a supersonic beam of CO molecules at a translational temperature of 220 mK.

Buffer gas cooling

Cryogenic buffer-gas cooling is a very general method. Molecules of any species are firstly produced by laser ablation of the relative target material inside a cryogenic cell, which is filled with a cold inert buffer-gas. Multiple elastic and inelastic scattering between the buffer-gas and the molecules rapidly cool their translational, vibrational and rotational degrees of freedom down to the buffer-gas temperature. Then, the buffer-gas flows out into vacuum, dragging with it molecules which are finally available in the form of molecular beams with a forward subsonic speed between 50 and 150 m/s. The natural choice for the buffer-gas is helium in both its stable isotope ^{4}He and ^{3}He, essentially because cold liquid helium is characterized by a large vapor pressure, which is needed for an efficient thermalization. This is particularly true for ^{3}He, which has a relevant vapor pressure even at very low temperature down to few hundreds of mK. The minimum temperature achievable by this technique is therefore about 300 mK, where even the ^{3}He vapor pressure begins to rapidly decrease to zero [60]. A great advantage of buffer-gas cooling is its widespread applicability to many molecular species. In fact, the only requirement is that molecules to be cooled survive multiple collisions with low-energy cold helium atoms. Furthermore, another advantage is the unique brightness of the beam, with high molecular densities strongly exceeding those possible with any other technique [61–65].

Deceleration techniques

In order to reach colder temperatures down to few mK, different kinds of adiabatic decelerators can be used. All of them rely on three dimensional traveling traps, which capture cold molecules from molecular beams previously produced via supersonic or buffer-gas

cooling. An ideal adiabatic decelerator slows down molecules without losses and heating, thereby conserving their initial phase space density. Therefore, it is not really a cooling technique, as it just selects the slice of molecular thermal distribution matching the trap acceptance and it merely slows down an already cold ensemble. As a consequence, the number of cold molecules is rather limited, but small samples with temperatures down to 1 mK $< T <$ 100 mK can be successfully prepared. In the past decade a wide variety of different molecular decelerators have been developed. Particularly important are the Stark decelerators [66–71], the Zeeman decelerators [72–76], and some other kinds based on optical fields [77, 78]. In the perspective of producing samples of ultracold molecules, decelerators are expected to be crucial. In fact, they can slow down molecules to velocities which allow trapping. In this thesis a microchip Stark decelerator, extremely suitable for polar CO molecules, is considered exactly in this perspective.

1.3.2   Ultracold regime

Many exciting experiments in fundamental science research and in new quantum technologies require ultracold molecules. So far, a general cooling technique is not available, but some particular molecular species showed promising results. For example, ultracold molecules have been prepared by assembling ultracold atoms, while other diatomic molecules have been recently laser cooled. Moreover, sympathetic cooling of molecular ions have been successfully performed and theoretical studies have been explored about some cases of ground state molecules.

Assembly from ultracold atoms

Some techniques allow to drive colliding ultracold atoms into ultracold molecules. So far most of experiments led to alkali-metal dimers and molecules formed from an alkali-metal atom and an alkaline-earth or Yb atom [79–81]. A first technique relies on Feshbach resonances, where an external magnetic field is exploited to drive ultracold atoms into molecules [82–87]. Essentially, a bound molecular state energy can be tuned by the external magnetic field to match the scattering energy of atoms, so that, by slowly varying the external field across the Feshbach resonance, atoms are adiabatically converted into molecules. A closely related method exploits Feshbach resonances followed by the so-called stimulated rapid adiabatic passage. With this technique ultracold atoms are converted to ultracold molecules, which are further coherently driven towards particular molecular states [88–95]. Otherwise, when molecules do not have readily accessible Feshbach reso-

nance, the photo-association technique can be used. Two colliding atoms absorb a photon to form an excited molecular state, whose energy is the sum of the kinetic energy of the colliding atoms and the photon energy. Therefore, the excited molecule spontaneously decays, giving rise to two atoms again, or producing a ground state molecule [96–100]. With these techniques best results yielded to ultracold molecules at temperature down to hundreds of nK. The drawback of this approach is that only very special kinds of molecules can be prepared.

Direct laser cooling

A radically different approach is the direct laser cooling of molecules. Apart from few exceptions, electronically excited molecules decay toward many different rovibrational levels of the electronic ground state and the lack of a closed two-level transition prevent direct laser cooling for most molecules. So far, molecular laser cooling has been demonstrated only for species featuring an unpaired electron that does not participate to the chemical bond. In these cases, unusually large overlap between the ground and excited rovibronic states yields to quasi-closed transitions [101]. Particular repumping schemes, involving more than just two states, have been proposed and successfully tested. In recent years, direct laser cooling evidenced promising advancing in the case of calcium monofluoride CaF [102–106], strontium monofluoride SrF [107–110] and yttrium monoxide YO [111, 112]. By direct laser cooling, YO has been cooled down to few mK, while CaF and SrF have been cooled down to, respectively, 50 μK and 300 μK.

Sympathetic cooling

A different approach, which is indifferent to the molecular electronic structure and thus potentially universal, is sympathetic cooling, where neutral molecules are cooled in a bath of ultracold atoms. In order to make molecules undergoing multiple scattering, they have to be trapped within the ultracold atom cloud. So far, this has been performed only for charged molecular ions by using very effective ion traps [113], while for neutral molecules no solutions have been found. Static electric and magnetic fields only trap low-field seeking molecules, which are never absolute ground states, so that inelastic collisions between molecules and the coolant are the major obstacle. Trapping the molecules in their absolute ground state would circumvent this problem, as they will never get lost because the inelastic channels are energetically prevented. However, their capturing via optical dipole trap or microwave trap is very challenging. Some theoretical works focused on

atom-molecule systems characterized by a large ratio between the cross section for elastic collisions, which produce thermalization, and that for inelastic collisions, which cause trap losses [114–117]. Conversely, in this thesis, we explore the experimental feasibility of an optical dipole trap for absolute ground state CO molecules, which have been firstly slowed down by a microstructured Stark decelerator.

1.4   Why CO molecules?

Carbon monoxide $^{12}C^{16}O$ polar molecules are in many ways extremely attractive for cooling and trapping experiments. They are bosons with no nuclear spin thus interesting in the perspective of molecular BECs. The non-degenerate rotational ground state $N = 0$ is well separated by more than 100 GHz to the next $N = 1$ rotational level and this provides that blackbody radiation, even at room temperature, pumps CO molecules out of their absolute ground state $X^1\Sigma^+ |v = 0, N = 0, +\rangle$ with a rate below 10^{-3} s^{-1} [118], making them ideal candidates for accumulation in any kind of trap. It is worth noting that, in their ground state, CO molecules experience a physical potential in AC electric fields very similar to that experienced by ground state ^{87}Rb atoms, so that some successfully developed trapping techniques [119–121] could be extended to cold absolute ground state CO molecules. Even more interesting, absolute ground state CO molecules could be optically trapped, thus offering unique advantages for sympathetic cooling towards ultracold polar molecules production. In this perspective, a scheme has been demonstrated aimed at producing translationally cold samples of ground-state CO molecules. It is based on two promising properties of CO molecules. On one side, electrostatic trapping and Stark deceleration are possible for their metastable $a^3\Pi_1$ state, by virtue of its high electric dipole moment, $\mu_e = 1.37$ Debye, and its quite long lifetime, $\tau = 2.63$ ms [122]. On the other side, a unidirectional optical pumping scheme, with a very high efficiency up to 28%, has been experimentally demonstrated from metastable $a^3\Pi_1$ state towards the absolute ground state $X^1\Sigma^+ |v = 0, N = 0, +\rangle$. The ability to Stark decelerate metastable CO molecules to a standstill point and pump them towards their absolute ground state is the basic idea proposed in [123]. In our laboratory we have a microstructured chip Stark decelerator successfully tested in many different experiments. From a supersonic beam, ground state CO molecules can be firstly excited to their metastable $a^3\Pi_1$ state and then loaded on the chip, where moving electrostatic microtraps decelerate them to the desired speed of few m/s by confining them within tubular-shape decelerating microtraps, whose typical energy depth is about few tens of mK while their typical length is around few tens

of μm. Surprisingly, the high-power laser available in our laboratory can be used as a dipole trap with an energy depth about 10 mK, provided that it is highly focused to few tens of μm. Such a matching between the chip microtrap features and the dipole trap requirements highly motivates the work presented throughout this thesis. Metastable CO molecules leaving the microstructured Stark decelerator can then be stopped by a strong DC electrical barrier, irreversibly transferred to their absolute ground state and finally captured in the optical trap. Such an optical dipole trap can be therefore used as an effective optical tweezer to put cold trapped ground state CO molecules within a sample of ultracold atoms. In this perspective, we discuss the experimental feasibility of such an optical trapping scheme as a first step towards sympathetic cooling. We simulate the whole cycle experiment, from the Stark deceleration up to the optical trapping, in order to find the best experimental conditions and predict the maximum loading rate for ground state CO molecules on the dipole trap.

1.5   Thesis organization

This thesis is structured as follows. In chapter (2), we describe the interaction between CO molecules and electromagnetic fields, in order to provide the basic theory underlying our simulations of the trapping experiment. Then, in chapter (3), we introduce the setup, required for such an experiment, and we present the observation of two molecular transitions, not yet reported in literature, which could be used in the experiment. Finally, in chapter (4) we present our simulations of optical dipole trapping and we discuss its experimental feasibility.

Chapter 2

Theory of CO molecules in electromagnetic fields

Here, we describe some theoretical aspects of molecular physics and light-matter interaction underlying high-precision spectroscopy measurements and quantum control of CO molecules, with particular attention to their interaction with external electromagnetic fields.

2.1 Energy shifts and quantum dynamics

Molecules are inherently complex quantum systems, possessing manifolds of closely spaced vibrational and rotational energy levels. In the presence of external electromagnetic fields, their spectra are modified and, thanks to the great development of different sources of coherent electromagnetic radiation, they can be finely probed by photons covering a huge range of frequencies from radio waves to far ultraviolet. A complete treatment of the interaction between molecules and electromagnetic fields is beyond the purposes of this thesis. We just summarize the most important aspects regarding the manipulation with electromagnetic fields for the external and internal molecular degrees of freedom involved in our experiments.

Molecules show two possible behaviours. When they interact with static electric or magnetic fields, their energy levels are shifted through the so-called DC Stark and Zeeman effects, respectively. In this case no quantum transition can occur. Otherwise, when they interact with time-dependent external fields, as electromagnetic radiation, the Hamiltonian is time-dependent and quantum transitions can be observed. However, when the

frequency of the electromagnetic radiation is far detuned from any quantum transition, it just perturbs the molecular energy levels, without inducing much population transfer, and this leads to the so-called polarizability potential. Conversely, if the frequency of the electromagnetic radiation matches the energy difference between two states, quantum dynamics can be induced via the so-called Rabi oscillations. Finally, for general time-varying electromagnetic fields the so-called non-adiabatic transitions can occur.

2.1.1 DC Stark effect

The DC Stark effect can be described in the framework of time–independent perturbation theory, which is useful to derive the corrections to the eigenstates and to the energy eigenvalues for a weakly perturbed quantum system. The free Hamiltonian $\hat{H}_0$ describes the unperturbed system, while the interaction Hamiltonian $\hat{H}_I$ represents the small external time-constant perturbations. The corrections, due to $\hat{H}_I$, to the eigenstates and eigenvalues of $\hat{H}_0$ can be established to a given order under the assumption that corrections of successive orders are always smaller. Here below, we report the formal expression for the first and the second order corrections to the free Hamiltonian eigenstates and eigenvalues. Then, we apply them to the specific case of DC Stark effect.

We denote by $|n\rangle$ the eigenstates of $\hat{H}_0$, with E_n their energy eigenvalues:

$$\hat{H}_0 \left| n^0 \right\rangle = E_n^{(0)} \left| n^0 \right\rangle. \tag{2.1}$$

The first order energy corrections are given by the expectation value of the interaction Hamiltonian in the unperturbed states:

$$E_n^{(1)} = \left\langle n^0 \middle| \hat{H}_I \middle| n^0 \right\rangle, \tag{2.2}$$

while the first order state corrections are given by the superposition of all the unperturbed states:

$$\left| n^1 \right\rangle = \sum_{m \neq n} \frac{\langle m^0 | \hat{H}_I | n^0 \rangle}{E_n^{(0)} - E_m^{(0)}} \left| m^0 \right\rangle. \tag{2.3}$$

We observe that the external perturbation mixes more effectively those states, whose energy is very similar and for which the interaction matrix element is significant.

The second order corrections to the energy mostly comes from the interaction between the considered level and the other closely spaced energy levels:

$$E_n^{(2)} = \sum_{m \neq n} \frac{|\langle m^0 | \hat{H}_I | n^0 \rangle|^2}{E_n^{(0)} - E_m^{(0)}}. \tag{2.4}$$

Now, let us summarize the main consequences of equations (2.2),(2.3) and (2.4) for what concerns our experiments with CO molecules. Unperturbed molecular eigenstates of diatomic CO molecules can be labelled by a definite set of quantum numbers $\{J, S, \Omega, \Lambda, \Sigma, M\}$ and they have a well defined parity $\pm$. Furthermore, the so-called Λ-doubling interaction breaks the degeneracy between two opposite parity states $|JS\Omega\Lambda\Sigma M\pm\rangle$ and leads to a fine splitting. Therefore, by considering the interaction with an external static electric field $\vec{E}$:

$$\hat{H}_{\text{DC Stark}} = -\hat{\vec{\mu}} \cdot \vec{E}, \tag{2.5}$$

we have two main consequences. The first is that the external electric field contributes to the energy shift of unperturbed eigenstates only at second order in perturbation theory. Indeed, as the dipole moment operator is odd under parity transformations and the eigenstates have a defined parity, the interaction Hamiltonian has vanishing diagonal matrix elements on the base of unperturbed molecular eigenstates:

$$\langle JS\Omega\Lambda\Sigma M\pm|\hat{H}_{Stark}|JS\Omega\Lambda\Sigma M\pm\rangle = 0. \tag{2.6}$$

Then, thanks to Λ-doubling splitting, which is much smaller than the energy difference between all the others eigenstates, the Eq. (2.3) and (2.4) greatly simplify respectively to:

$$|JS\Omega\Lambda\Sigma M\pm\rangle^{(1)} = \frac{\langle JS\Omega\Lambda\Sigma M\pm|\hat{H}_I|JS\Omega\Lambda\Sigma M\mp\rangle}{\Lambda} |JS\Omega\Lambda\Sigma M\pm\rangle, \tag{2.7}$$

and

$$E^{(2)}_{JS\Omega\Lambda\Sigma M\pm} = \frac{|\langle JS\Omega\Lambda\Sigma M\mp|\hat{H}_I|JS\Omega\Lambda\Sigma M\pm\rangle|^2}{\Lambda}, \tag{2.8}$$

where Λ denotes the Λ-doubling splitting. The above equations tell us that both the first order correction to the eigenstates and the second order correction to the eigenvalues, mostly depend on the matrix element of the DC Stark Hamiltonian between the two states of each Λ-doublet.

Now, we derive the matrix element for the DC Stark Hamiltonian between two Λ-doublet levels in the case of a diatomic molecule by following the semi-classical description reported in [124]. As explained before, CO molecules are well described by Hund's coupling case (a) for which the electronic motion is strongly coupled to the internuclear axis and the electric dipole moment is directed along this axis. To evaluate the amplitude $\langle JS\Omega\Lambda\Sigma M\mp|-\hat{\vec{\mu}} \cdot \vec{E}|JS\Omega\Lambda\Sigma M\pm\rangle$, we need to derive the effective electric dipole moment

μ_{eff} along the electric field $\vec{E}$. Among all the quantum numbers describing the unperturbed levels, it depends only on those regarding the overall molecular rotation and its component along both the external electric field $\vec{E}$ and the internuclear axis, where the electric dipole moment lies. Then, we consider only the total molecular angular momentum J, its projection over the inter nuclear axis Ω and its projection over the quantization axis M. The average electric dipole moment along the total angular momentum is

$$\mu_J = |\vec{\mu}| \cos\left(\vec{\mu}, \vec{J}\right) = |\vec{\mu}| \frac{\Omega}{|\vec{J}|}, \tag{2.9}$$

and by taking its projection over the quantization axis, which corresponds to the electric field axis, we obtain

$$\mu_E = \mu_J \cos\left(\vec{J}, \vec{E}\right) = \mu_J \frac{M}{|\vec{J}|}. \tag{2.10}$$

Therefore, we reach the semi-classical estimation for the matrix element by substituting Eq. (2.9) within (2.10)

$$\langle JS\Omega\Lambda\Sigma M\mp | -\hat{\vec{\mu}} \cdot \vec{E} | JS\Omega\Lambda\Sigma M\pm \rangle = -\mu_E |\vec{E}| = -|\vec{\mu}||\vec{E}| \frac{M\Omega}{J(J+1)}. \tag{2.11}$$

Finally, by using this expression within Eq. (2.7) and (2.8) the first order correction comes from the mixing with the opposite parity state

$$|JS\Omega\Lambda\Sigma M\pm\rangle^{(1)} = -\frac{|\vec{\mu}||\vec{E}|}{\Lambda} \frac{M\Omega}{J(J+1)} |JS\Omega\Lambda\Sigma M\pm\rangle, \tag{2.12}$$

and the second order correction to the energy levels

$$E^{(2)}_{JS\Omega\Lambda\Sigma M\pm} = \frac{|\vec{\mu}|^2 |\vec{E}|^2}{\Lambda} \left(\frac{M\Omega}{J(J+1)}\right)^2. \tag{2.13}$$

As we see, DC Stark interaction mixes levels of opposite parity and leads to energy shift only for Λ-doublets with non-vanishing values of M and Ω.

The above results can be obtained also by following another way. Once established that only two levels, belonging to each Λ-doublet, significantly contribute to DC Stark effect, we can study the following two-levels Hamiltonian

$$\hat{H}_{Stark} = \begin{pmatrix} \frac{\Lambda}{2} & -|\vec{\mu}||\vec{E}|\frac{M\Omega}{J(J+1)} \\ -|\vec{\mu}||\vec{E}|\frac{M\Omega}{J(J+1)} & -\frac{\Lambda}{2} \end{pmatrix}, \tag{2.14}$$

where we have arbitrarily chosen the zero energy in the middle between the two Λ-doublet components. By diagonalizing the above matrix we obtain the new eigenvalues:

$$\lambda_\pm = \pm \sqrt{\left(\frac{\Lambda}{2}\right)^2 + |\vec{\mu}|^2 |\vec{E}|^2 \left(\frac{M\Omega}{J(J+1)}\right)^2} = \pm \left(\frac{\Lambda}{2} + \frac{|\vec{\mu}|^2 |\vec{E}|^2}{\Lambda} \left(\frac{M\Omega}{J(J+1)}\right)^2\right) + o(|\vec{E}|^3),$$

(2.15)

where we recognize the same results of Eq. (2.13) if we take their Taylor expansion up to second order in the power of electric field strength.

Finally, we apply these results to the particular quantum state of CO molecules involved in our experiments, namely the excited meta-stable state $a^3\Pi_1$ $|v=0, J=1, +\rangle$. The permanent electric dipole moment is $|\vec{\mu}| = 1.375$ Debye [125] and the zero-field energy difference in the Λ-doublet is 394 MHz. The total angular momentum quantum number is $J=1$, thus there are only three possible values for its projection $M=0, \pm 1$, which are degenerate if no magnetic field perturbs the molecule. The $M=0$ component has no Stark shift, while both components $M=\pm 1$ are Stark shifted and they remain degenerate. Their upper states, with positive parity, are low-field seeking states as their energies increases with higher electric fields, while the lower states, with negative parity, are high-field seeking states as their energies decreases for growing electric fields, as shown in Fig. (2.1).

A homogeneous electric field mixes the Λ-doublet components and this modifies the intensity for the measured spectra. Instead, inhomogeneous electric fields lead to the broadening of spectral lines for $M=\pm 1$ states.

To conclude, we highlight the limit on the electric field strength under which the above treatment is consistent. In the case of CO molecules in the $a^3\Pi_1$, for very high electric fields ($\vec{E} \gg \frac{\Lambda}{2|\vec{\mu}|}$ above 100 $\frac{\text{kV}}{\text{cm}}$) states with increasing energies from one rotational level approach states with decreasing energies from the next rotational level. When this occurs, both levels undergo the so-called self-avoided crossing and their behaviour greatly deviates from the derived equations. However, in our experimental setup we never reach such extreme conditions.

2.1.2 Zeeman interaction

Magnetic fields, similarly to electric fields, generally lead to splitting, shifts and broadening phenomena affecting molecular spectra and therefore influencing high-precision spectroscopy measurements. Thus, a basic understanding of the interaction between molecules
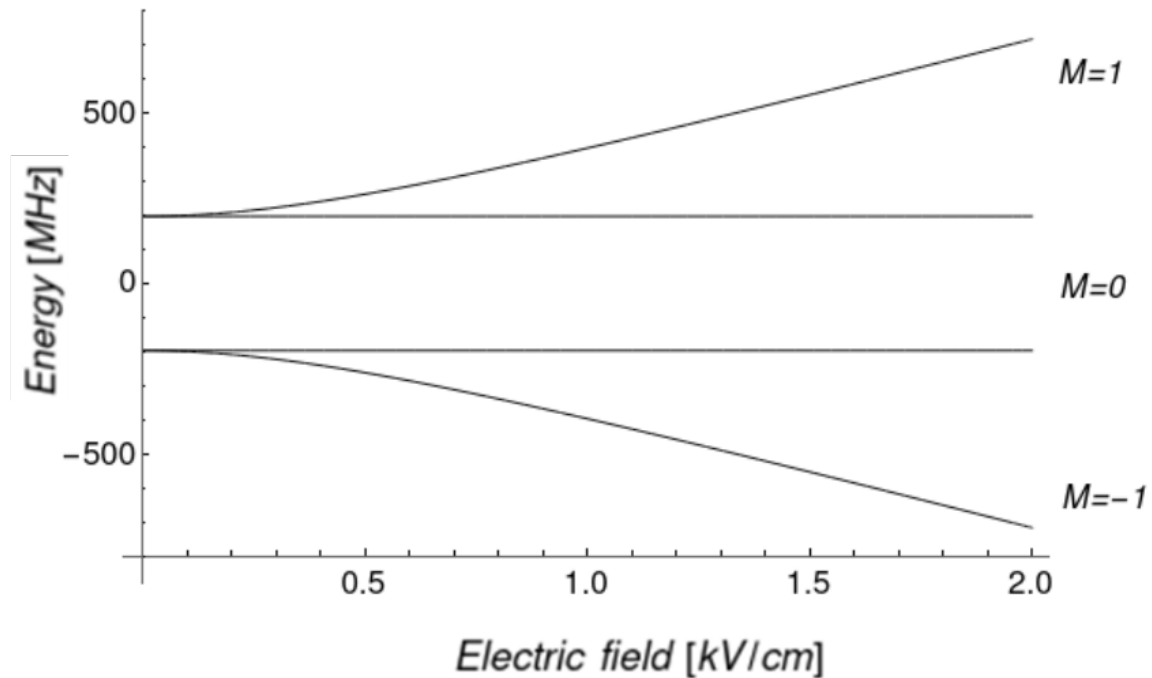
Figure 2.1: DC Stark shift for the positive and negative parity components with $M=0,\pm1$, belonging to the first electronically excited state $a^3\Pi_1 \left|v = 0, J = 1\right\rangle$ of CO molecules. The upper level with positive parity is a low-field seeking state, while the lower odd parity component is a high-field seeking state. Both opposite parity components with $M=0$ show no dependence on the electric field strength.

and magnetic fields is needed to design spectroscopy experiments as well as to manipulate and control their external and internal degrees of freedom. Here below, we report the main aspects of this interaction, focusing on the particular case of CO molecules.

From a very general point of view, an external magnetic field $\vec{B}$ destroys the isotropy of free space. The degeneracy between different orientations of the molecule is broken and these different states acquire distinct energies in the magnetic field. This phenomenon is referred as the Zeeman splitting. It depends on the interaction between charged particles, with definite spin and orbital angular momenta, and the external magnetic field. Within molecules, both electrons and nuclei interact with magnetic fields but, as nuclei have a larger mass, they generally lead to very weak corrections. We neglect their effects and we only focus on the electron contributions.

As derived in many textbooks [126, 127], for multi-electron systems like molecules, the interaction Hamiltonian resulting from the two contributions of the electron orbital

angular momentum $\hat{L}$ and the electron spin angular momentum $\hat{S}$ is the following:

$$\hat{H}_{\text{Zeeman}} = -\hat{\vec{\mu}}_M \cdot \vec{B} = \mu_{\text{B}} \left(g_L \hat{L} + g_S \hat{S} \right) \cdot \vec{B}, \tag{2.16}$$

where μ_{B} is the Bohr magneton, while g_L and g_S are, respectively, the electron orbital and spin gyromagnetic factors. As we are not focused on high-precision Zeeman spectroscopy, we use their approximated values $g_L = 1$ and $g_S = 2$, neglecting their quantum electrodynamics corrections.

By comparing the Zeeman Hamiltonian with the DC Stark Hamiltonian defined in Eq. (2.5), we immediately notice that they seem quite similar, as both involve a scalar product between external magnetic or electric field, on one side, and the magnetic or the electric dipole moment operator on the other. Despite their formal analogy, their effects on molecular spectra are different. We know that, being it defined by the cross product of two vectors, the magnetic field $\vec{B} = \vec{\nabla} \times \vec{A}$ is a pseudovector, which does not change under parity transformations:

$$\hat{\mathcal{P}}: \quad \vec{B} \; \to \; \vec{B}. \tag{2.17}$$

In order for the quantity $\hat{\vec{\mu}}_M \cdot \vec{B}$ to be invariant under parity inversion, as it is by definition any scalar product, the magnetic moment operator $\hat{\vec{\mu}}_M$ must also be invariant under such a transformation:

$$\hat{\mathcal{P}}: \quad \hat{\vec{\mu}}_M \; \to \; \hat{\vec{\mu}}_M. \tag{2.18}$$

We use this property to present the effects of magnetic field on molecular spectra, within the framework of time-independent perturbation theory, thus referring to Eqs. (2.2), (2.3) and (2.4). All the effects depend on the matrix elements of the magnetic dipole moment operator evaluated on the basis of the unperturbed molecular eigenstates. Because they have a well defined parity and the magnetic dipole moment is an even operator, only its matrix element between states with the same parity are non-zero and the magnetic field induced couplings appear in first order perturbation theory. Its diagonal elements lead to first order corrections to unperturbed energies, then showing a linear dependence on the magnetic field strength, in contrast to quadratic dependence of DC Stark shift shown by Eq. (2.13).

Let us see the explicit expression for the first order Zeeman shift in the case of CO molecules. As reported in [128, 129] the magnetic dipole operator $\hat{\vec{\mu}}_M$ for diatomic molecules which are described by the Hund's case (a), can be rewritten by the following

expression:

$$\hat{\vec{\mu}}_M = \mu_B \left(g_L \hat{L} + g_S \hat{S} \right) = -g_J^{(a)} \mu_B \hat{J}, \tag{2.19}$$

where $g_J^{(a)}$ is the so-called Landé gyromagnetic factor in a Hund's case (a) representation, which takes the following form:

$$g_J^{(a)} = \frac{(g_L \Lambda + g_S \Sigma) \Omega}{J(J+1)}. \tag{2.20}$$

Therefore, by choosing the quantization axis along the external magnetic field $\vec{B}$, we obtain the first order Zeeman correction to the zero-field eigenstates:

$$E_{JS\Omega\Lambda\Sigma M\pm}^{(1)} = \langle JS\Omega\Lambda\Sigma M\pm| -\hat{\vec{\mu}}_M \cdot \vec{B}|JS\Omega\Lambda\Sigma M\pm\rangle = g_J^{(a)} \mu_B M|\vec{B}|. \tag{2.21}$$

Finally, for the CO molecules in the $a^3\Pi_1$ state, namely with $\Lambda = 1$, $\Sigma = 0$, $\Omega = 1$ and in the rotational level $J = 1$, the above expression simplifies to:

$$E_B^{(1)} = \frac{1}{2}\mu_B M|\vec{B}|, \tag{2.22}$$

so that each state is Zeeman splitted in three states, corresponding to the three values of the angular momentum projection quantum number $M = 0, \pm1$. The above approximated analytical formula fits very well calculations involving higher orders corrections in perturbation theory, as shown in Fig. (2.2). Another consequence of Eq. (2.19) is that, at first approximation, Zeeman interaction does not mix eigenstates with different magnetic number M, as the magnetic dipole moment operator is diagonal on them. Therefore, in sharp contrast with Stark effect, magnetic field induced quantum mixing is expected to be very small, as all the closest levels within the Λ-doublet cannot contribute.

Finally, it is interesting to describe some consequences of the presence of an external electric field perpendicular, or just not perfectly parallel, to the external magnetic field. In this case, as long as the Stark interaction is weaker than the Zeeman one, the eigenstates still have a well-defined magnetic quantum number M, since the magnetic field dominates molecular alignment, and the described Zeeman splitting still remains. However, when the electric field strength grows enough, molecules reorient themselves along the electric field direction and their eigenstates loose a definite magnetic number M along the magnetic field direction. Then, for increasing electric fields, states with different magnetic numbers M are even more effectively mixed up so that no Zeeman structure appears, as shown in the case of CO molecules in Fig. (2.3).

A precise understanding of Zeeman effect is essential to correctly analyse the observed molecular spectra in the presence of magnetic fields and to predict the shifts of spectral
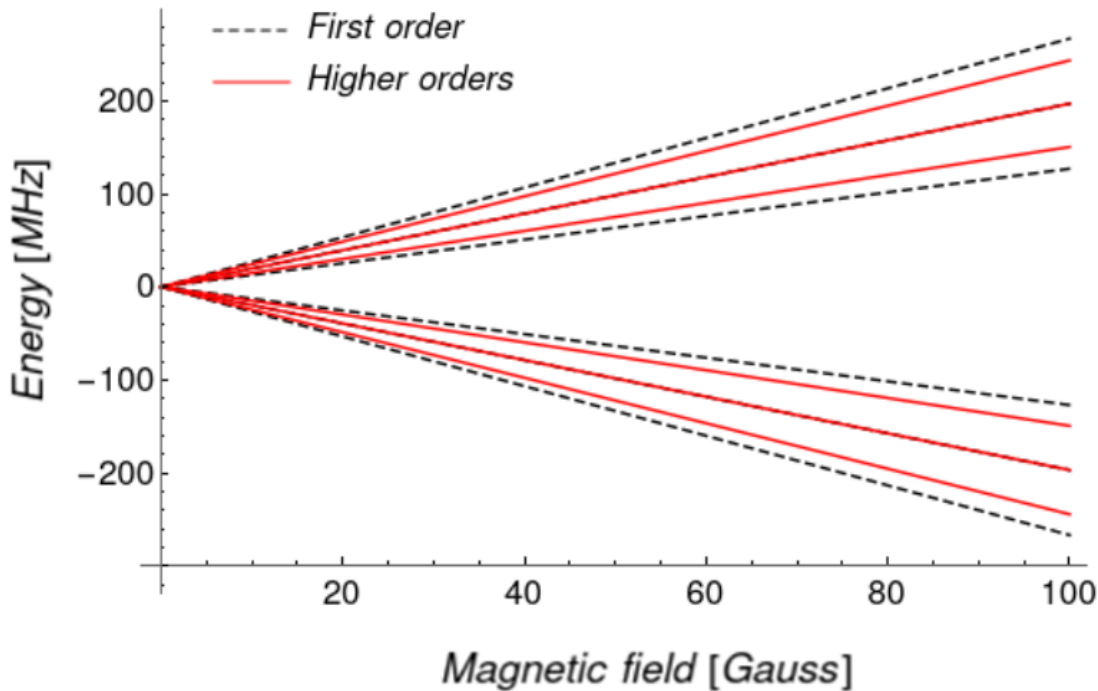
Figure 2.2: Zeeman splitting predicted at first order in perturbation theory (black dashed lines) and at higher orders in perturbation theory (red lines). Calculations regard CO molecules for both components of the Λ-doublet within the $a^3\Pi_1 |v = 0, J = 1\rangle$ state. Specifically, the lower three states represent the Zeeman splitting of the odd parity component, while the upper states represent the positive parity one. Each parity component splits in three levels for which the lowest, the middle and the higher ones correspond, respectively, to magnetic quantum number M=-1,0,+1. The energy zero has been taken arbitrarily in the middle between two parity components at zero field. We show these predictions up to 100 Gauss, as in our experiments no higher magnetic field is produced.

lines or their broadening arising from inhomogeneous magnetic fields. Moreover, from the point of view of molecular control, as we will describe in the next chapter, magnetic fields under specific conditions can prevent the undesired appearance of non-adiabatic losses. In general, the Zeeman as well as the Stark effects are essential ingredients to be considered in order to design high-precision spectroscopic measurements and molecular trapping or quantum control experiments.
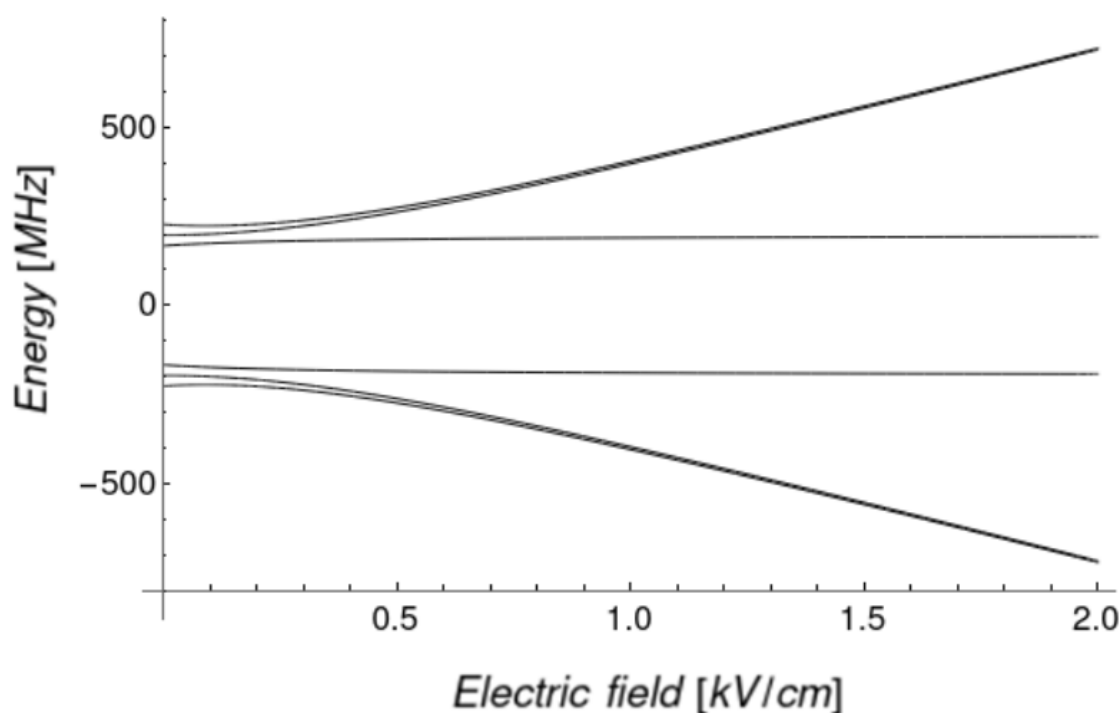
Figure 2.3: DC Stark shift for CO molecules in the $a^3\Pi_1$ $|v = 0, J = 1\rangle$ state, in the presence of a 50 Gauss magnetic field perpendicular to the electric field. For small electric field strength values, there is the expected Zeeman structure, while for higher values it is washed up, as the magnetic numbers $M = 0, \pm 1$ of the levels are no more well-defined because they are mixed up by the electric field.

2.1.3 Optical Block equations

Time-dependent Hamiltonians generally lead to population transfer phenomena and molecules can transit between different quantum states. Under specific conditions, such a perturbation can be used to drive quantum dynamics in a controlled way. To reach this goal, we should be able to produce a sample of molecules lying in the same quantum state and interacting with laser fields for longer times as those characterizing the induced quantum dynamics. Indeed, when a laser field interacts with a sample of molecules in different quantum states, as they are perturbed differently, a controlled collective quantum dynamics cannot be reached and no coherence is then experimentally accessible.

We observed coherent phenomena with molecules by using microwave fields and some promising preliminary results have also been obtained in the mid-infrared region for a

vibrational transition. We present the equations encoding some basic aspects of coherent light-matter interaction to analyse later the experimental data. We show the equations describing a general two-levels quantum system interacting with a monochromatic laser field, whose frequency closely matches the frequency difference between the two states.

Furthermore, we present coherent light-matter interaction in the general framework of open quantum systems theory. By this way we can describe a purely coherent quantum dynamics in the presence of the spontaneous emission occurring from the upper energy level. In such a formalism, the wavefunction description of quantum systems is no more helpful, as it only obeys a unitary time evolution governed by the Shrödinger's equation and cannot account for irreversible, non-unitary time evolution including spontaneous decays. We use, instead, the so-called density matrix representation $\hat{\rho}$. Its general dynamics is described and governed by the following Liouville–von Neumann equation

$$i\hbar\frac{\partial\hat{\rho}}{\partial t} = \left[\hat{H}, \hat{\rho}\right] + \hat{D}(\hat{\rho}),\tag{2.23}$$

where $\hat{D}(\hat{\rho})$ is the so-called dissipator and describes the non-unitary part of dynamics. It is worth noting that, when $\hat{D}(\hat{\rho}) = 0$ and there are no dephasing effects, then the Liouville–von Neumann and the Shrödinger's equations are equivalent.

Now, let us describe a molecule interacting with a monochromatic electric field $\vec{E}(t) = \vec{e}E\cos(\omega_1 t)$, where E denotes the field strength, $\vec{e}$ the unitary vector describing its polarization and ω_1 its frequency. Such a molecule can be described as a two-levels quantum system represented by two-dimensional density matrix $\hat{\rho}$

$$\hat{\rho} = |\psi\rangle\langle\psi| = \begin{pmatrix} \rho_{11} & \rho_{12} \\ \rho_{21} & \rho_{22} \end{pmatrix} = \begin{pmatrix} a_1 a_1^* & a_1 a_2^* \\ a_2 a_1^* & a_2 a_2^* \end{pmatrix},\tag{2.24}$$

where the diagonal elements ρ_{11} and ρ_{22} are the populations of the two states, while the off-diagonal elements ρ_{12} and ρ_{21} are the so-called coherences, encoding the quantumness of the system as their vanishing values imply that quantum features can no longer be observed. The total Hamiltonian $\hat{H}$ can be written as the sum between the Hamiltonian of the unperturbed two-levels system $\hat{H}_0$ and the interaction Hamiltonian $\hat{H}_\mathrm{I}$, with

$$\hat{H}_0 = \begin{pmatrix} \hbar\omega_0 & 0 \\ 0 & 0 \end{pmatrix},\tag{2.25}$$

$$\hat{H}_\mathrm{I} = \begin{pmatrix} 0 & -\mu_{12}E\cos(\omega_1 t) \\ -\mu_{12}E\cos(\omega_1 t) & 0 \end{pmatrix},\tag{2.26}$$

where ω_0 is the transition frequency between the two considered molecular states and $\mu_{12} = \mu_{21} = \langle 1 | \hat{\mu} | 2 \rangle$ is the matrix element of the electric dipole moment operator $\hat{\mu}$ evaluated on the eigenstates of the unperturbed Hamiltonian. As we explained before, they can be non-vanishing only for two eigenstates with opposite parity. The coherent population transfer between these states is usually called Rabi oscillations. Their dynamics is derived in many textbooks, for instance in [130]. Here below, we explicitly derive the equations for the density matrix elements, by highlighting in detail all the approximations done. The Liouville–von Neumann equation for a two-levels molecule interacting with a monochromatic radiation field, without dephasing processes, leads to the following system of coupled differential equations:

$$
\begin{aligned}
\dot{\rho}_{11} &= i\frac{\mu_{12}E}{\hbar} \cos(\omega_1 t)(\rho_{21} - \rho_{12}) \\
\dot{\rho}_{12} &= -i\rho_{12}\omega_0 + i\frac{\mu_{12}E}{\hbar} \cos(\omega_1 t)(\rho_{22} - \rho_{11}) \\
\dot{\rho}_{21} &= i\rho_{21}\omega_0 - i\frac{\mu_{12}E}{\hbar} \cos(\omega_1 t)(\rho_{22} - \rho_{11}) \\
\dot{\rho}_{22} &= -i\frac{\mu_{12}E}{\hbar} \cos(\omega_1 t)(\rho_{21} - \rho_{12})
\end{aligned}
\tag{2.27}
$$

Then, to remove the time dependency, we apply the unitary transformation

$$
\hat{U} = \begin{pmatrix} e^{-\frac{i}{2}\omega_1 t} & 0 \\ 0 & e^{\frac{i}{2}\omega_1 t} \end{pmatrix}
\tag{2.28}
$$

both to $\hat{H}$ and $\hat{\rho}$. Thus

$$
\hat{H}' = \hat{U}^\dagger \hat{H} \hat{U} \quad \text{and} \quad \rho' = \hat{U}^\dagger \rho \hat{U},
\tag{2.29}
$$

yielding

$$
\begin{aligned}
\rho_{11} &\to \rho'_{11} = \rho_{11} & \dot{\rho}_{11} &\to \dot{\rho}'_{11} = \dot{\rho}_{11} \\
\rho_{12} &\to \rho'_{12} = \rho_{12}e^{-i\omega_1 t} & \dot{\rho}_{12} &\to \dot{\rho}'_{12} = \dot{\rho}_{12}e^{-i\omega_1 t} - i\omega_1\rho_{12}e^{-i\omega_1 t} \\
\rho_{21} &\to \rho'_{21} = \rho_{21}e^{i\omega_1 t} & \dot{\rho}_{21} &\to \dot{\rho}'_{21} = \dot{\rho}_{21}e^{i\omega_1 t} + i\omega_1\rho_{21}e^{i\omega_1 t} \\
\rho_{22} &\to \rho'_{22} = \rho_{22} & \dot{\rho}_{22} &\to \dot{\rho}'_{22} = \dot{\rho}_{22}
\end{aligned}
\tag{2.30}
$$

from which we obtain the new equations:

$$
\begin{aligned}
\dot{\rho}_{11} &= i\frac{\mu_{12}E}{\hbar} \cos(\omega_1 t)\left(\rho_{21}e^{i\omega_1 t} - \rho_{12}e^{-i\omega_1 t}\right) \\
\dot{\rho}_{12}e^{-i\omega_1 t} - i\omega_1\rho_{12}e^{-i\omega_1 t} &= -i\rho_{12}e^{-i\omega_1 t}\omega_0 + i\frac{\mu_{12}E}{\hbar} \cos(\omega_1 t)(\rho_{22} - \rho_{11}) \\
\dot{\rho}_{21}e^{i\omega_1 t} + i\omega_1\rho_{21}e^{i\omega_1 t} &= i\rho_{21}e^{i\omega_1 t}\omega_0 - i\frac{\mu_{12}E}{\hbar} \cos(\omega_1 t)(\rho_{22} - \rho_{11}) \\
\dot{\rho}_{22} &= -i\frac{\mu_{12}E}{\hbar} \cos(\omega_1 t)\left(\rho_{21}e^{i\omega_1 t} - \rho_{12}e^{-i\omega_1 t}\right)
\end{aligned}
\tag{2.31}
$$

Then, we multiply the second and third equations respectively by $e^{i\omega_1 t}$ and $e^{-i\omega_1 t}$ and we have:

$$
\begin{aligned}
\dot{\rho}_{11} &= i\frac{\mu_{12}E}{\hbar}\cos\left(\omega_1 t\right)\left(\rho_{21}e^{i\omega_1 t} - \rho_{12}e^{-i\omega_1 t}\right) \\
\dot{\rho}_{12} &= -i\rho_{12}\left(\omega_0 - \omega_1\right) + i\frac{\mu_{12}E}{\hbar}\cos\left(\omega_1 t\right)\left(\rho_{22}e^{i\omega_1 t} - \rho_{11}e^{i\omega_1 t}\right) \\
\dot{\rho}_{21} &= i\rho_{21}\left(\omega_0 - \omega_1\right) - i\frac{\mu_{12}E}{\hbar}\cos\left(\omega_1 t\right)\left(\rho_{22}e^{-i\omega_1 t} - \rho_{11}e^{-i\omega_1 t}\right) \\
\dot{\rho}_{22} &= -i\frac{\mu_{12}E}{\hbar}\cos\left(\omega_1 t\right)\left(\rho_{21}e^{i\omega_1 t} - \rho_{12}e^{-i\omega_1 t}\right).
\end{aligned}
\tag{2.32}
$$

We use now the expansion $\cos\left(\omega_1 t\right) = \frac{1}{2}\left(e^{i\omega_1 t} + e^{-i\omega_1 t}\right)$ and we perform the so-called Rotating-Wave Approximation (RWA) to neglect the rapidly varying terms $e^{2i\omega_1 t}$ and $e^{-2i\omega_1 t}$, usually referred as anti-resonant terms, and we finally obtain the Optical Block equations:

$$
\begin{aligned}
\dot{\rho}_{11} &= \frac{i}{2}\frac{\mu_{12}E}{\hbar}\left(\rho_{21} - \rho_{12}\right) \\
\dot{\rho}_{12} &= -i\rho_{12}\left(\omega_0 - \omega_1\right) + \frac{i}{2}\frac{\mu_{12}E}{\hbar}\left(\rho_{22} - \rho_{11}\right) \\
\dot{\rho}_{21} &= i\rho_{21}\left(\omega_0 - \omega_1\right) - \frac{i}{2}\frac{\mu_{12}E}{\hbar}\left(\rho_{22} - \rho_{11}\right) \\
\dot{\rho}_{22} &= -\frac{i}{2}\frac{\mu_{12}E}{\hbar}\left(\rho_{21} - \rho_{12}\right).
\end{aligned}
\tag{2.33}
$$

If the electric fields non-trivially depend on space no analytical solutions can be found, while when they are homogeneous analytical solutions exist.

Chapter 3

Designing a dipole trap for the absolute ground state CO

A sketch of the experimental setup for optical trapping of absolute ground state CO molecules is shown in Fig. (3.1). A pulsed valve generates a supersonic beam of cold CO molecules, which are pumped to their meta-stable state $a^3\Pi_1$ $|v = 0, J = 1, +\rangle$ by a pulsed laser at 206 nm and loaded on the Stark decelerator after the skimmer selection. Afterwards, slow molecules are further decelerated by an electric field barrier which definitely stop them where two laser beams are focused. The first irreversibly pumps molecules to their absolute ground state $X^1\Sigma^+$ $|v = 0, N = 0, +\rangle$, while the second is the high-power trapping laser.
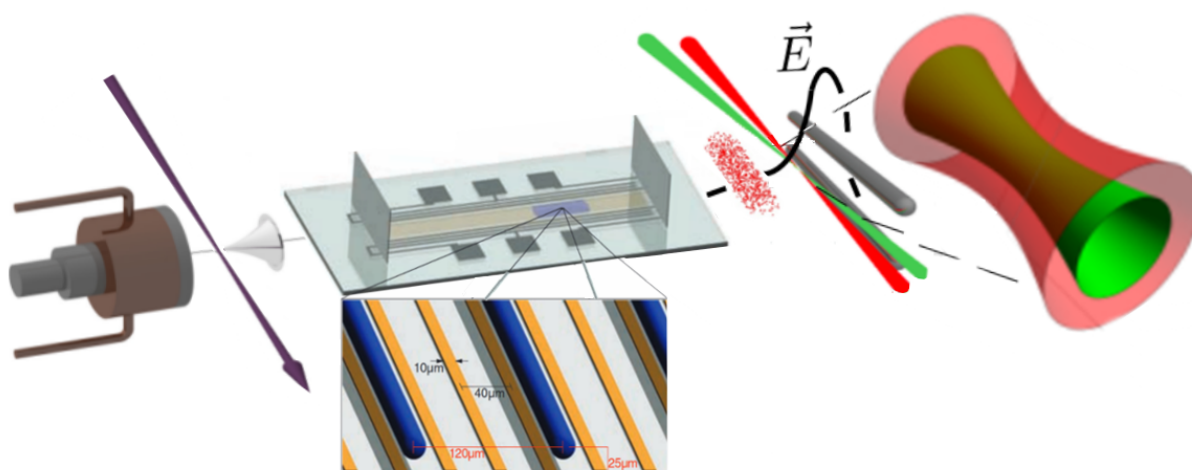

Figure 3.1: A schematic representation for dipole optical trapping experimental setup. The zoom describes the tubular microtraps (blue) on the chip Stark decelerator.

3.1 Meta-stable CO molecules preparation

Here we focus on the preparation of CO molecules in initial meta-stable state $a^3\Pi_1$ $|v = 0, J = 1, +\rangle$. In order to optimize the loading on the microstructured Stark decelerator, we need pulsed molecular beams which, compared to continuous sources, are characterized by a higher beam density, a colder rotational temperature and a narrower velocity distribution [131, 132]. Moreover, due to the short pulse duration, the pumping requirement for the vacuum chamber is greatly reduced and the generation of molecules can be synchronized with the pulsed excitation laser.

We use a modified series 99 General Valve releasing, at a repetition rate of 10 Hz, a gas mixture containing 20% of CO molecules into a vacuum chamber across a 0.76 mm diameter nozzle. It is sealed with a conical poppet coupled to a ferrite material, which is surrounded by a solenoid. Its motion is controlled by short pulses of current in the solenoid, typically of the order of 100 μs. Moreover, the valve body temperature can be controlled between room temperature and 77 K. To adapt its working conditions to a wider range of temperatures, the pre-loading of the spring, counteracting the poppet motion, can be controlled with a micrometric screw without breaking the vacuum. Liquid nitrogen at 77 K firstly refrigerates a flux of nitrogen gas, which is used to cool down the valve body, whose final temperature can be increased and stabilized by using a simple resistive heater. In our experiments we use that valve at a temperature of 140 K, as a pre-cooled gas mixture close to the nozzle, is favorable for the subsequent supersonic adiabatic cooling.

3.1.1 Supersonic adiabatic cooling

Supersonic adiabatic cooling consists in the free expansion into a vacuum chamber of a high-pressure gas, which is allowed to cross a nozzle engineered in such a way to minimize viscous forces, heat conduction and shock waves, so that the expansion is adiabatic and isentropic to a very good approximation. Thermodynamics tells us that any gas, which expands adiabatically and isentropically, must cool.

The cooling produced in a supersonic expansion directly regards the translational temperature, which depends on the width of the gas velocity distribution. As long as molecules are crossing the nozzle and a large amount of scattering processes continues to take place, the speed distribution narrows even more, while its maximum is shifted even forward to higher velocities as the flow is preferentially in one direction. In other words, as

long as molecular collisions drive the expansion, the translational temperature decreases and the mean speed continuously grows. Therefore, as the speed of sound is proportional to the square root of such a temperature, when the flux velocity overcomes it, a supersonic translationally cold molecular beam is generated. After the flow velocity approaches its maximum value, it remains almost constant during the rest of the expansion.

Furthermore, as the translational motion cooling proceeds, molecular collisions tend to cool rotational as well as vibrational degrees of freedom, just as if the molecules had immersed in a colder gas. However, during the expansion not only translational temperature decreases but also the molecular density, so that rotational and vibrational cooling stops when the density becomes too low to allow a significant number of collisions. The final rotational and vibrational temperature essentially depends on their typical relaxation times. As the rotations rapidly equilibrate with the translational bath, they are extensively cooled, while the vibrations are far less effectively cooled as their relaxation time is much higher [133–135]. This fact can be easily understood by using a very simple argument based on the adiabatic theorem as reported in [136].

A two-body collision can be treated as the effect of a time-dependent perturbation $\hat{H}_I$, acting on the incoming molecules by changing their momentum as well as their internal quantum state. Given two states and given a perturbation amplitude, the smaller their energy difference is, the more likely occurs a transition between them. Therefore, as the energy density of rotational levels is about one order of magnitude higher than of the vibrational ones, rotational relaxation is much more effective.

In a supersonic molecular beam translational motion is thus colder than rotations, which in turn are colder than vibrations $T_{tra} < T_{rot} < T_{vib}$. Now, it is difficult to precisely establish the particular values of rotational and vibrational temperature achievable during the supersonic cooling. Indeed, they depend on the particular quantum mechanical amplitudes for the rovibrational transitions mediated by molecular scattering, and presenting such complex quantum mechanical calculations is far beyond the purposes of this thesis.

Instead, concerning the translational temperature and the final longitudinal speed of the supersonic beam, we can estimate them by using simple analytical expressions. We have a mixture of 20% of CO molecules in a given carrier gas, which can be chosen among Xe, Kr, and Ne noble gases. We model such a mixture as an ideal gas characterized by the following values of the average molar mass M and the average heat capacity C_p or

C_v:

$$M = \sum_{i=1}^{2} x_i M_i \qquad C_p = \sum_{i=1}^{2} x_i C_{p,i} \qquad C_v = \sum_{i=1}^{2} x_i C_{v,i}, \tag{3.1}$$

where M_1, $C_{p,1}$, $C_{v,1}$ refer to CO, while M_2, $C_{p,2}$, $C_{v,2}$ to the chosen carrier gas. For our mixture, the molar fractions are respectively $x_1 = 0.2$ and $x_2 = 0.8$. Then, as reported in many textbooks (for instance in [131]), we describe the supersonic adiabatic cooling as an isentropic expansion of an ideal gas, so that the translational temperature T_{tra} and the final longitudinal speed v can be calculated by the following formula:

$$T_{\text{tra}} = T_0 \left(\frac{p}{p_0} \right)^{\frac{\gamma-1}{\gamma}}, \tag{3.2}$$

$$v = \sqrt{\frac{2 C_p T_0}{M}}, \tag{3.3}$$

where T_0 is the gas temperature before the expansion, p_0 and p are, respectively, the gas pressure before and after the expansion, and $\gamma = \frac{C_p}{C_v}$ is the ratio between the heat capacities. Then, by using our experimental setup parameters T_0=140 K, p=2 bar, and p_0=5 10^{-8} bar, the final translational temperature is T_{tra}=0.22 K, independently of the particular noble gas used in the mixture. It is worth noting that the final temperature highly depends on the large difference between the valve backing pressure and the vacuum chamber pressure, while the nature of the carrier gas just affects the final longitudinal speed, heavier atoms leading to slower velocities: v_{Xe}=238 $\frac{\mu m}{\mu s}$, v_{Kr}=294 $\frac{\mu m}{\mu s}$ and v_{Ne}=538 $\frac{\mu m}{\mu s}$, as it is shown in Fig. (3.2).

Now, it is worth underlying why the carrier gas is chosen among noble gases. At these cold temperatures, condensation phenomena could be important. As three-body, or higher, collisions are required to form nuclei around which condensation takes place, the lowering density helps to prevent its occurrence, while noble gases allow to reach colder temperature making condensation further less likely.

Finally, we wonder about the features characterizing the molecular transverse motion. After cooling, the molecules in the supersonic beam cross a cone-shaped skimmer, with an aperture diameter of 1 mm, which selects the central beam traveling into a second, differently pumped, vacuum chamber. Therefore, such a selection effectively defines the transverse speed distribution.
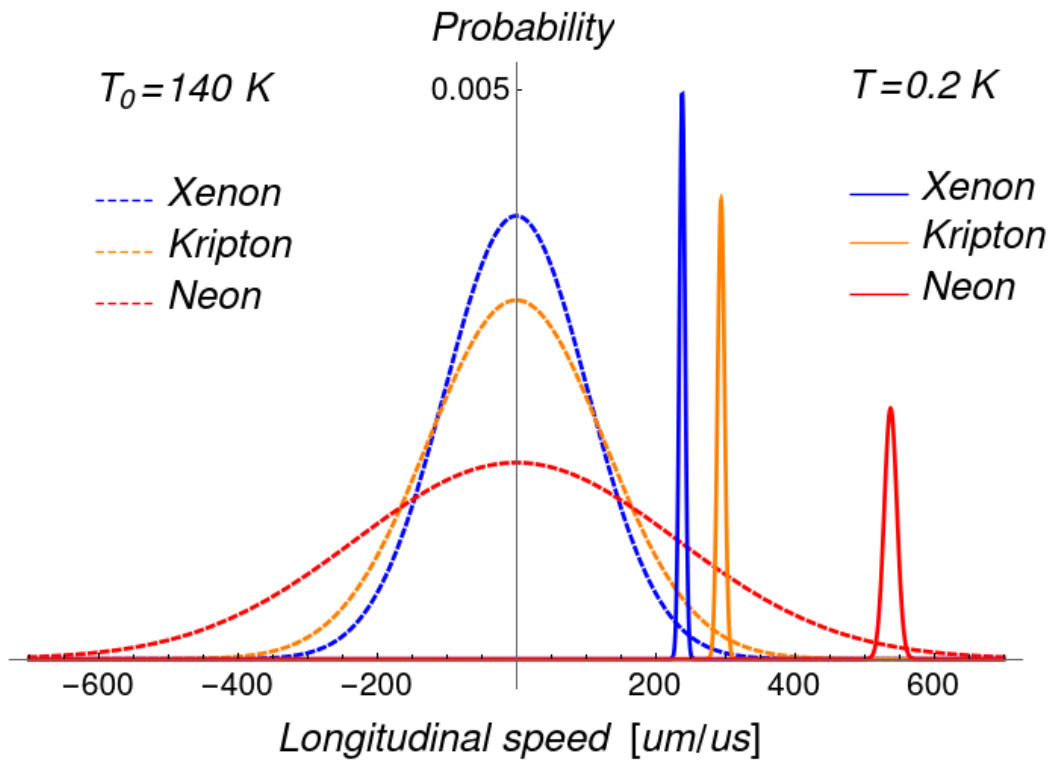
Figure 3.2: We show the longitudinal speed distributions in the laboratory frame of reference of the gas before the nozzle (dashed lines) and after the supersonic adiabatic cooling (solid lines) for three different mixtures 20% of CO molecules, respectively, in Xenon, Krypton and Neon. The three distributions of supersonic molecules are re-scaled by a factor 0.05.

3.1.2 Saturating the spin-forbidden transition

Thanks to supersonic adiabatic cooling, a large fraction of CO molecules initially belongs to the first rotational levels of vibrational and electronic ground state. A precise estimation of such a fraction is not easily given as the temperatures T_{rot} and T_{vib} are not accurately known. Their evaluation would require the knowledge of the rotational and vibrational cross sections together with the scattering probability dependence on the molecular density, calculated during the whole supersonic cooling.

As shown in Fig. (3.3), we focalize an ultra-violet pulsed radiation on the molecular beam. We pump the jet-cooled CO molecules via the spin-forbidden transition $a^3\Pi_1 \; |v=0, J=1, +\rangle \leftarrow X^1\Sigma^+ \; |v=0, N=1, -\rangle$ at 1453233648 ± 5 MHz [137], corresponding to a laser light around 206.29 nm. Such a transition is weakly allowed because the $A^1\Pi$ state interacts with the $a^3\Pi_1$ through the spin-orbit coupling and gives it a par-
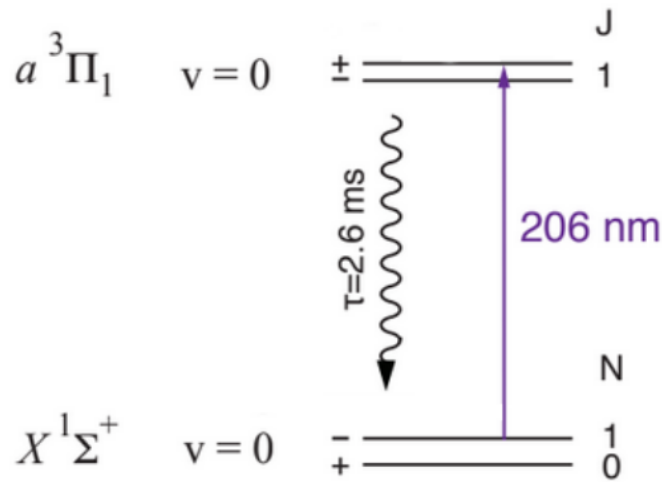
Figure 3.3: Thanks to the supersonic expansion, only the lower rotational levels of the ground state are populated. The pulsed excitation laser at 206 nm saturates the spin-forbidden transition $a^3\Pi_1$ $|v = 0, J = 1, +\rangle \leftarrow X^1\Sigma^+$ $|v = 0, N = 1, -\rangle$. The first electronically excited state $a^3\Pi_1$ then decays back to the ground state with a lifetime of 2.63 ms.

tial spin-zero character. More precisely, as explained in previous chapter, because the spin-orbit Hamiltonian for diatomic molecules mainly couples energy levels with the same Ω quantum number, the major mixing contribution comes from the state $A^1\Pi_1$. This mixing, on one hand enables to saturate such a spin-forbidden transition by using available laser systems, on the other it prevents the decay back to the ground state for a time long enough to perform molecular beam experiments. Indeed $a^3\Pi_1$ lifetime has been measured to be 2.63 ms [122].

For our experiments, we exploit a pulsed UV laser light at 1 mJ, with a Fourier-limited bandwidth of about 150 MHz. Such a radiation is generated by means of an optical parametric oscillator (OPO), as schematically shown in Fig. (3.4). A frequency-doubled pulsed Nd:YAG laser beam at 532 nm (Spectra Physics, Quanta Ray Pro-230) is frequency stabilized by coupling a small amount of its output power to a temperature-controlled iodine cell. Then, it is splitted in two beams. One is frequency-doubled at 266 nm thanks to a BBO crystal, while the other pumps an OPO cavity, consisting of four mirrors and two KTP crystals. The cavity is seeded with a signal radiation at 917 nm
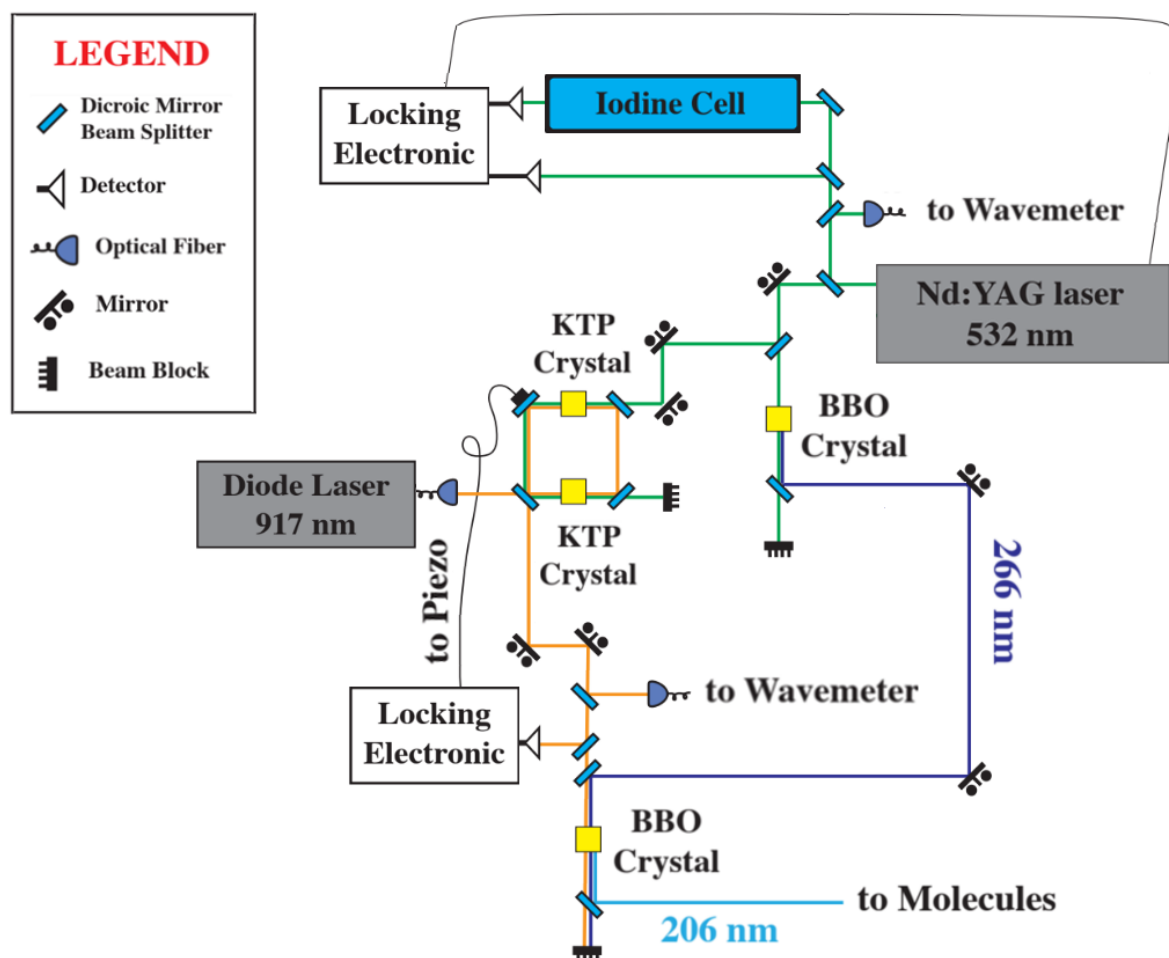
Figure 3.4: Radiation at 206 nm produced via an optical parametric oscillator (OPO).

from a CW diode laser which is also used to stabilize the cavity length. Indeed it is used as the reference for a periodic modulation applied to a piezoelectric element that controls the position of one mirror of the cavity. Finally, the pulsed radiation at 917 nm leaving the OPO cavity is mixed in a second BBO crystal with the beam at 266 nm so that, by means of sum frequency generation, the desired 206 nm radiation is generated. The spin-forbidden transition can be frequency matched by finely tuning the frequency of the seeding diode laser.

3.2 A Stark decelerator on a chip

The Stark decelerator has been successfully tested by many previous experiments and its experimental outcomes can be properly predicted by yet developed complex simulations [138,139]. The output of these simulations will be the basis for our feasibility study, reported in the next chapter. Here, we summarize the main features and the behaviour of the chip decelerator.

Its design has been firstly presented in Ref. [70]. It has been developed for polar molecules in low-field seeking states, therefore suitable for CO molecules in the $a^3\Pi_1$ $|v = 0, J = 1, +\rangle$ state. It consists of a microstructured array of gold electrodes on a glass substrate. Specifically, an array of 1254 equidistant, parallel, gold electrodes, each of which is 4 mm long, 10 μm wide, and approximately 300 nm high, has been configured to generate an array of local minima of electric field strength with a periodicity of 120 μm, about 25 μm above the substrate, as shown in Fig. (3.5). These periodic local minima arise from the superposition principle for the electric fields created by the periodic electrode array.

By applying definite electric potentials to the electrode array, we can control the electric field local minima, effectively acting as a set of low-field seeking traps. While, by using time-varying potentials, we obtain time-varying electrostatic traps. Even more interesting, if the time-varying potentials are time-periodic, for instance sinusoidal functions, we are able to control the traps motion and, by changing their frequency, we achieve different velocities. Furthermore, we can tune the energy depth by changing the potentials strength. Each trap is characterized by a diameter of about 20 μm and the shape of the bottom of each microtrap can be approximated by a harmonic potential.

As the chip controls the motion of such low-field seeking traps, it is a Stark decelerator suitable for CO molecules in the $a^3\Pi_1$ meta-stable state. Molecules flying parallel to the chip surface along its longitudinal axis can be loaded in the microtraps directly from the molecular beam. A schematic representation of the chip Stark decelerator with its tubular, traveling microtraps is shown in Fig. (3.5).

A detailed mathematical description of the relation between the time-varying potentials and the arising 3-dimensional electrostatic moving traps can be found in [140]. Various kinds of waveforms for time-varying potentials and different regimes of Stark deceleration are there accurately analysed. Specifically, it is evidenced how the electrostatic traps geometry slightly varies for different deceleration strength, as shown in Fig. (3.5), and particular attention has been paid on non-adiabatic losses.
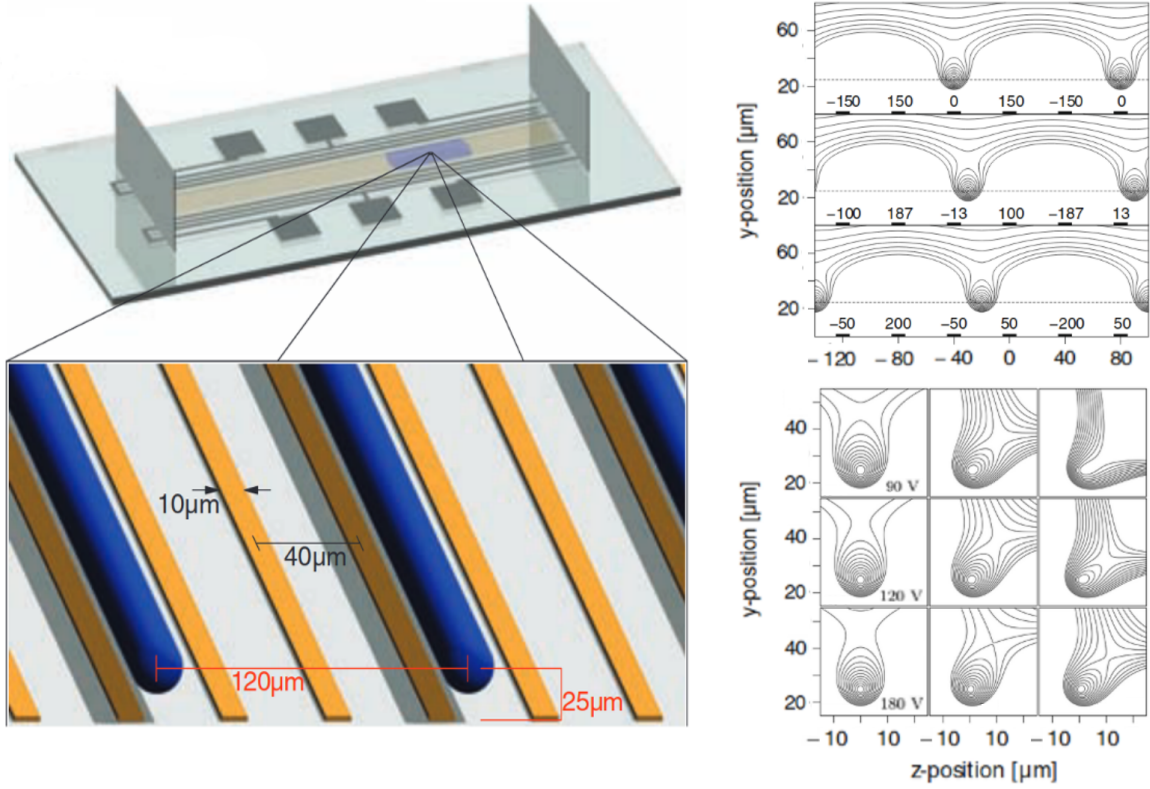
Figure 3.5: The chip Stark decelerator is shown in two stages of magnification with the y axis chosen perpendicular to the substrate while the z axis along it and perpendicular to the electrodes. Low-field seeking microtraps are represented by the blue color. Two insets show calculated equipotential energy surfaces seen by CO in the low-field seeking state $a^3\Pi_1 |v = 0, J = 1, +\rangle$. Up inset shows 70 mK deep traps translated at a constant distance from the surface, where contour lines are separated by 7.5 mK. Down inset shows how the potential energy surfaces are distorted when microtraps undergo a constant deceleration for three different rates and three different peak-to-peak waveforms amplitudes. Contour lines are separated by 2.6 mK, 3.5 mK, and 5.3 mK. At zero acceleration, the traps are symmetric around $z = 0$, but as the deceleration increases, the traps tilt to the right and become shallower and disappearing in the extreme case. Image is taken from [140].

About our trapping experiment, there are two major aspects concerning the chip Stark decelerator: the final microtraps velocity and the microtraps energy depth. The first governs the average speed by which molecules leave the chip along the molecular beam axis, while the second gives rise to the molecular thermal motion after their release from the traps at the end of the chip. Here below, we summarize both aspects in some details.

3.2.1 Microtrap's velocity

We discuss the capability of controlling the final longitudinal speed of Stark decelerated CO molecules leaving the chip. The microtraps longitudinal speed is controlled via the frequency of the waveforms applied to chip's electrodes. Then, if such a frequency is not kept constant and it is properly decreased in time, we can generate a set of decelerating microtraps. To load the incoming supersonic beam on the chip, the initial frequency is chosen to match the velocity of the microtraps to that of the faster incoming molecules, while it is therefore decreased accordingly to the arrival time of the slower ones. As reported in [69,140], simulations of the microtrap Stark deceleration are in weak agreement with the experimental results, as shown in Fig. (3.6).

However, we see how the disagreement between measured and predicted values grows for increasing deceleration rates. This fact fundamentally depends on two reasons. The first is well accounted by the simulations and directly comes from the decreasing of the trap energy depth when the deceleration rate increases at a constant peak-to-peak waveform amplitude, as shown in Fig. (3.5). Increasing deceleration rates leads, indeed, to shallower traps so that the number of trapped molecules is correspondingly lower. The second main reason for the disagreement between simulations and experiments consists in the non-adiabatic losses, which are not taken into account within the simulations. Non-adiabatic transitions essentially depend on two aspects: the energy difference between the closest coupled quantum states, and the rate at which the energy of a defined state changes in time. Qualitatively, when the energy of a quantum state varies very rapidly as compared to the energy difference between that state and the closest one, then there is a non-vanishing probability that the transition between the two states occurs.

On one side, the $a^3\Pi_1 \ket{v = 0, J = 1, +}$ state, at vanishing electric and magnetic fields, is degenerate with another quantum state, whose Stark shift is negligible and cannot be trapped. Then, when the energy difference between these two states is small enough, non-adiabatic losses are highly probable to occur. If no magnetic field is present, they happen for molecules traveling close to the electric field minima within the traps.

Otherwise, non-adiabatic losses can occur if the rate of change of the Stark shift exceeds the energy difference between two levels. This appears, as a consequence of the so-called jittering for the electrostatic traps, coming from the unavoidable fluctuations due to imperfections in the amplitude, offset and phase of the waveforms applied to the chip's electrodes. To rule out non-adiabatic transitions, we can perturb the molecules to increase the energy difference between their coupled energy levels. As experimentally
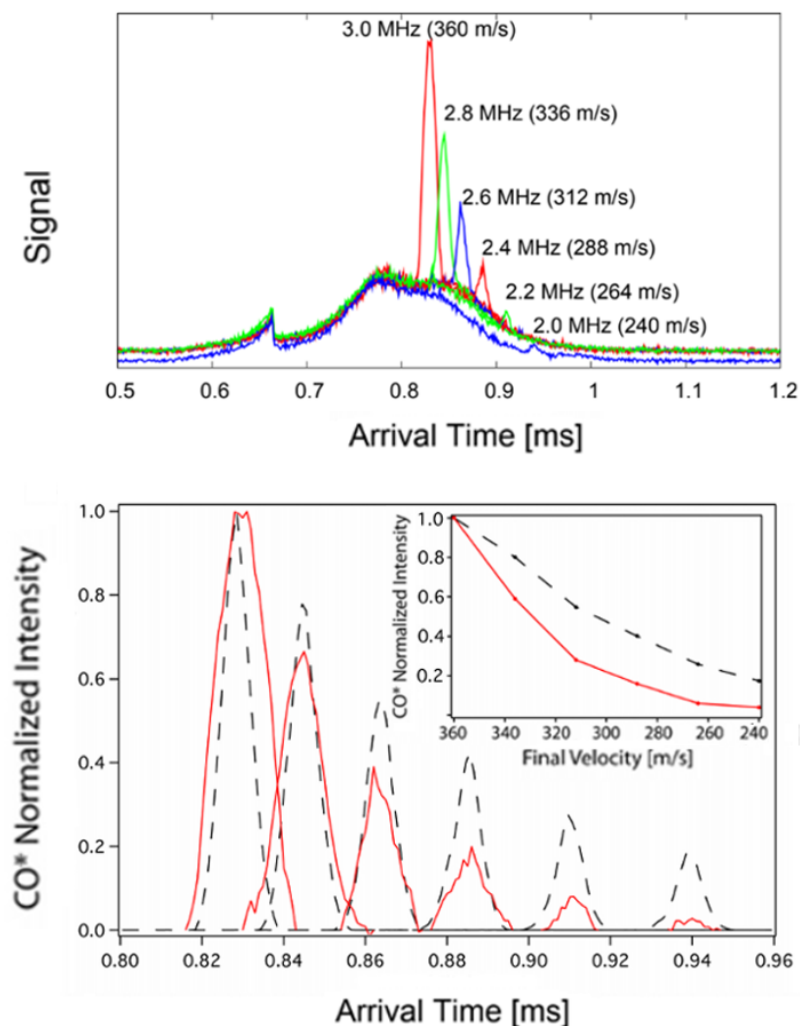
Figure 3.6: On the top, experimental results are shown for various deceleration regimes leading to different final velocities. In the leftmost trace, the waveforms driving the chip's electrodes have a constant frequency of 3.0 MHz. In subsequent traces, the frequency of the waveform is reduced to different values over different time-intervals, after which the waveforms are switched off. Downside, the same experimental results (solid red), after background subtraction, are compared with the simulations (dashed black), yielding to a good agreement. However, the trajectory simulations predict a decreasing number of decelerated molecules as the acceleration increases but the loss in experiments is higher than the one predicted. The inset shows the integrated intensity of each peak, plotted against the final velocity of the molecules in that peak. Images are taken from [140].

tested in [141], to reduce the role of non-adiabatic losses, the degeneracy at zero electric field has been eliminated by adding a strong enough magnetic field, thanks to the Zeeman splitting. Under this condition, trajectory simulations and experimental data are in excellent agreement and we can safely use them to generate the input of our software. Furthermore, to our purposes the microtrap velocity can be considered, from now on, a free parameter that we can arbitrarily choose.

3.2.2 Thermal motion

Two-dimensional spatial imaging experiments have been performed to observe the free expansion of molecules after they are released from the chip. The basic idea is to ionize the molecules and image their position on a screen. A set of ion lenses is therefore used to image the produced CO cations onto a micro-channel plate detector (MCP), followed by a phosphor screen, whose emitted photons are finally collected by a CCD camera yielding the two-dimensional images, as shown in Fig (3.7).

From each sequence of imaging measurements, it is then possible to extract the molecular free expansion velocity for different values of trap energy depth as controlled via different amplitudes of the waveforms applied to the electrodes. Now, it is fundamental to clarify that we cannot directly link these spreading velocities to the concept of temperature, which cannot be strictly defined. Indeed, the low density, 10^7 cm^{-3} of trapped molecules, prevents collisions to occur and then rules out any thermalization process. Actually, as demonstrated in [139], the various velocities distribution can be understood as arising from the trap's energy depth and the particular trap's shape. Deeper traps lead to velocity distributions peaked around higher speed values, while the distinctive trap shape mainly affects their tails behaviour. As shown in Fig. (3.8) the molecular speed distributions can be approximated very well by using the Maxwell-Boltzmann distributions. Therefore, even if the molecular temperature is not strictly defined, it can be taken from the best Maxwell-Boltzmann fit of the data. As shown by Fig. (3.8), previous experiments reported in [139] demonstrated the capability of producing cold molecules characterized by a temperature of few mK. Moreover, the experimental data are in excellent agreement with the predictions based on trajectories simulations, thus demonstrating their validity.

Finally, a clear analysis on the relation between microtrap's shape and velocity distribution has been done. By taking different analytical expressions for the trap's potential, different distributions have been predicted and, as expected, conical traps lead to similar distributions, while for instance harmonic traps do not. Furthermore, by integrating
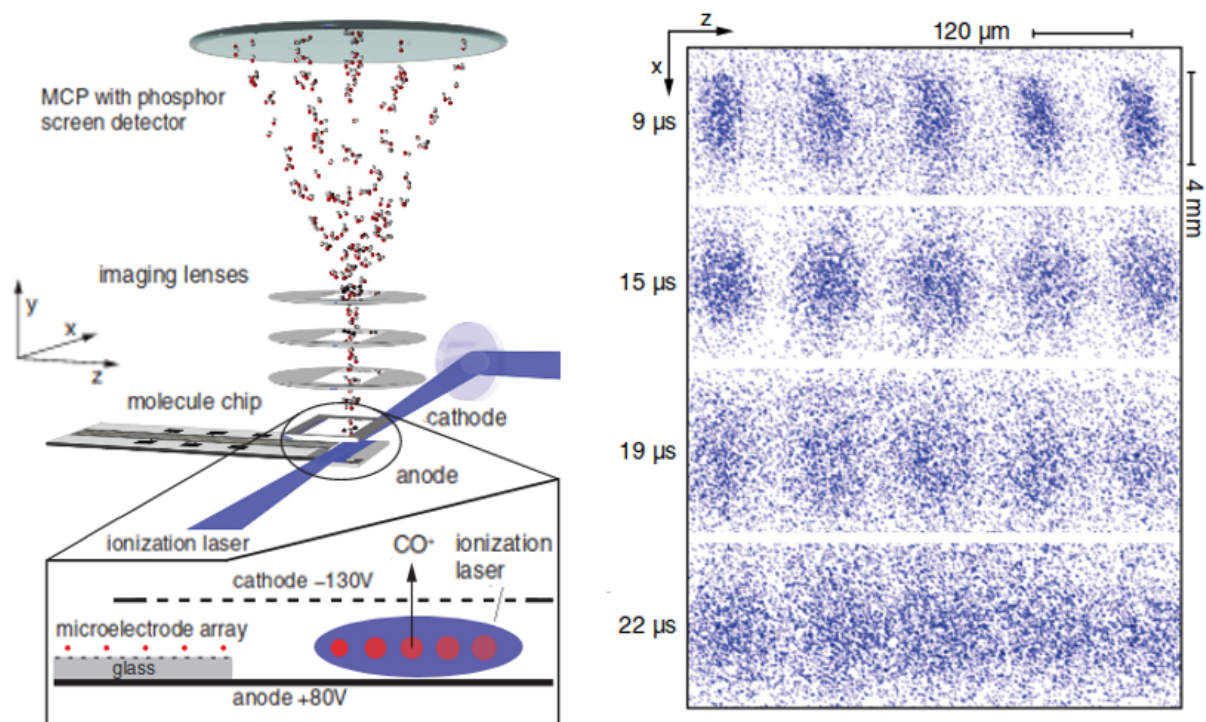
Figure 3.7: On the left, meta-stable CO molecules on the chip Stark decelerator are ionized via REMPI using a pulsed 283 nm laser. Then, ion optics are used to form an image on a MCP detector, followed by a phosphor screen and a CCD camera (not shown) finally used to record the image. On the left, the zoom shows molecules still trapped above the chip, while, on the right, five clouds of molecules of increasing sizes are shown after ballistic flight within the focal spot of the ionizing laser. In the center, two-dimensional spatial imaging data are shown. Molecules are imaged for different ballistic expansion times. The vertical direction x is along the length of the microtraps, while the horizontal z direction is along the molecular beam axis. The experimental procedure runs at a rate of 10 Hz and the images are the sum of approximately 10^5 experimental cycles. Images are taken from [138, 139]
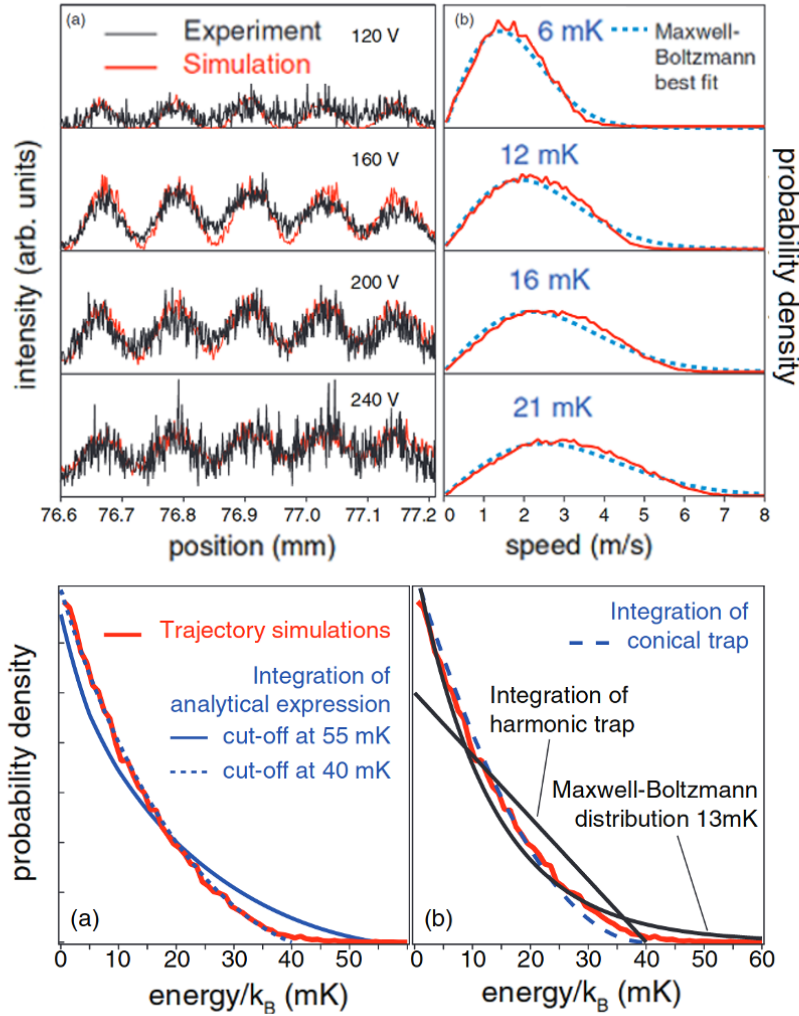
Figure 3.8: On the left, experimental data and trajectories simulations are in excellent agreement for different values of the voltages, and corresponding speed distributions (red solid line) extracted from the trajectory simulations are compared to the best fit Maxwell-Boltzmann curve (blue dashed line), labeled with the best fit temperature. Speeds are given relative to the mean forward velocity of the molecular cloud. On the right, it is shown a comparison between energy distributions arising from trajectories simulations (red solid line) and analytical calculations based on different trap's potentials, namely conical, harmonic and logarithmic potentials. The integration of such a conical potential returns an exponential distribution for the kinetic energy, which is precisely the Maxwell-Boltzmann distribution for a thermal ensemble in two dimensions. Images are taken from [139]

the analytical expression for the same conical trap's potential to different cutoff energies above the trap minimum, different results are obtained. In particular, if is considered an average value for the trap's energy depth, by taking into account also the deceleration process, a very good agreement can be reached even by analytical calculations. This reflects the fact that identical applied voltages correspond to shallower traps during deceleration, therefore reducing the effective temperature for trapped molecules.

In conclusion, we emphasize that in previous experiments it has been possible to finely control both the molecular motion and their temperature via the chip Stark decelerator. Moreover, the yet developed software performing trajectories simulations, has been used to predict very well all the experimental findings. From our perspective, this point is of fundamental relevance, since our feasibility study of the dipole trap is finally based on the output of such a software. Finally, since both the microtrap's velocity and temperature can be freely chosen by properly applying definite waveforms, from now on, we consider them in our simulations as free parameters.

3.3 Optical pumping

To drive meta-stable CO molecules to their absolute ground state, we use the following laser system. A 5 W cw semiconductor laser at 532 nm pumps a tunable cw ring dye laser (Radiant Dyes Laser Accessories GmbH). With Rhodamine 6G it can be used at the desired frequency around 563 nm with a power up to 300 mW. Moreover, it has a bandwidth of about 1 MHz and, by using a digital controller scan generator, its frequency can be finely tuned with a scan resolution down to a few MHz. By properly setting its frequency, it can be used to transfer meta-stable CO molecules towards their absolute ground state via stimulated emission pumping, by using different intermediate quantum states as reported below.

3.3.1 Favorable optical pumping scheme

Absolute ground state CO molecules can be prepared, thanks to the highly favorable irreversible optical pumping scheme firstly reported in [123] and schematically shown in Fig. (3.9). From the spin-triplet excited state $a^3\Pi_1$ $|v=0, J=1, +\rangle$, CO molecules can be transferred to the spin-singlet absolute ground state $X^1\Sigma^+$ $|v=0, N=0, +\rangle$ via stimulated emission pumping by using a continuous-wave laser around 563 nm. This wavelength just connects the triplet state $a^3\Pi_1$ with the singlet state $A^1\Pi$ $|v=1, J=1, -\rangle$,
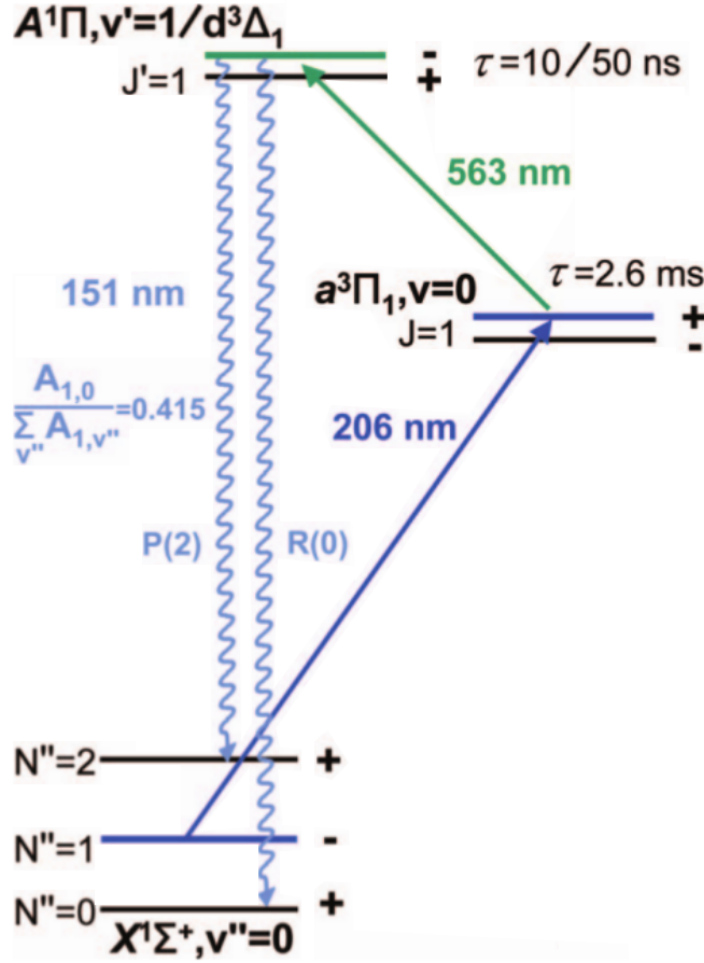
Figure 3.9: Energy level diagram of the relevant states involved in the optical pumping scheme proposed in [123] to populate the absolute ground state of CO molecules. A first radiation at 206 nm excites CO molecules to their low-field seeking component $a^3\Pi_1 |v = 0, J = 1, +\rangle$. Then, they are transferred to the spin-singlet state $A^1\Pi$ $|v = 1, J = 1, -\rangle$, via its perturbing triplet states $d^3\Delta_1$ and $e^3\Sigma_1$, and subsequently decay to the ground state after few tens of ns. The branching-ratio up to 28% towards the absolute ground state $X^1\Sigma^+ |v = 0, N = 0, +\rangle$ makes this optical pumping scheme very efficient. Image is taken from [123].

via its perturbing triplet states $d^3\Delta_1$ and $e^3\Sigma_1$. Indeed, the singlet state $A^1\Pi$, by interacting with the triplet states $d^3\Delta_1$ or $e^3\Sigma_1$, takes from them a large amount of triplet character, which opens the otherwise spin-forbidden transition $A^1\Pi |v = 1, J = 1, -\rangle \leftarrow a^3\Pi_1 |v = 0, J = 1, +\rangle$. This large mixing essentially explains why 300 mW can drive such a spin-forbidden transition. Moreover, it is worth noting that it can be used over a wide

spectral range covering all the above mentioned transitions, namely the $d^3\Delta_1$ levels and the $e^3\Sigma_1$ levels. Then, since the excited state $A^1\Pi$ and the ground state $X^1\Sigma^+$ are both spin-singlets, a very fast spontaneous decay occurs and populates the ground state $X^1\Sigma^+$. This radiative decay time has been measured to be few tens of ns [142].

Quantum selection rules tell us that the parity changes for each dipole transition. Thus, starting from molecules lying in the meta-stable state $a^3\Pi_1 \ket{v = 0, J = 1, +}$, after the stimulated emission pumping, only positive parity ground state components $X^1\Sigma^+$ can be populated. Then, by spontaneous rovibrational emission, different positive parity ground state components can be finally populated. It has been predicted that the transitions towards the vibrational ground state $X^1\Sigma^+$, $v = 0$ are the 41.5% of the total amount of the transitions towards all the others vibrational states [123]. Moreover, only some of these populate the absolute ground state. In rovibrational molecular spectroscopy there are P, Q and R branches, respectively corresponding to transitions with $\Delta J = -1$, $\Delta J = 0$ and $\Delta J = +1$. The parity selection rules take out Q-branch transitions, while from theoretical calculations R-branch transitions are twice as strong as the P-branch ones [143]. Therefore, the final result is that up to 28% of the total amount of decays from the state $A^1\Pi \ket{v = 1, J = 1, -}$, take place towards the absolute ground state $X^1\Sigma^+$ $\ket{v = 0, N = 0, +}$. It is worth noting that such a prediction is based on the assumption that no electric fields are present during the optical pumping. If some electric electric fields are present, they mix opposite parity states for each intermediate Λ-doublet, thus leading to a reduction of the 28% absolute ground state branching-ratio.

3.3.2 Observed highly meta-stable states

Ground state stimulated emission pumping around 563 nm can be realized by means of different intermediate quantum states. Four transitions, represented in Fig.(3.10), have been first observed in [123].

Instead, those transitions coming from the interaction between the $A^1\Pi$ levels and the $e^3\Sigma_1$ levels have not yet been reported in literature. To find these transitions we used a tunable pulsed dye laser with a bandwidth of about 1 GHz (Radiant Dyes Laser Accessories GmbH, NarrowScan), pumped by a frequency doubled Nd:YAG 10 Hz laser source at 532 nm (InnoLas Photonics GmbH, SpitLight 1200). More precisely, we performed a frequency scan, over the spectral region where they were expected to be, while recording the intensity of the fluorescence signal back to the ground state by using a Photo-Multiplier-Tubes (PMT). We obtained the data represented in Fig. (3.11). Given such results, we
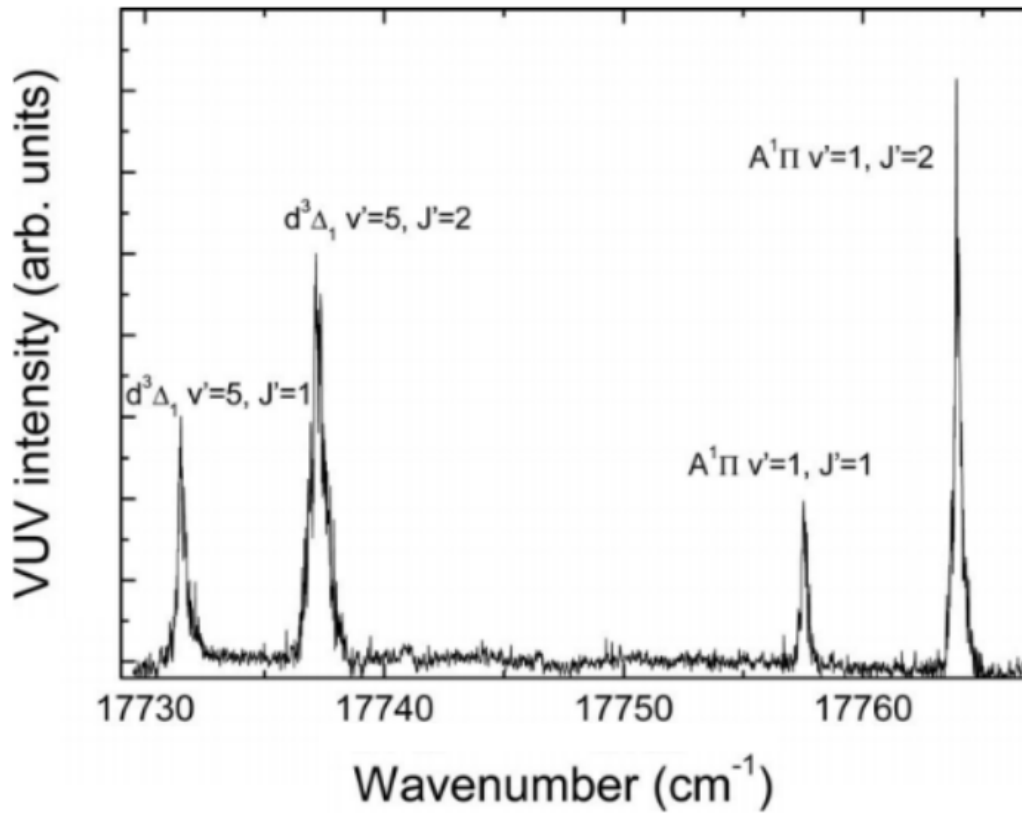
Figure 3.10: Vacuum Ultra Violet (VUV) excitation spectrum of meta-stable CO molecules. Molecules are optically excited from the state $a^3\Pi_1$ $|v=0, J=1, +\rangle$ to the levels identified in the figure, while the intensity of the VUV fluorescence back to the ground-state is recorded. More precisely, the four observed lines arise from the lowest two rotational levels of the mutually interacting $d^3\Delta_1$ v=5 and $A^1\Pi$ v = 1 states. Image is taken from [123].

observed them again by using the much narrower RDL, so that we determined with higher precision their frequencies as 16323.420 $\pm$0.001 cm^{-1} and 16330.453 $\pm$0.001 cm^{-1}. Moreover, for both transitions we measured the fluorescence signal for different values of RDL power as reported in Fig. (3.12).
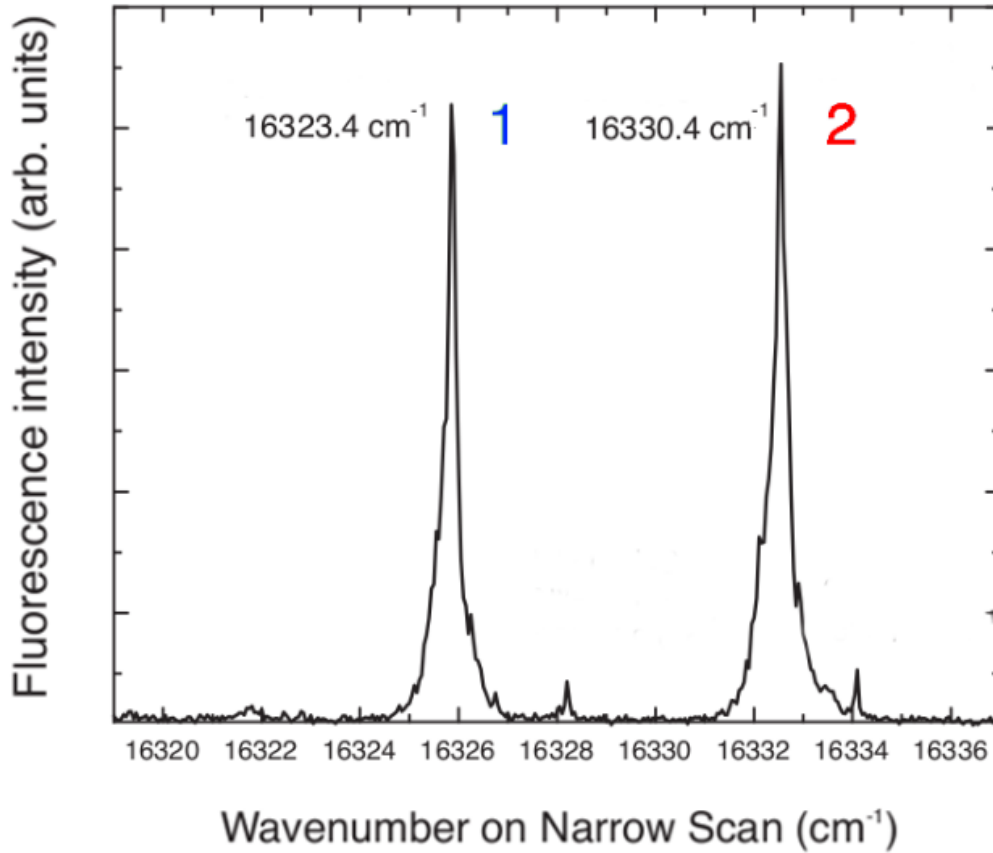
Figure 3.11: Vacuum Ultra Violet (VUV) excitation spectrum of meta-stable CO molecules. Molecules are optically excited from the state $a^3\Pi_1$ $|v = 0, J = 1, +\rangle$ to the levels within the highly meta-stable $A^1\Pi$ state perturbed by $e^3\Sigma_1$ levels. The frequency scan is performed by using the Narrow Scan pulsed laser, while the intensity of the fluorescence back to the ground state is recorded by using Photo-Multiplier-Tubes.

3.4 High-power trapping laser

We described above how meta-stable CO molecules are suitable for Stark deceleration and how a favorable optical pumping scheme can be exploited to irreversibly drive them towards their absolute ground state. Then ground state CO molecules can be trapped via the polarizability potential in the focal spot of a high-power laser beam.

In this thesis, we consider the dipole trap realized by means of a high-power IPG
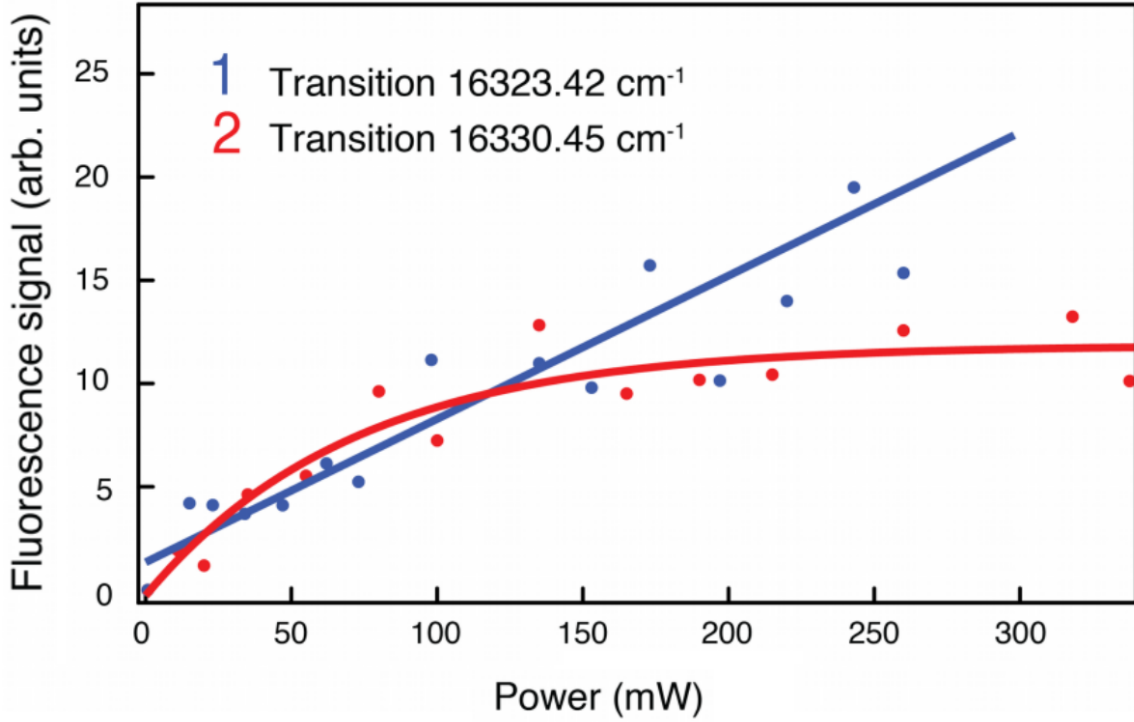
Figure 3.12: Dependence on the RDL power for the fluorescence signal measured by using Photo-Multiplier-Tubes for both the new observed transitions showed in Fig. (3.11). We see that the florescence corresponding to the transition at 16323.420 cm^{-1} is more intense, thus it is more attractive that the one at 16330.453 cm^{-1}. To reduced as much as possible the influence from the fluctuations of the number of CO molecules in the state $a^3\Pi_1$ $|v = 0, J = 1, +\rangle$, we recorded the fluorescence signal from this state with another PMT. Then, we normalized the fluorescence from the $A^1\Pi$ state back to the ground state, by dividing its value with the fluorescence from the $a^3\Pi_1$ $|v = 0, J = 1, +\rangle$ state. The two independent PMT are placed in such a way to minimize their response to the undesired wavelengths.

Ytterbium Fiber Laser, available in our lab, which can reach a huge power around 300 W. To be conservative, we consider a really usable maximum power of 240 W, thus reduced by a 20%.

In our simulations, we model its electric field spatial distribution as a Gaussian TEM$_{00}$

mode:

$$E(x, y, z) = \sqrt{\frac{4P}{\pi \epsilon_0 c w_0^2}} \frac{w_0}{w_z} e^{-\frac{x^2+z^2}{w_z^2}},$$

$$(3.4)$$

$$w_z = w_0 \sqrt{1 + \left(\frac{(y - y_0)\lambda}{\pi w_0^2}\right)^2},$$

where P is the laser power, w_0 is the beam waist and λ the laser wavelength. Moreover, we assumed that the laser is centered at the origin, while its optical axis lies along the y-axis.

3.5 Measuring apparatus

Optically trapped absolute ground state CO molecules can be finally observed by using a very sensitive and state-selective detection system. It involves different processes, a first excitation to the meta-stable state $a^3\Pi_1$, a subsequent ionization and a final electrical acceleration towards a micro-channel plate detector.

The transition to the $a^3\Pi_1$ state can be performed by a 206 nm radiation, which can be generated by a completely analogous system as the one, described before, used to prepare excited CO molecules at the beginning of the trapping experiment. Compared to that case, the only variation regards the required tiny frequency difference coming from the different ground state rotational level, which here is $N=0$ and not $N=1$. Then the ionization process is based on the REMPI process. REMPI is an highly sensitive and state-selective detection method widely used in molecular spectroscopy. It is a process in which the energy of an integral number of photons matches the energy difference between the initial quantum state and some intermediate state. A general (n+m) REMPI process exploits n photons for the transition to the intermediate quantum state, while the other m photons are used for ionization. Being a multiphoton phenomenon, it requires a large power, so that it is typically realized by means of pulsed laser beams. In our case, as shown in Fig. (3.13), after the transition at 206 nm, we exploit a (1+1) REMPI in which the first photon at 283 nm excites CO molecules from their meta-stable state $a^3\Pi_1$ $|v = 0, J = 1, -\rangle$ to the intermediate rotational levels of the $b^3\Sigma^+$ state, while the second ionizes them.

The radiation at 283 nm needed for REMPI detection is generated by means of two
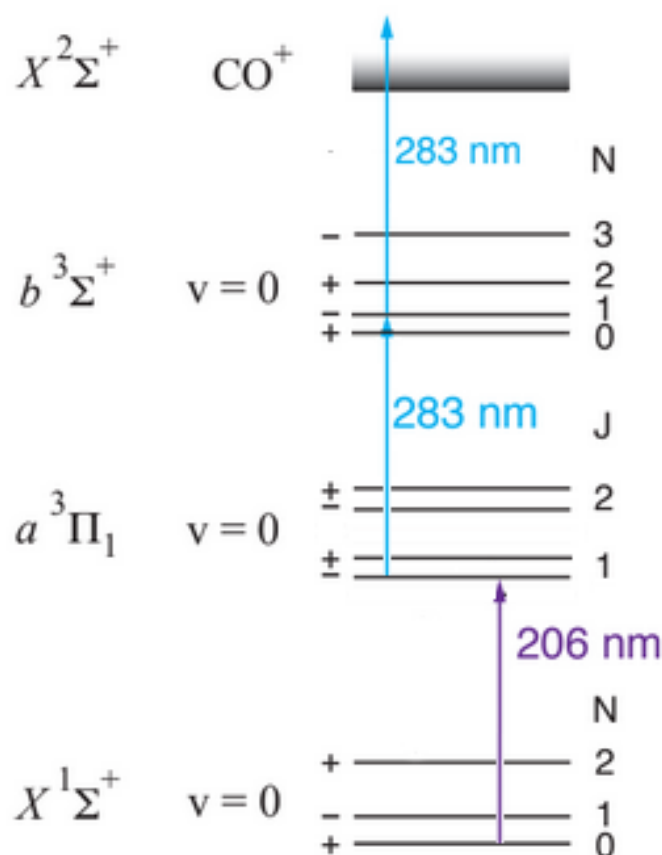
Figure 3.13: Energy level diagram of the relevant states involved in the absolute ground state detection. A first transition at 206 nm to the meta-stable $a^3\Pi_1$ state is followed by a two-photons REMPI ionization at 283 nm. More precisely REMPI detection can exploits different rotational levels N=0,1,2,3 of the electronically excited state $b^3\Sigma^+$.

laser systems. A first frequency doubled Nd:YAG 10 Hz laser source at 532 nm (InnoLas Photonics GmbH, SpitLight 1200), pumps a tunable pulsed dye laser (Radiant Dyes Laser Accessories GmbH, NarrowScan) which can be controlled by a grating with a bandwidth of about 1 GHz. By using Fluorescine 27, it emits in the spectral range between 541 nm and 571 nm, thus it can be frequency doubled with a BBO crystal, to achieve the desired frequency of about 283 nm. Furthermore, we can select the desired rotational level in the intermediate $b^3\Sigma^+$, v=0 state, by controlling the dye laser frequency. The efficiency of this system cannot be precisely predicted, and to be conservative, we consider a REMPI

detection efficiency around 80%.

Suddenly after REMPI, two electrodes can be used to accelerate CO^+ ions towards a micro-channel plate. It is an array of electron multipliers oriented parallel to one another. When a fast CO^+ ion impacts on them, a cascade signal of electrons are generated with an efficiency close to unity. Such a current signal can be amplified and measured. By this way, we are able to perform state-selective detection for a very small number of ground state CO molecules, the main limit coming from the REMPI detection efficiency. We expect then to be able to observe them down to few units per experimental cycle.

Chapter 4

Dipole trap feasibility study and simulations

4.1 Introduction

Here we simulate the whole experimental cycle in order to estimate the trapping probability. The results of the simulations will allow to decide if it is reasonable to start to implement such a trapping experiment or if it is more promising to explore other techniques.

The trapping experiment has been shown in Fig. (3.1) and described in the previous chapter. Summarizing, meta-stable $a^3\Pi_1$ CO molecules, suitable for Stark deceleration, are firstly laser-prepared. They are loaded on the chip Stark decelerator and slowed to the desired longitudinal speed with a given temperature down to few mK. Then, they leave the chip and an electric field barrier decelerates them. A pumping laser efficiently drives them to their absolute ground state and prepares them to be trapped by a high-power laser. Finally, a state-selective detection system observes those molecules successfully loaded in the optical dipole trap.

As discussed above, the simulations of the Stark deceleration in the microchip were developed in past years, and the predicted molecular distribution after the chip has been used and tested for many previous experiments, so that the output of such program can be trusted. Starting from this molecular distribution, we developed new simulations encoding all the other components. For a given configuration of the experimental setup, we can calculate the trapping probability as the ratio between the number of trapped molecules and the number of molecules in the distribution we start with. Each configuration depends

on many parameters which describe the whole setup. For instance, we can explore how the trapping probability varies as we change the positions and the waist of the RDL and the trapping laser, or as we change the electric field barrier and the microtraps speed and temperature. Then, we can search for the optimal experimental setup by comparing the output corresponding to many different configurations. The idea is very attractive as it permits to explore the consequences for a large amount of different setups. However, this task is quite complex as we have many independent free parameters and we need to scan a huge multidimensional space.

In order to present our feasibility study of such a complex trapping experiment, we firstly describe in some details the main aspects of our simulations. We focus on trajectory simulations and then we describe how we model the quantum transitions due to spontaneous emission. Afterwards, we present the results of our simulations.

4.2 Molecular trajectories

Meta-stable CO molecules, leaving the chip Stark decelerator, are characterized by a number density down to 10^7 cm^{-3} [139]. Then, to describe their motion, we safely neglect their mutual interaction and simulate single molecule trajectories, which are governed by physical potentials depending on the particular molecular state. We consider two relevant quantum states, the meta-stable $a^3\Pi_1$ $|v = 0, J = 1, +\rangle$ and the absolute ground state $X^1\Sigma^+$ $|v = 0, J = 0, +\rangle$. In fact, molecules in different states are lost during the experiment and we just account them in the total amount of molecules, while the other intermediate $A^1\Pi$ state, involved in the ground state optical pumping, can be safely ignored because its lifetime of few tens of ns [123] is very short as compared to the ms time scale of molecular trajectories.

Here below, we summarize the physical potentials governing the molecular motion in the presence of static and dynamical external electric fields. We neglect the interaction with an external magnetic field as it can be produced with inhomogeneities lower than few Gauss over the whole trapping region, so that the magnetic forces are orders of magnitudes lower than electric ones. Magnetic field is thus only useful to prevent non-adiabatic losses via the Zeeman splitting.

4.2.1 Low-field seeking excited state $a^3\Pi_1$

When CO molecules in the low-field seeking excited state $a^3\Pi_1 \,|v = 0, J = 1, +\rangle$, interact with a static electric field, their motion is governed by the following DC Stark potential:

$$U_{\text{Stark}}\left(E\right) = \sqrt{\left(\frac{\mu_e E}{2}\right)^2 + \left(\frac{\Lambda}{2}\right)^2} - \frac{\Lambda}{2}, \tag{4.1}$$

where E is the electric field strength, $\mu_e = 1.37$ Debye is the electronic dipole moment and $\Lambda = 394$ MHz is the Λ-doublet splitting.

If instead they interact with an electromagnetic wave, their motion obey the so-called polarizability potential:

$$U_\alpha(E) = -\frac{1}{2}\alpha E^2, \qquad \alpha = 4.7 \cdot 10^{-3} \, \frac{\mu\text{m}^4}{\mu\text{s}^2 \, V^2} \tag{4.2}$$

where the assumed polarizability α of CO molecules comes from the most recent value reported in literature [144], which is the same of the ground state polarizability.

4.2.2 High-field seeking ground state $X^1\Sigma^+$

As reported in [123], CO molecules in their absolute ground state $X^1\Sigma^+ \,|v = 0, J = 0, +\rangle$ moving in a static electric field are governed by the following purely quadratic DC Stark potential:

$$U_{\text{Stark}}\left(E\right) = -\text{k}E^2, \qquad \text{k} = 1.4 \cdot 10^{-2} \, \frac{\mu\text{m}^4}{\mu\text{s}^2 \, V^2}, \tag{4.3}$$

While the polarizability potential, responsible for the trapping force, is the same of the meta-stable CO molecules:

$$U_\alpha(E) = -\frac{1}{2}\alpha E^2, \qquad \alpha = 4.7 \cdot 10^{-3} \, \frac{\mu\text{m}^4}{\mu\text{s}^2 \, V^2}. \tag{4.4}$$

These physical potentials are used to simulate all the molecular trajectories for the trapping experiment.

4.3 Physical constraints

The trapping probability depends on many different experimental parameters, which are encoded in our simulations, such as the microtrap's velocity and temperature, the electric field barrier space-time dependence, the position, orientation and power of the pumping and trapping laser beams. We start by simplifying as much as possible the set of independent parameters, thus greatly reducing the space to be explored in order to predict the maximum value for the trapping probability achievable by using our setup. In fact, many experimental parameters are correlated among each other, while many others are subjected to physical constraints to make the trapping experiment feasible. Here below, we describe these physical constraints and correlations, in order to clearly understand the final simulation findings.

4.3.1 Optical trapping geometry

Meta-stable CO molecules leave the chip in tubular packets with a length of 2 mm along the y-axis. Therefore, it is appropriate that the pumping laser and the optical trap lie in front of them with their optical axis aligned along the y-axis.

Moreover, in order to make the trapping experiment feasible, excited CO molecules have to be transferred to their absolute ground state inside the optical trap. Therefore, the pumping laser must be focused inside the dipole trap. As shown in Fig.(4.1), both lasers are focused with the same focal point along the same optical axis.

After they leave the chip, the tubular packets of CO molecules get bigger accordingly to their speed distribution, and their size determines the spatial overlap with the optical trap. Moreover, they spontaneously decay with a lifetime τ=2.63 ms, so that it is highly desirable that the optical trap lies as close as possible to the chip exit. As we want that the chip is not damaged by the high-power trapping laser, the minimum distance D is fixed by taking three times its y-waist, calculated at the border of the chip (whose width is 4 cm), by the following expression:

$$D(w) = 3w\sqrt{1 + \left(\frac{y_c\lambda}{\pi w^2}\right)^2}, \tag{4.5}$$

where w is the optical trap waist, $\lambda = 1.071$ μm its wavelength and $y_c = 2$ mm is half width of the chip.
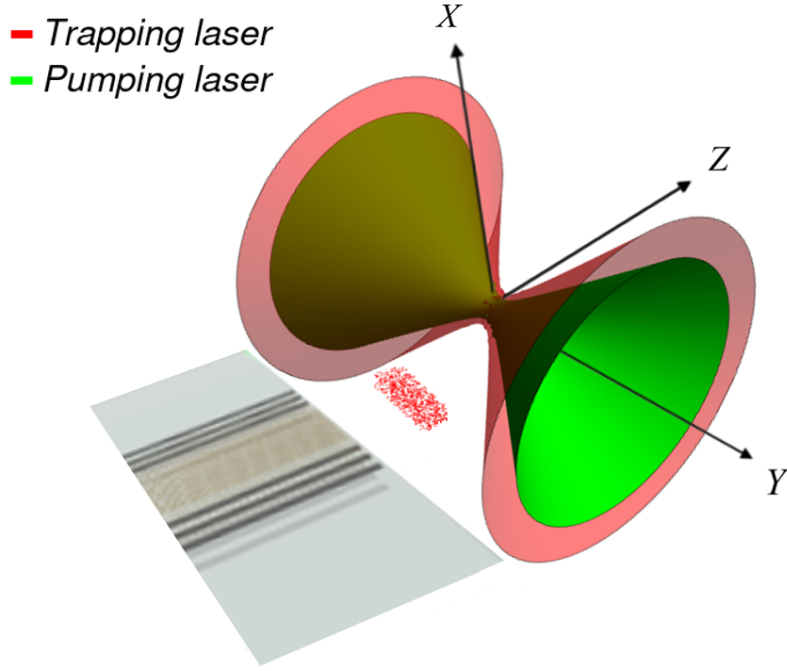
Figure 4.1: The pumping laser can be focused inside the optical trap, as its wavelength at 0.563 μm is shorter than the other at 1.071 μm. Outside its limiting surface, calculated via Eq. (4.5), the high-power laser does not damage the chip Stark decelerator.

Let us check the physical consistency of such a geometry. As reported in [70], from their laser-preparation to the chip exit, meta-stable CO molecules evolve for a time of few hundreds of μs, so that only a small fraction of them are lost by spontaneous emission. We then neglect such a fraction and we estimate their survival probability when they reach the dipole trap. By assuming the time origin when they leave the chip, their population is described by the exponential law $P_{a^3\Pi_1}(t) = e^{-\frac{t}{\tau}}$. To be conservative, we consider the worst case of a uniform Stark deceleration from the chip exit to the optical trap, leading to the longest time. In this case, they reach the trap after a period $\Delta t = \frac{2D}{v}$, where D is the minimum chip-trap distance and v is the microtrap longitudinal speed. The excited state population at this time is therefore:

$$P_{a^3\Pi_1}(v, w) = \exp\left(-\frac{2D(w)}{v}\frac{1}{\tau}\right), \tag{4.6}$$

which depends on longitudinal speed v and on the trap waist, which in turn fixes the minimum chip-trap distance via the Eq. (4.5). As shown in Fig. (4.2), the survival probability is above the 25%, so that the consistency of our setup geometry is well verified. It

is worth noting that this is just a first check, as the spontaneous emission is automatically encoded in our final simulations.
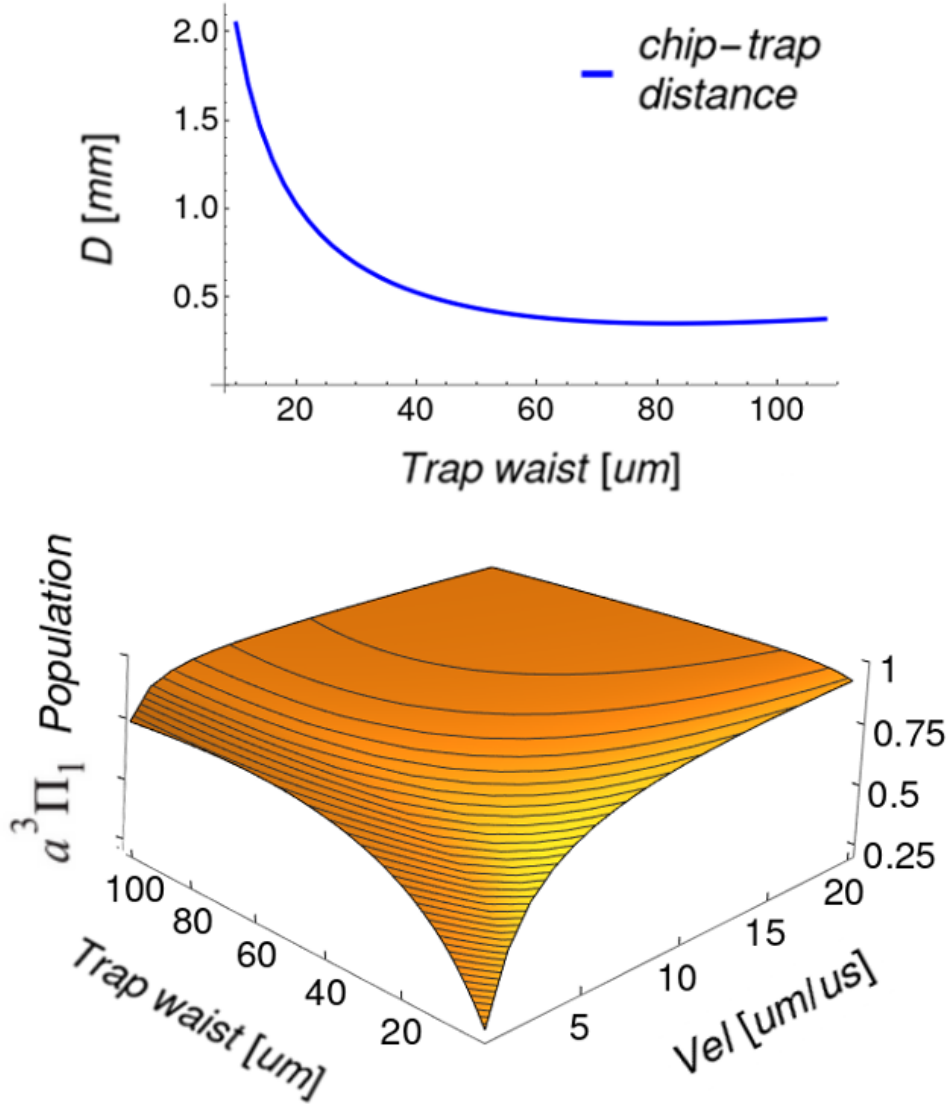

Figure 4.2: On the top it is represented the minimum chip-trap distance, accordingly to Eq. (4.5). We observe that, when the dipole trap is highly focused, the minimum distance rapidly grows up, and for a trap waist down to 10 μm it is around 2 mm. Downside, we plot the $a^3\Pi_1$ population, described by Eq.(4.6), on the parameter space spanned by the trap waist in the range [10,100] μm and by the microtrap velocities in the range [1,20] $\frac{\mu m}{\mu s}$. Apart from very slow molecules and very focused optical traps, the survival probability is close to unity.

4.3.2   Energy constraints

Meta-stable CO molecules leave the chip Stark decelerator with a mean velocity v, which can be arbitrarily chosen by tuning the microtrap speed. They can be stopped in the vacuum by the electric field barrier, when their kinetic energy is converted to the Stark energy:

$$\frac{1}{2}Mv^2 = \sqrt{\left(\frac{\mu_e E_{\text{stop}}}{2}\right)^2 + \left(\frac{\Lambda}{2}\right)^2} - \frac{\Lambda}{2}, \tag{4.7}$$

where M is the mass of CO molecules, while the right term is the Stark energy described by Eq. (4.1). As plotted in Fig. (4.3), the required electric field strength E as a function of the microtrap speed v is:

$$E_{\text{stop}}(v) = \frac{2}{\mu_e}\sqrt{\left(\frac{1}{2}Mv^2 + \frac{\Lambda}{2}\right)^2 - \left(\frac{\Lambda}{2}\right)^2}, \tag{4.8}$$
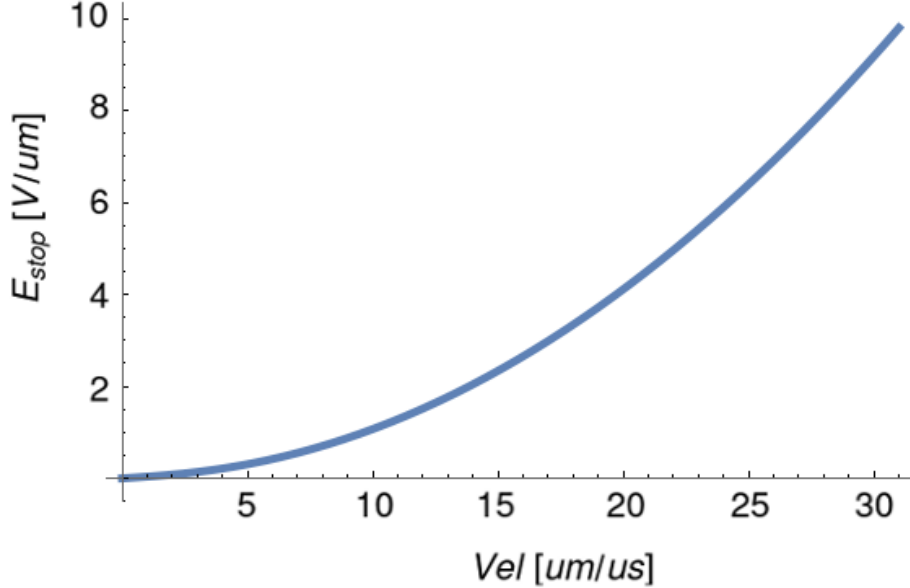

Figure 4.3: We plot the electric field strength E required to stop $a^3\Pi_1$ molecules leaving the chip VS longitudinal speed v.

Once meta-stable CO molecules are stopped, they are pumped to their absolute ground state, and they are eventually trapped in the high-power laser focus. This is described by

a Gaussian TEM_{00} mode, see Eq. (3.4), so that in the absence of the electric field barrier, the trapping potential just depends on the waist of the trapping laser, while its power is fixed to its maximum value of 240 W. As shown in Fig. (4.4), the more focused it is, the greater is its energy depth, up to about 10 mK when its waist is reduced down to 10 μm.

When the electric field barrier, needed to stop meta-stable CO molecules, is present there are two more effects to be considered. On one side, the trapping potential modifies the Stark potential, which decelerates the meta-stable CO molecules. On the other, the trapping potential is modified by the purely quadratic Stark potential, which affects the absolute ground state CO molecules.

As described by Eqs. (4.1) and (4.2) the physical potential governing the motion of meta-stable CO molecules in the low-field seeking component of the $a^3\Pi_1$ state is:

$$U_{a^3\Pi_1}(x,y,z) = \sqrt{\left(\frac{\mu_e E_B(x,y,z)}{2}\right)^2 + \left(\frac{\Lambda}{2}\right)^2} - \frac{\Lambda}{2} - \frac{1}{2}\alpha E_T^2(x,y,z), \qquad (4.9)$$

where $E_B(x,y,z)$ and $E_T(x,y,z)$ are the electric field strengths, respectively, for the electric field barrier and for the trapping laser. Therefore, if the trapping laser is highly focused it can break the rise of the Stark potential barrier, as shown in Fig. (4.5).

The other physical constraint regards CO molecules after they are pumped in their absolute ground state $X^1\Sigma^+$. When the electric field barrier and the optical trap are both considered, their trajectories obey the following potential:

$$U_{X^1\Sigma^+}(x,y,z) = -kE_B^2(x,y,z) - \frac{1}{2}\alpha E_T^2(x,y,z), \qquad (4.10)$$

where the first term describes the quadratic Stark shift, see Eq. (4.3), and the second is the trapping potential, see Eq. (4.4), which is equal for meta-stable and ground state CO molecules. The Stark effect can force absolute ground state molecules out of the optical trap, if its energy depth is not large enough, as shown in Fig (4.6).

For the trapping experiment to be feasible, the electric field barrier must exert to meta-stable CO molecules a decelerating force $F_{a^3\Pi_1}$ larger than the trapping force F_T, which in turn must be larger than the Stark force $F_{X^1\Sigma^+}$ acting on absolute ground state CO molecules, i.e.:

$$\left|\vec{F}_{X^1\Sigma^+}\right| \leq \left|\vec{F}_T\right| \leq \left|\vec{F}_{a^3\Pi_1}\right|. \qquad (4.11)$$
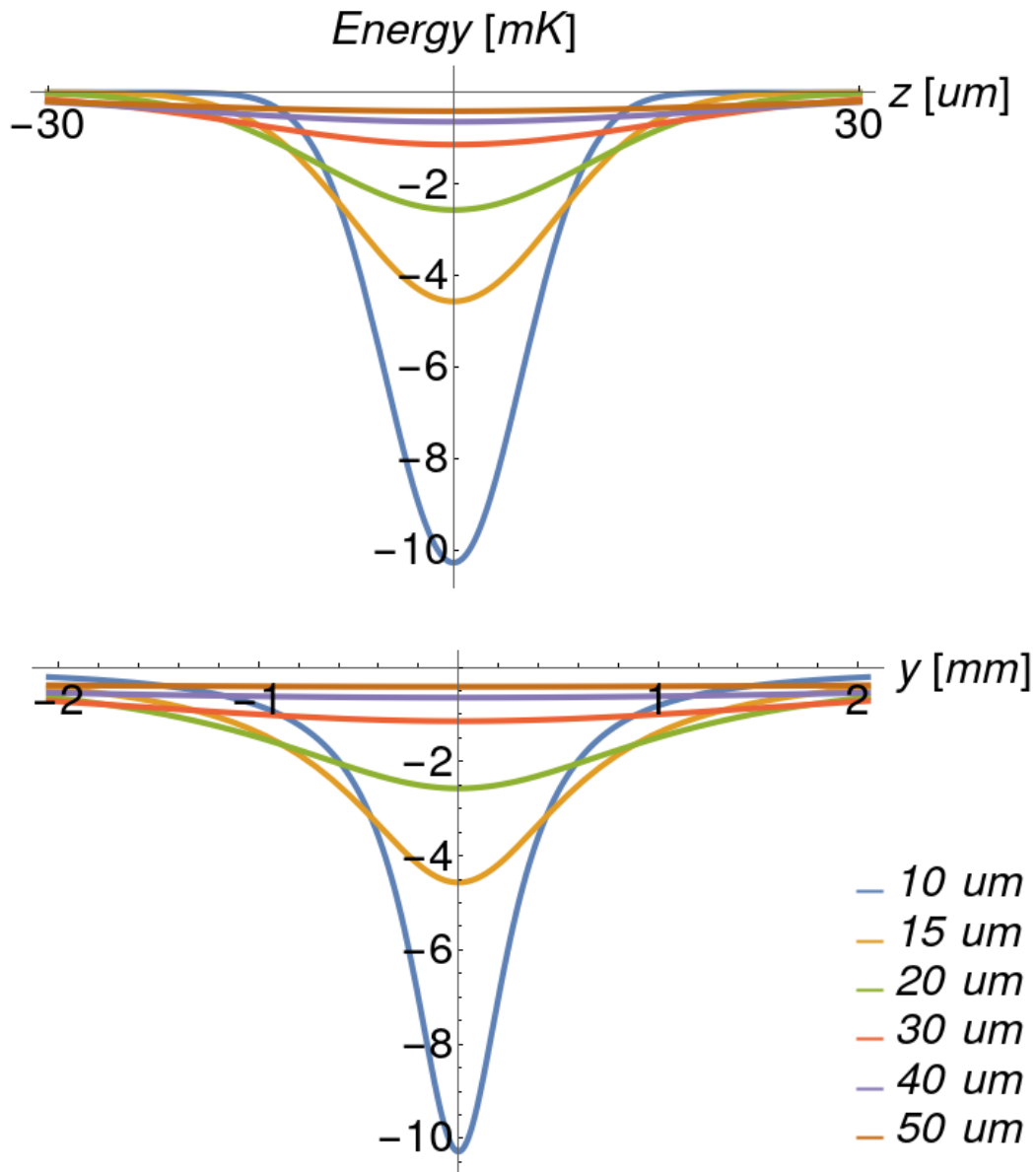
Figure 4.4: One-dimensional sections for trapping wells potentials $U(x, y, z)$ calculated for different values of the trapping laser waist 10, 15, 20, 30, 40, 50 μm, when the power of the trapping laser is fixed to its maximum value of 240 W. On the top, the sections are taken along the z-direction $U(0, 0, z)$ perpendicularly to the optical axis. Downside, they are taken along the optical trap axis $U(0, y, 0)$. More focused laser beams lead to greater energy depth up to 10 mK.
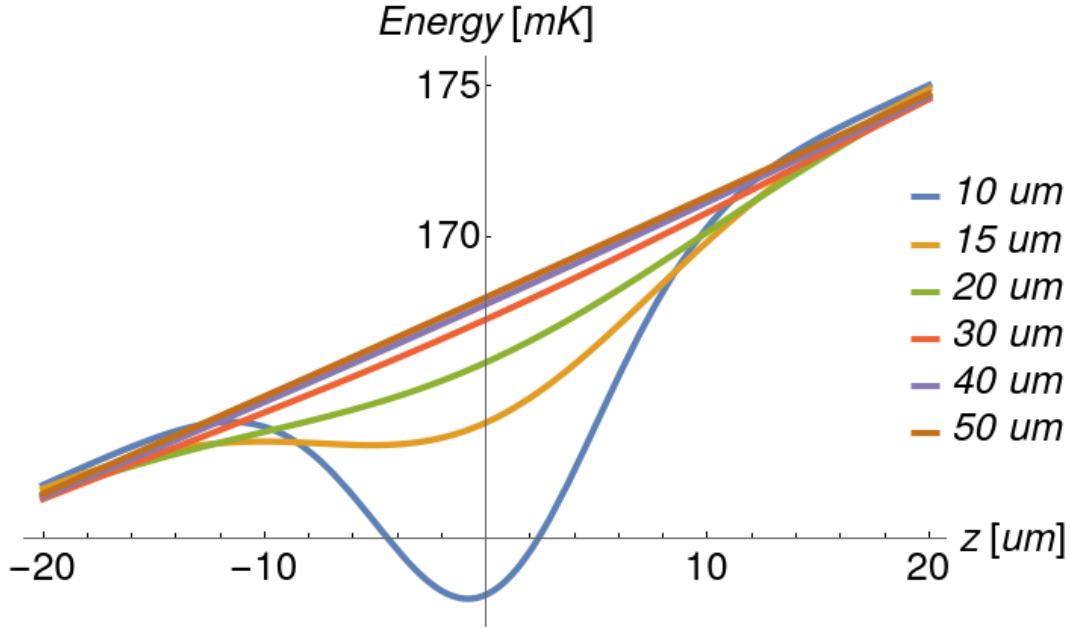
Figure 4.5: One-dimensional sections for the Stark potential barrier in the presence of the trapping laser at its maximum power of 240 W, for values of waist 10, 15, 20, 30, 40, 50 μm. The electric field barrier has been fixed to the value of about 1 $\frac{V}{\mu m}$ over a distance of 0.5 mm, which is the electric field strength needed to stop meta-stable CO molecules leaving the chip at 10 $\frac{\mu m}{\mu s}$, see Fig. (4.3).

From Eqs. (4.3) and (4.1), by using the definition $\vec{F} = -\vec{\nabla} U$, we derive the two force fields:

$$\vec{F}_{X^1\Sigma^+}(x, y, z) = -2k E_B(x, y, z) \vec{\nabla} E_B(x, y, z)$$

$$\vec{F}_{a^3\Pi_1}(x, y, z) = -\frac{(\frac{\mu_e}{2})^2 E_B(x, y, z)}{\sqrt{(\frac{\mu_e E_B(x,y,z)}{2})^2 + (\frac{\Lambda}{2})^2}} \vec{\nabla} E_B(x, y, z).$$

(4.12)

We consider the longitudinal z-direction, along which the trapping force is stronger, and we use Eqs. (4.12) to express the above relation (4.11) in the form:

$$2k E_B \left| \frac{\partial E_B}{\partial z} \right| \leq |F_{T,z}| \leq \frac{(\frac{\mu_e}{2})^2 E_B}{\sqrt{(\frac{\mu_e E_B}{2})^2 + (\frac{\Lambda}{2})^2}} \left| \frac{\partial E_B}{\partial z} \right|.$$

(4.13)

Finally, we consider the trapping force strength along the z-axis, with x=0 and y=0 and we take its maximum value F_{Max}. When it is stronger than the Stark force acting on
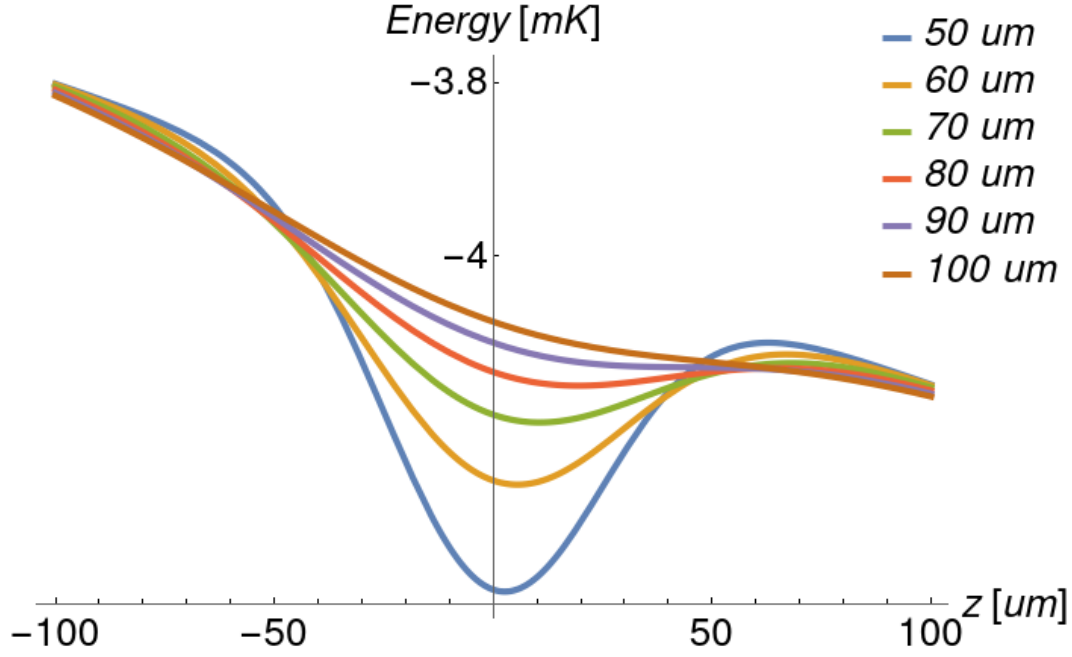
Figure 4.6: One-dimensional sections of the trapping potential for absolute ground state CO molecules, when the Stark potential barrier is considered. The waist of the trapping laser, at its maximum power of 240 W, assume the values 50, 60, 70, 80, 90, 100 μm. The electric field barrier has been chosen to achieve the value of about 10 $\frac{V}{\mu m}$ over a distance of 0.5 mm. We observe how absolute ground state CO molecules cannot be trapped if the waist is greater than 80 μm.

the absolute ground state CO molecules, the optical trapping can be performed. On the other side, when F_{Max} is lower than the Stark force decelerating incoming meta-stable CO molecules, the potential barrier is not modified. Therefore, we find for each maximum trapping force F_{Max}, a minimum and a maximum value for the z-component of the electric field gradient:

$$\left|\frac{\partial E_B}{\partial z}\right| \leq \frac{F_{Max}}{2kE_B} = \left|\frac{\partial E_B}{\partial z}\right|_{Max}$$

(4.14)

$$\left|\frac{\partial E_B}{\partial z}\right| \geq \frac{\sqrt{(\frac{\mu_e E_B}{2})^2 + (\frac{\Lambda}{2})^2}}{(\frac{\mu_e}{2})^2 E_B} F_{Max} = \left|\frac{\partial E_B}{\partial z}\right|_{Min}.$$

here the electric field strength E_B and its gradient $\frac{\partial E}{\partial z}$ are calculated at the ori-

gin (0,0,0), where the electric field barrier overlaps the trap.

For each waist of the trapping laser we calculate the maximum force F_{Max}, and for a given microtrap speed, by Eq. (4.8), we determine the required E_B to stop meta-stable CO molecules. Then, as shown in Fig. (4.7), we find the subspace of parameters for which the trapping experiment is feasible.
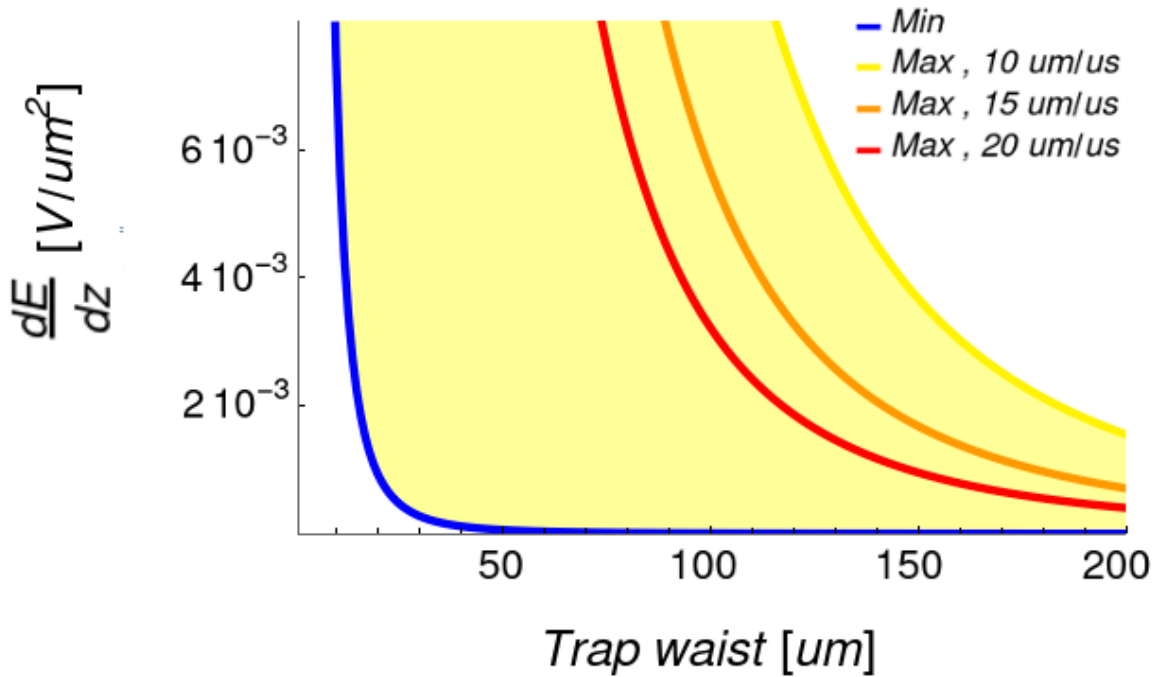

Figure 4.7: Two-dimensional section of the whole parameter space, where two parameters have been considered: the trapping laser waist and the electric field gradient along the longitudinal z-direction. The yellow region denotes the subset of parameters for which the trapping experiment is feasible. As defined by Eq.(4.14), the blue line represents the minimum value of $\left|\frac{\partial E_B}{\partial z}\right|_{Min}$, while the others represent the maximum value of $\left|\frac{\partial E_B}{\partial z}\right|_{Max}$ corresponding to the values of microtrap velocities, 10, 15 and 20 $\frac{\mu m}{\mu s}$. We observe that the incoming speed affects the maximum value and that for faster molecules the feasibility subspace is reduced.

This analysis is the starting point for our simulations, as it is a preliminary check for the experimental feasibility.

To conclude, it is worth to underline the two main approximations at the basis of the above analysis. Firstly, we only considered the electric field strength required to stop a meta-stable CO molecule characterized by a specific longitudinal speed v_z, and we did not take into account the longitudinal speed distribution of the whole incoming molecular packet. Secondly, we approximated the electric field strength E_B and gradient $\frac{\partial E}{\partial z}$ to be both constant over the dipole trap, which is a good guess provided that the electric field barrier is large as compared to the optical trap. Moreover, we did not considere the dependence on the other x and y coordinates neither as regards the trap nor as regards the electric field barrier.

These points will be considered in successive simulations, where the initial distribution of meta-stable CO molecules, leaving the chip Stark decelerator, evolves in a three-dimensional potential accounting for all these features.

4.3.3   The role of temperature

As explained previously, the low molecular density inside each microtrap prevents molecules from being in thermal equilibrium among each other. Nevertheless, as shown in Fig. (3.8), their speed distribution is very well approximated by using the Maxwell-Boltzmann distribution and we refer to the microtrap temperature T, as its best fit parameter. Therefore, given a microtrap leaving the chip at the longitudinal speed v_0 and characterized by a temperature T, its longitudinal speed distribution $\rho(v_z)$ can be described by the following one-dimensional Maxwell-Boltzmann probability distribution:

$$\rho(v_z) = \sqrt{\frac{M}{2\pi k_B T}} \exp\left(-\frac{M(v_z - v_0)^2}{2 k_B T}\right), \tag{4.15}$$

where the temperature T governs its spreading through the scale parameter:

$$\sigma = \sqrt{\frac{k_B T}{M}}. \tag{4.16}$$

Then, in order to stop a large fraction of the incoming meta-stable CO molecules inside the optical trap, the electric field strength must grow from the minimum value E_B^- to the maximum E_B^+ over the trap size, where these values are those required to stop,

respectively, slowest and fastest molecules:

$$E_B^{\pm}(v_0, T) = E_{\text{stop}}(v_0 \pm \sigma) = \frac{2}{\mu_e}\sqrt{\left(\frac{1}{2}M(v_0 \pm \sigma)^2 + \frac{\Lambda}{2}\right)^2 - \left(\frac{\Lambda}{2}\right)^2}, \tag{4.17}$$

where we used Eq. (4.8). In order to satisfy this condition, we obtain the following expression:

$$\frac{\partial E}{\partial z} = \frac{E_B^+(v_0, T) - E_B^-(v_0, T)}{2w_0}, \tag{4.18}$$

which depends on the microtrap speed v_0, its temperature T and the trap waist w_0. Therefore, we can check its consistency with the trapping experiment by using the conclusions summarized by Fig. (4.7).

As shown in Fig. (4.8), there is only one subspace of experimental parameters leading to optimal trapping, and from now on we focus on the following subset:

$w_0 \leq 100 \ \mu\text{m}$,

$T \leq 16 \ \text{mK}$,

$v_0 \leq 20 \ \mu\text{m}/\mu\text{s}$.

4.3.4   Optimal Stark deceleration

Here, we search the electric field barrier $E_{\text{B}}(x, y, z)$, by imposing that its strength and its gradient, calculated on the dipole trap focus, are the same of those defined via Eqs.(4.8). The following exponential function:

$$E_1(x, y, z) = E_1 \exp\left(\frac{\nabla_z E_1}{E_1} z\right). \tag{4.19}$$

satisfies this requirement, provided that:

$$E_1 = \frac{2}{\mu_e}\sqrt{\left(\frac{1}{2}Mv^2 + \frac{\Lambda}{2}\right)^2 - \left(\frac{\Lambda}{2}\right)^2}, \tag{4.20}$$

and

$$\nabla_z E = \frac{E_1(v_0^{\text{max}} + \sigma^{\text{max}}) - E_1(v_0^{\text{max}} - \sigma^{\text{max}})}{2w_0}, \tag{4.21}$$
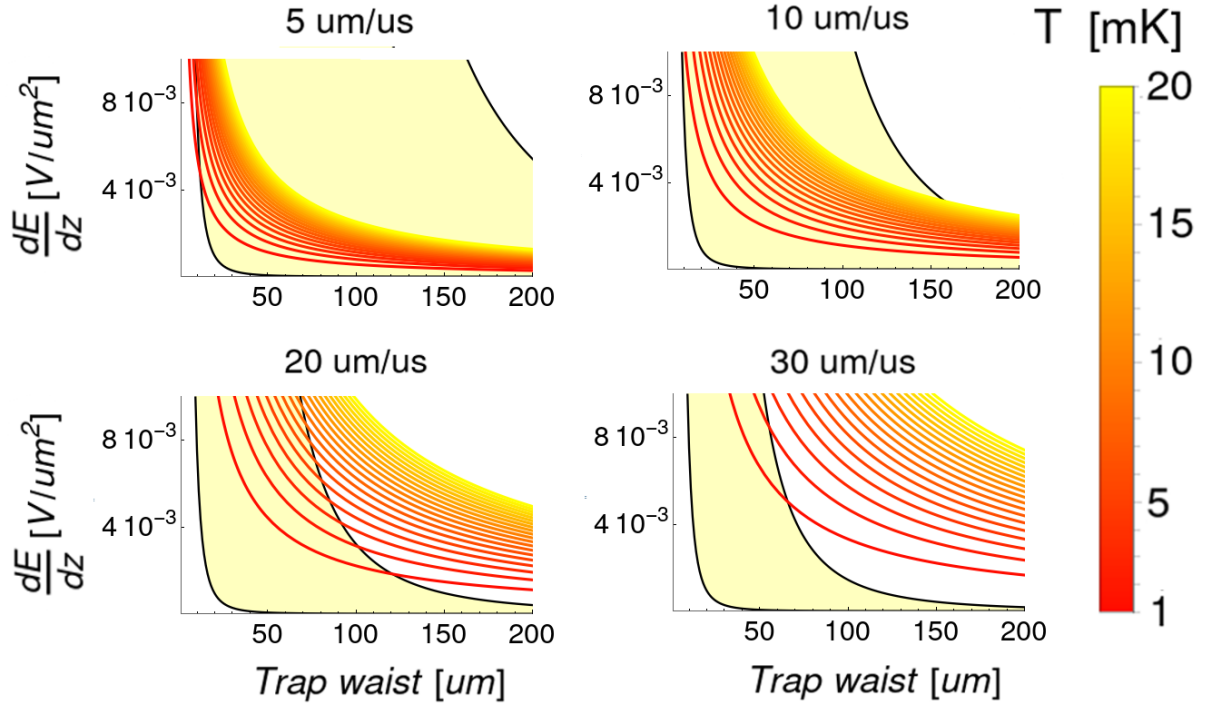
Figure 4.8: The image represents four two-dimensional sections corresponding to different values of microtrap speed: 5, 10, 20 and 30 $\frac{\mu m}{\mu s}$. The light-yellow regions denote the subspaces where the trapping experiment is feasible. We observe that their area reduces as the microtrap speed increases. The electric field gradient, described by Eq.(4.18), as a function of the trap waist, is represented for different speeds and for different microtrap temperatures T: 1, 2,...,19, 20 mK. The intersection among these functions and the feasibility regions give us accurate information on those parameters for which the trapping experiment can be more probable. We can conclude that lower microtrap temperatures are desirable, while microtrap speed higher than 20 $\frac{\mu m}{\mu s}$ are not.

with

$$\sigma^{\max} = \sqrt{\frac{k_B T^{\max}}{M}}. \tag{4.22}$$

where we choose the maximum values $v_0^{\max} = 20 \ \mu\text{m}/\mu\text{s}$ and $T^{\max} = 16$ mK, in order to ensure optimal deceleration for colder and slower molecules, while the trap waist w_0 will adapt the electric field barrier to preserve the experimental feasibility.

This electric field barrier leads to a Stark deceleration with no dependence on x and y

coordinates, while we know that the dipole trap exerts on meta-stable CO molecules an attractive force along these directions. Therefore, an improved electric field barrier could depend on them in order to contrast this effect, so that the excess of energy coming from the acceleration due to the dipole trap could be converted in Stark energy:

$$\frac{1}{2}Mv^2 = \sqrt{\left(\frac{\mu_e E_2(x,y,z)}{2}\right)^2 + \left(\frac{\Lambda}{2}\right)^2} - \frac{\Lambda}{2} - \frac{\alpha}{2}E_{\mathrm{T}}^2(x,y,z), \tag{4.23}$$

where $E_{\mathrm{opt}}(x,y,z)$ and $E_{\mathrm{T}}(x,y,z)$ are the electric field strength, respectively, of the optimal electric field barrier and of the dipole trap at the inversion point (x,y,z). Therefore, if we like to stop molecules on the dipole trap optical axis, where the trapping potential reach its maximum depth, we find the following electric field strength:

$$E_2(y) = \frac{2}{\mu_e}\sqrt{\left(\frac{1}{2}Mv^2 + \frac{\Lambda}{2} + \frac{\alpha}{2}E_{\mathrm{T}}^2(0,y,0)\right)^2 - \left(\frac{\Lambda}{2}\right)^2}, \tag{4.24}$$

where $E_{\mathrm{T}}(0,y,0)$ is the dipole trap electric field strength along its optical axis. As shown in Fig.(4.9), this correction becomes relevant for highly focused trapping laser, which are expected to perform best trapping.

By using the required electric field strength $E_2(v,y)$, we find a slightly different electric field barrier $E_2(x,y,z)$ which stops meta-stable CO molecules around the dipole trap optical axis:

$$E_2(x,y,z) = E_2(y)\exp\left(\frac{\nabla_z E}{E_2(y)}z\right). \tag{4.25}$$

To check the consequences of both found electric field barriers $E_1(x,y,z)$ and $E_2(x,y,z)$, we perform simulations of optical trapping in the limit of zero temperature, where the trapping probability must approach its highest value, limited by the probability of 28% that meta-stable CO molecules, surviving spontaneous emission, are pumped to their absolute ground state. The results are shown in Fig.(4.10).

As expected, both set of simulation yields to a maximum probability of 28%. However, the improved precision to stop CO molecules along the z-direction by most accurate electric field barrier $E_2(x,y,z)$ has the drawback of the appearance of an undesired force along the y-direction, which leads to major losses. Similar effects will manifest if the same arguments are extended to the x-direction. Therefore, we can conclude that it is better to
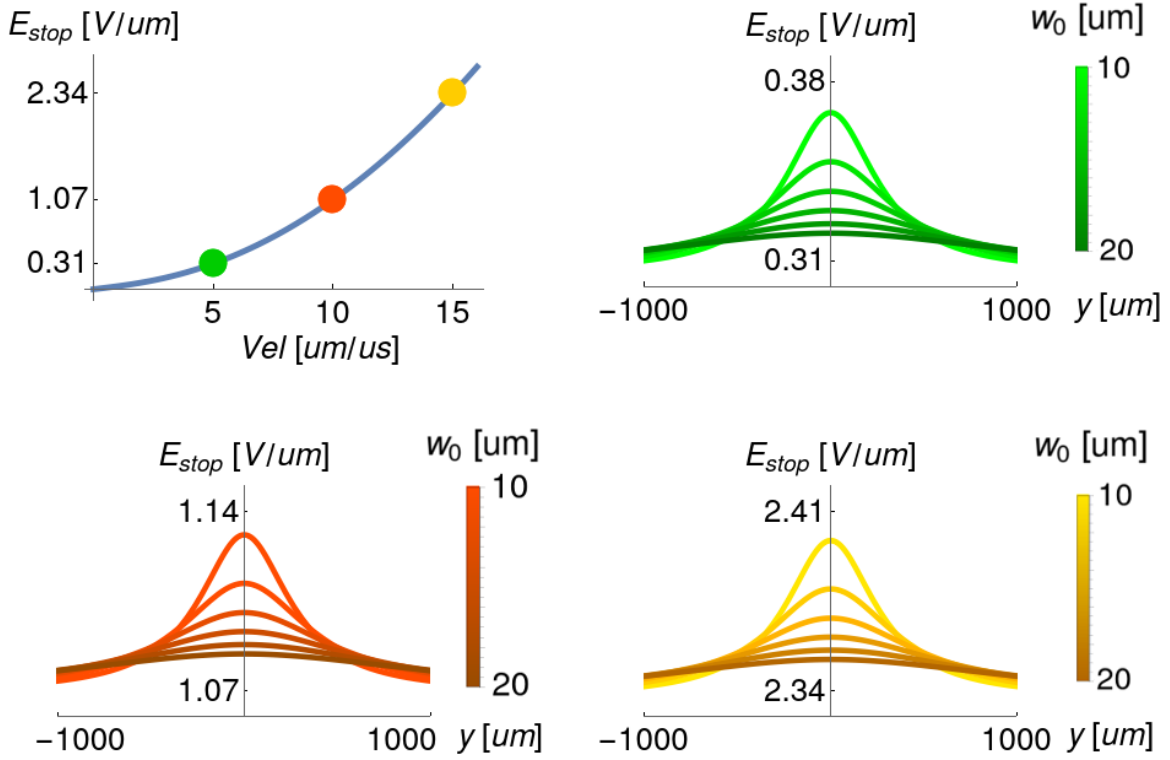
Figure 4.9: We represent two models of electric field barrier. Left side on the top, the electric field strength only depends on the incoming speed v of meta-stable CO molecules, as defined by Eq.(4.8). The other graphics represent the corrections accounted by Eq.(4.24), for which the electric field strength depends on the y-coordinate in order to balance the attractive forces arising from the dipole trap. Their profiles are represented for different values of molecular longitudinal speed $v = 5, 10, 15$ $\mu m/\mu s$ and different trap waist $w_0 = 10, 12, 14, 16, 18, 20$ μm.

have some losses coming from the simpler one-dimensional electric field barrier, which do not exactly balance the kinetic energy, than a more involved one which generates Stark forces in the other two dimensions.
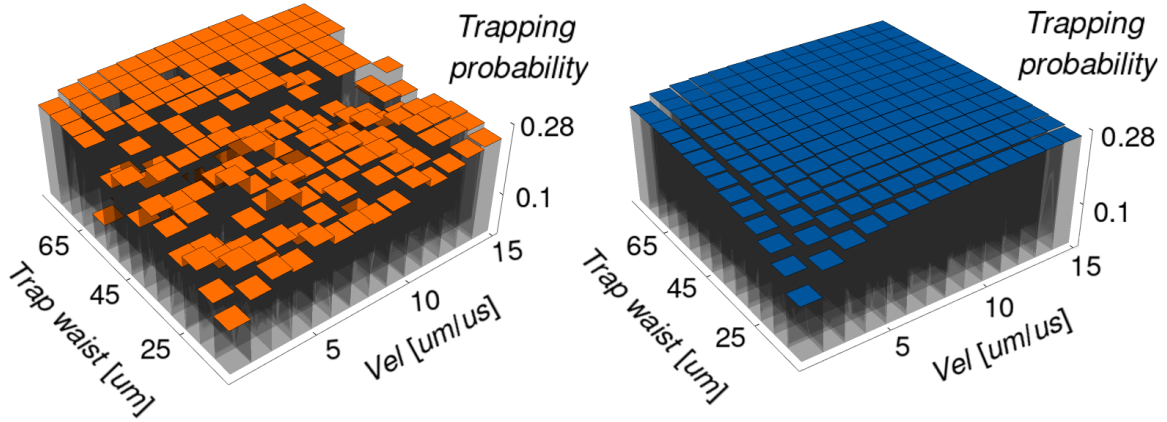
Figure 4.10: .Trapping probability prediction in the zero temperature limit for different values of trap waist and microtrap speeds. On the left, the results have been obtained by simulating the trapping experiment by using the electric field $E_2(x, y, z)$, described by Eq.(4.25). We observe how the new force in the y-direction is detrimental for optical trapping. On the right, simulations have been performed by using the simplest one-dimensional electric field barrier $E_1(x, y, z)$, defined by Eq.(4.19). For both kinds of simulations, we observe that the trapping probability is limited by spontaneous emission and they reproduce approximated results showed in Fig.(4.2).

4.4 Simulations

Here we discuss the experimental feasibility of the proposed optical trapping scheme by comparing the molecular phase-space volume with the optical dipole trap acceptance. This approach does not include many experimental details but it encodes its distinctive features and main limits. Then, we simulate how Stark deceleration highly affects the thermal distribution of the incoming meta-stable molecules, thus hindering their loading on the optical dipole trap.

4.4.1 Overlapping phase-space

Given an optimal electric field barrier stopping a large fraction of meta-stable CO molecules inside the dipole trap, we wonder what is the probability to optically trap them.

We use the results presented before in Fig. (4.2); we consider the minimum chip-trap

distance $D(w_0)$ for each trap waist w_0 and we focus on temperatures down to 1 mK, with reference to the experimental results shown in Fig. (3.8).

We need to estimate the trapping probability over the subspace of these experimental parameters:

$$P_t(w_0, v_0, T) = \frac{N_t}{N}, \tag{4.26}$$

where N_t is the number of trapped ground state CO molecules and N the total amount of meta-stable CO molecules leaving the chip.

Once meta-stable CO molecules are stopped along the longitudinal direction, we calculate the density of trapped molecules $w(x, y, z)$ at the standstill point (x, y, z) by the following expression:

$$w(x, y, z) = \int_0^{v_e(x,y,z)} \rho(x, y, z, v) dv, \tag{4.27}$$

where v is the modulus of the residual molecular speed in the x-y plane, $\rho(x, y, z, v)$ is the phase-space molecular density and $v_e(x, y, z)$ is the escape velocity calculated as:

$$v_e(x, y, z) = \sqrt{\frac{2\left|U_{X^1\Sigma^+}(x, y, z)\right|}{M}}, \tag{4.28}$$

which is obtained by imposing that the total energy is zero:

$$\frac{1}{2}Mv^2 + U_{X^1\Sigma^+}(x, y, z) = 0, \tag{4.29}$$

where $U_{X^1\Sigma^+}(x, y, z)$ is defined by Eq. (4.10). The density $w(x, y, z)$ in fact tell us how many molecules in the point (x, y, z) have negative total energy so that they can be trapped.

Then, to obtain the total number of trapped molecules, we integrate the density of trapped molecules $w(x, y, z)$ over the whole space:

$$N_t = \int_{\mathbb{R}^3} w(x, y, z) \, dx \, dy \, dz = \int_{\mathbb{R}^3} \int_0^{v_e(x,y,z)} \rho(x, y, z, v) \, dv \, dx \, dy \, dz. \tag{4.30}$$

The total number of molecules N is formally expressed as follows:

$$N = \int_{\mathbb{R}^3} \int_0^\infty \rho(x, y, z, v) \, dv \, dx \, dy \, dz. \tag{4.31}$$

Now, we assume that the molecular speed distribution is independent of the molecular space density, so that the joint density distribution is the product of their marginal distributions $\rho(x, y, z, v) = \rho(x, y, z)\rho(v)$. From a mathematical point of view, this hypothesis is very appealing as it greatly simplifies our calculations. Physically, it is correct as long as molecules move inside the microtraps, and when they start to freely expand in the vacuum a correlation between positions and speeds have to be expected. In fact, faster molecules more probably reach higher distances. This correlation will be automatically encoded later on in our trajectory simulations. Moreover, the molecular space density is assumed to be homogeneous at each time.

We then obtain the much simpler expression for the trapping probability:

$$P_t = \frac{N_t}{N} = \frac{\int_{\mathbb{R}^3} dx\; dy\; dz \int_0^{v_e(x,y,z)} \rho(v)\; dv}{\int_{\mathbb{R}^3} dx\; dy\; dz}, \tag{4.32}$$

where the homogeneous molecular density takes out from the integrals and cancels out. Furthermore, we extend the spatial integration only over the molecular cloud volume V, freely expanded in the vacuum in the x-y plane until the longitudinal motion is stopped on the dipole trap:

$$P_t = \frac{1}{V} \int_V dx\; dy\; dz \int_0^{v_e(x,y,z)} \rho(v)\; dv. \tag{4.33}$$

Finally, once established the molecular packet volume V and the speed distribution $\rho(v)$, this integral can be numerically calculated. The volume V depends on the chip-trap time of flight Δt and on the free expansion rate governed by the temperature T. As the time of flight depends on the microtrap speed v_0 and on the chip-trap minimum distance $D(w_0)$, the volume is a function of three parameters $V(w_0, v_0, T)$. In order to predict an upper limit for the trapping probability, we set the time of flight to its minimum value $\Delta t = \frac{D(w_0)}{v_0}$.

Finally, concerning the speed distribution $\rho(v)$, we use the following two-dimensional Maxwell-Boltzmann distribution:

$$\rho_T(v) = 2\pi v \left(\frac{M}{2\pi k_B T} \right) \exp\left(-\frac{M}{2k_B T} v^2 \right), \tag{4.34}$$

where we considered a motion in the x-y plane involving the residual transverse speed $v = \sqrt{v_x^2 + v_y^2}$. By numerically calculating the integral at Eq. (4.33), we obtain the results shown in Figs. (4.11) and (4.12).
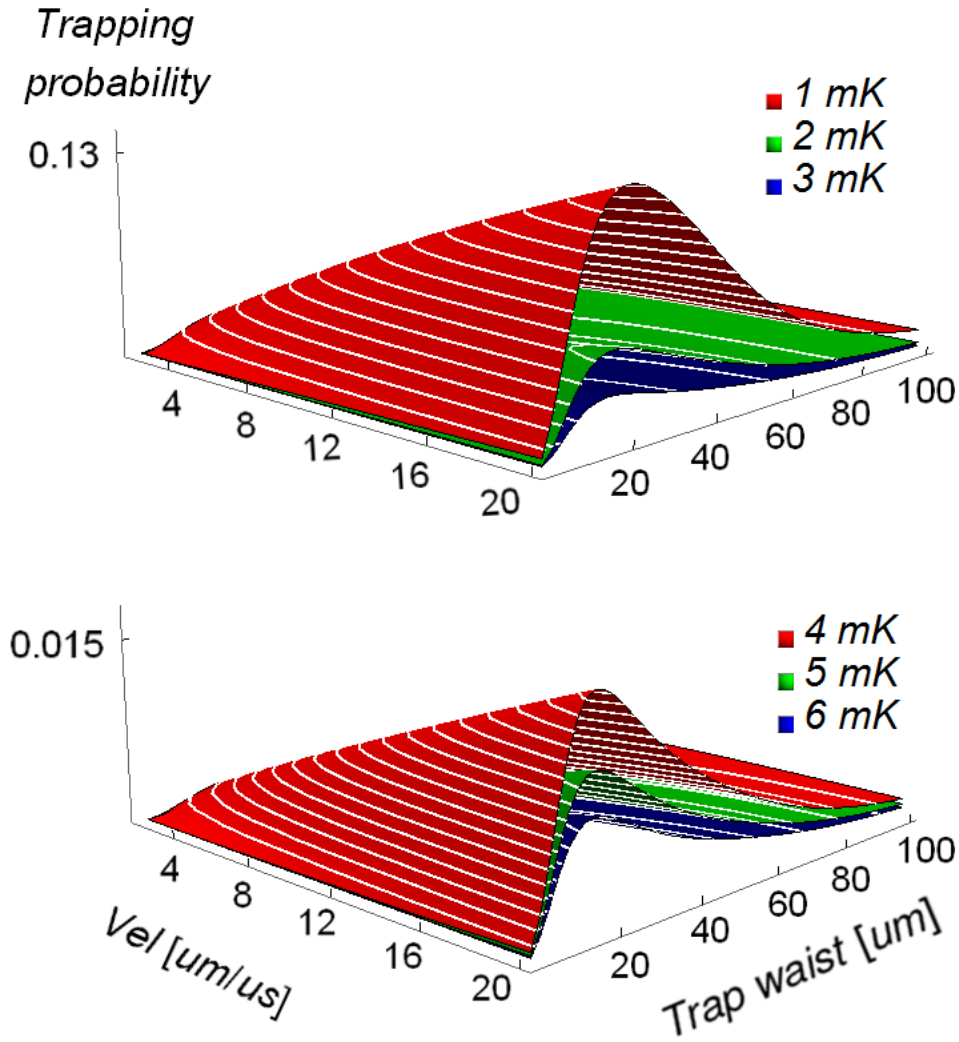
Figure 4.11: Different sections of the trapping probability P_t are shown for various microtrap temperature: 1,2,3,4,5,6 mK. We observe that from 1 mK to 4 mK, the trapping probability P_t decreases by about one order of magnitude. As expected, by increasing the microtrap speed, P_t grows as the spatial overlapping between the molecular cloud and the dipole trap is much more effective. Furthermore, P_t critically depends on the trap waist, with its maximum corresponding to a value about 20 μm.

We observe that the trapping probability rapidly decreases for temperatures around 10 mK, for which $P_t \sim 0.003$. We conclude that the longitudinal speed distribution $\rho(v_z)$, characterizing the meta-stable CO molecules leaving the chip, critically affects the probability to successfully load them on the dipole trap. Specifically, we predicted a
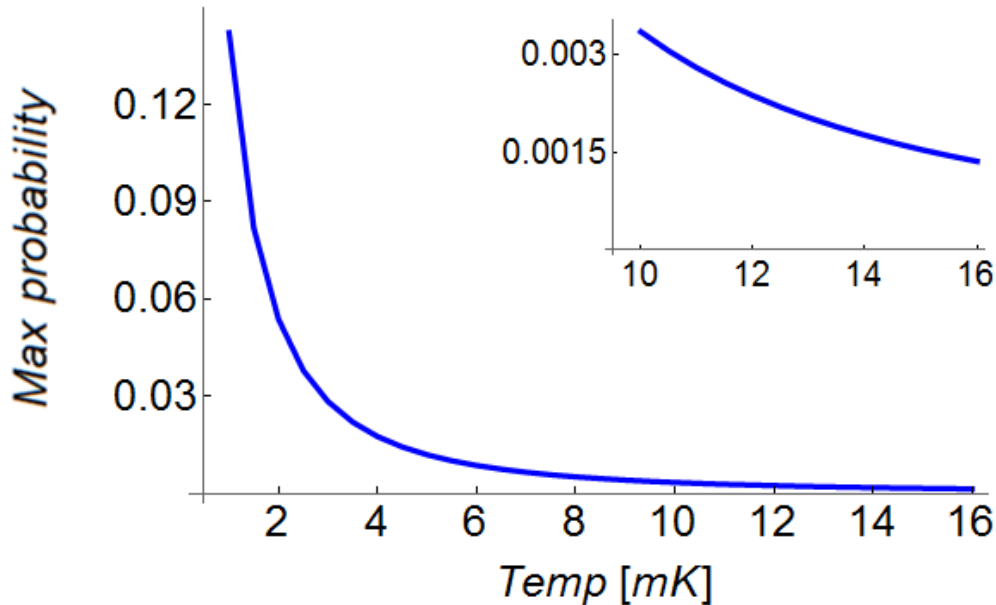
Figure 4.12: For each temperature, we calculated the maximum trapping probability over the two-dimensional subspace generated by the trap waist and the microtrap speed parameters.

trapping probability down to about 1% for molecules characterized by a small temperature of few mK in the case of a highly focused dipole trap with a waist down to 20 μm. Nevertheless, till now, we did not considere the detrimental role coming from the Stark deceleration and the ground state optical pumping on the final temperature of absolute ground state CO molecules. This will further lower the expected trapping probability.

4.4.2   The role of Stark deceleration

So far, we did not explicitly take into account the role of the ground state optical pumping. Here, we focus on its consequences which critically affect the whole trapping experiment.

Till now, we hypothesised that all the excited CO molecules can be Stark decelerated to a standstill and subsequently transferred to the ground state. As we explained before, see Fig. (4.8), it is certainly true that all of them can be stopped within the dipole trap by suitably choosing the Stark electric field barrier. However, it is not possible to contemporarily drive them to the ground state by exploiting a continuous-wave laser beam. The reason is very simple. Suppose that the pumping laser overlaps the dipole trap, so

that excited molecules transit to the ground state where they cross it. Since the excited molecules have not the same translational kinetic energy in the longitudinal direction, some of them reach it when they stop, others transit to the ground state when they are still fast and some others do not reach the RDL at all, because they stop earlier. Therefore, regardless to the precise quantum dynamics by which excited molecules are pumped to their ground state, it is not possible to simultaneously control all of them. The best we can do is just maximize the number of slow ground state molecules. Towards this goal, here we analyse the effect of the optical pumping on the longitudinal speed distribution of ground state CO molecules. Then, we discuss how this probability distribution generally affects the trapping experiment, as the microtrap speed and temperature are varied. In particular, we demonstrate that higher microtrap speeds are detrimental, conversely to the results presented above in Fig. (4.11), where we showed how faster microtraps were preferable thanks to the greater spatial overlapping between the dipole trap and the molecular clouds. In other words, a compromise between two opposite behaviours have to be found about the microtrap speed in order to maximize the trapping probability.

The disadvantageous aspect of an increasing microtrap speed can be easily understood as follows. Imagine two molecular clouds, leaving the chip with two different longitudinal speeds $v_1 < v_2$, but characterized by the same temperature T. We can describe their thermal motion around their mean values v_1 and v_2 by using the following probability density functions:

$$\rho_1(v_z) = \sqrt{\frac{M}{2\pi k_B T}} e^{-\frac{M}{2k_B T}(v_z - v_1)^2} \qquad \rho_2(v_z) = \sqrt{\frac{M}{2\pi k_B T}} e^{-\frac{M}{2k_B T}(v_z - v_2)^2}. \tag{4.35}$$

Now, for each molecular cloud we choose a Stark electric field barrier stopping their mean speed exactly where the RDL drives molecules to the ground state. We consider two molecules belonging to the first and to the second molecular cloud and travelling, respectively, at $v_{z,1} = v_1 + \epsilon$ and $v_{z,2} = v_2 + \epsilon$. The probability to find these two molecules is exactly the same. Then, we wonder which speeds they have, when they cross the RDL and transit to the ground state. Since their kinetic energies are converted to Stark energy until they reach the RDL, the two velocities are the following:

$$v_{z,1}^{\mathrm{RDL}} = \epsilon\sqrt{1 + \frac{2v_1}{\epsilon}} \qquad v_{z,2}^{\mathrm{RDL}} = \epsilon\sqrt{1 + \frac{2v_2}{\epsilon}}, \tag{4.36}$$

where $v_{z,1}^{\mathrm{RDL}} < v_{z,2}^{\mathrm{RDL}}$ so that the probability to trap the first molecule is clearly higher.

This simple argument evidently shows an aspect for which slower microtraps have to be rather desirable.

Let us now quantitatively analyse this phenomenon. Our purpose is to find the probability density function $\rho_{ij}^{(g)}(v_z)$ describing the longitudinal speeds of ground state CO molecules for different values of microtrap velocities and temperatures, v_i and T_j. We start by generating, for each couple (v_i, T_j), a statistical ensemble of excited molecules, whose longitudinal motion is described by the following density probability function:

$$\rho_{ij}^{(e)}(v_z) = \sqrt{\frac{M}{2\pi k_B T_j}} \exp\left(-\frac{M}{2k_B T_j}(v_z - v_i)^2\right). \tag{4.37}$$

Then, for each excited molecule, we simulate its Stark deceleration until it reaches the RDL, where it is driven to the ground state. In particular the electric field barrier stops molecules with the speed v_i, exactly where there is the RDL, so that only faster molecules are transferred to the ground state. For simplicity, we model the RDL as driving quantum transitions instantaneously if the molecules overcome a specific z-coordinate. Now, it is clear that the RDL has not a spatially discontinuous boundary, as its intensity drops to zero continuously, so that its real shape is expected to slightly correct the specific positions at which excited molecules are pumped to the ground state. Nevertheless, such a correction does not compromise the main findings of our analysis, which is largely independent on this particular aspect. Furthermore, we are assuming that the RDL acts instantaneously on excited molecules, but this approximation is very well verified. Indeed, the time-scale of the optical pumping is of the order of tens of ns, then being negligible as compared to the hundreds of μs, which characterize the Stark deceleration dynamics. Now, by starting from a set of different statistical molecular ensembles, belonging to the corresponding set of probability density functions $\rho_{ij}^{(e)}(v_z)$, we evolve all of them until they reach the RDL. Then, we focus on their longitudinal speeds and we fit these ensembles by using a probability density function with the same form:

$$\rho_{ij}^{(g)}(v_z) = \sqrt{\frac{M}{2\pi k_B T_j'}} \exp\left(-\frac{M}{2k_B T_j'}(v_z - v_i')^2\right), \tag{4.38}$$

where T_j' and v_i' are the best fit parameters, representing the temperature and mean speed of ground state CO molecules, immediately after their transition.

From the reasoning above, see Eq. (4.36), we expect to obtain values of (v_i', T_j'), growing with the increasing values of microtrap speed and temperature (v_i, T_j). By looking at Fig. (4.13) and (4.14), we indeed observe such a phenomenon.
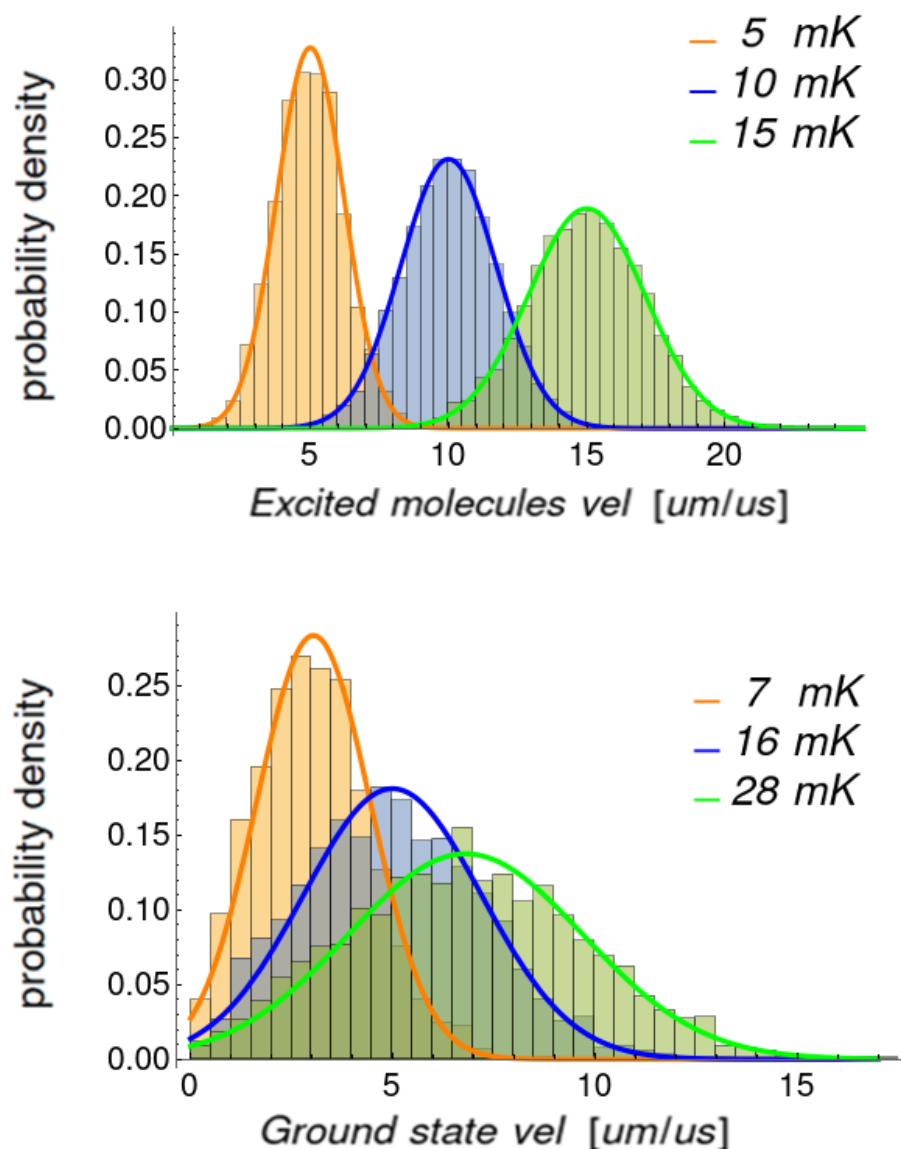
Figure 4.13: On the top, the three histograms represent the ensemble of the longitudinal speed for the excited CO molecules leaving microtraps moving at 5, 10, 15 $\frac{\mu m}{\mu s}$ with three different temperature of 5, 10, 15 mK. The three envelops are the corresponding probability density functions, described at Eq. (4.37). Down, the histograms represent the longitudinal velocities of those molecules which have been transferred to the ground state. We observe that as the microtrap speed and temperature grow, the corresponding distributions of ground state molecules have higher temperature and mean velocity.

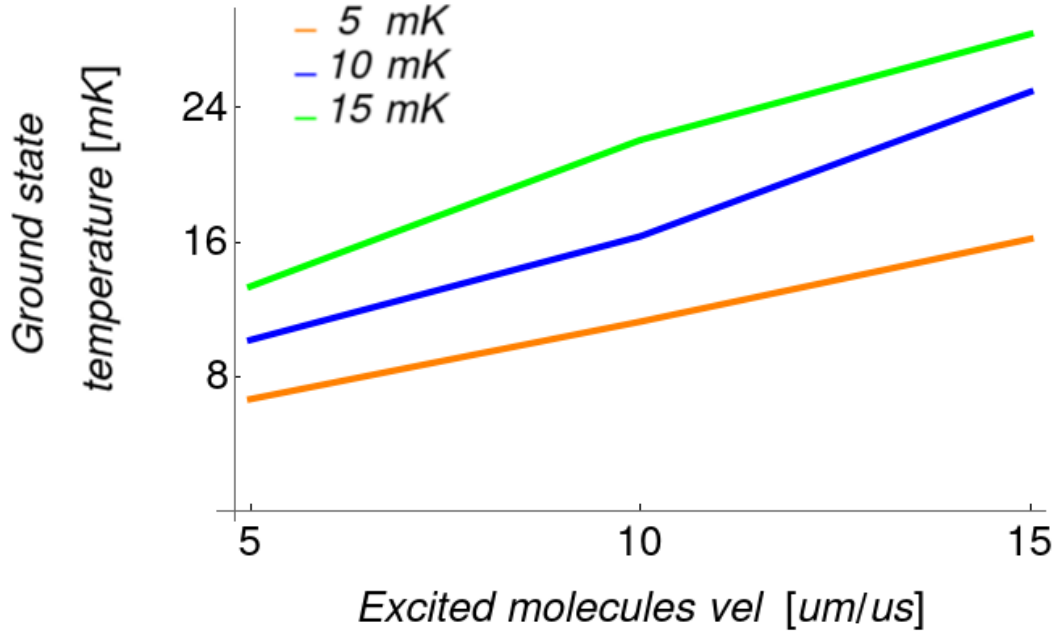Figure 4.14: We represent how the best fit temperature parameter, characterizing the probability density function for ground state CO molecules, depends on the microtrap's velocity for different choices of microtrap's temperature of 5,10,15 mK. We see that higher microtrap speed leads to increasing effective temperature for ground state molecules. Then from this point of view, faster microtraps are detrimental for the trapping experiment.

4.4.3   Maximum trapping probability

We simulate the whole cycle experiment in order to obtain a reliable estimation for the upper limit of the trapping probability. Starting from molecular distributions of meta-stable CO molecules leaving the chip Stark decelerator, we simulate their trajectories until they reach the pumping laser, which drives them to their absolute ground state, and we establish how many of them can be loaded in the dipole trap. We encode all the physical constraints discussed above to predict the trapping probability over the space of free parameters, representing the optimal setup conditions. Trajectory simulations account contemporarily for all detrimental aspects, as the spontaneous emission phenomena, the effect of Stark deceleration on the molecular phase-space distribution or the role of the pumping laser, which transfer only few molecules to their absolute ground state. There-

fore, we expect a lower value of the achievable trapping probability per experimental cycle. By focusing on most promising experimental values of trap waist and microtrap velocities, we find a maximum trapping probability about 10^{-4}. Then, if we have less than 100 CO molecules leaving the chip Stark decelerator, we expect to optically trap about 0.01 molecules in their absolute ground state per cycle experiment. Therefore, as the trapping experiment is characterized by a repetition rate of 10 Hz, we predict an accumulation rate of about of 0.1 s^{-1}, which is greater than the rate at which blackbody radiation pumps molecules out of their absolute ground state, but it is far behind the observation threshold.

4.5   Conclusions

We assessed the feasibility of a novel approach to capture ground-state CO molecules in an optical dipole trap. Such approach involves the use of a molecular beam of metastable CO, a microstructured Stark decelerator, static electrodes, and a series of lasers, pulsed and cw. The optimization of all parameters is a complex task due to the large number of degrees of freedom and their mutual relations. Thus, a brute force approach is not feasible and we sought some insight in the individual role of each parameters and its relations with the others. We reduced as much as possible the number of independent free parameters and we focused on the physical constraints underlying the experimental feasibility. On this basis, we searched for the optimal setup by evaluating the trapping probability over different sub-spaces of independent parameters, each of those evidencing a particular physical aspect. We explored each setup configuration with trajectory simulations. We concluded that this approach yields a rate of about 0.1 trapped molecules per second, which is very low, especially considering the complexity of the setup.

However, the motivation to trap an ensemble of ground-state molecules in an optical dipole trap remains strong because it would be a good basis for sympathetic cooling using a bath of ultracold atoms. Therefore, the work reported here can be applied to similar studies and the simulations developed throughout this work can be generalized to other scheme of optical trapping experiments.

Bibliography

[1] A. Peters, Y. K. Chung, and S. Chu. Measurement of gravitational acceleration by dropping atoms. *Nature*, 400:849, 1999.

[2] M. Cadoret, E. de Mirandes, P. Cladé, S. Guellati-Khélifa, C. Schwob, F. Nez, L. Julien, and F. Biraben. Combination of bloch oscillations with a ramsey-bordé interferometer: New determination of the fine structure constant. *Physical review letters*, 101:230801, 2008.

[3] C. G. Parthey, A. Matveev, J. Alnis, B. Bernhardt, A. Beyer, R. Holzwarth, A. Maistrou, R. Pohl, K. Predehl, T. Udem, T. Wilken, N. Kolachevsky, M. Abgrall, D. Rovera, C. Salomon, P. Laurent, and T. W. Hänsch. Improved measurement of the hydrogen $1s - 2s$ transition frequency. *Physical review letters*, 107:203001, 2011.

[4] K. Pachucki, V. Patkóš, and V. Yerokhin. Testing fundamental interactions on the helium atom. *Physical Review A*, 95:062510, 2017.

[5] P. J. Mohr, D. B. Newell, and B. N. Taylor. Codata recommended values of the fundamental physical constants: 2014. *Reviews of Modern Physics*, 88:035009, 2016.

[6] D. Hanneke, S. Hoogerheide, and G. Gabrielse. New measurement of the electron magnetic moment and the fine structure constant. *Physical review letters*, 100:120801, 2008.

[7] F. Biraben. Spectroscopy of atomic hydrogen. *The European Physical Journal Special Topics*, 172:109–119, 2009.

[8] S. Sturm, F. Köhler, J. Zatorski, A. Wagner, Z. Harman, G. Werth, W. Quint, C. Keitel, and K. Blaum. High-precision measurement of the atomic mass of the electron. *Nature*, 506:467–470, 2014.

[9] T. Rosenband, D. B. Hume, P. O. Schmidt, C. W. Chou, A. Brusch, L. Lorini, W. H. Oskay, R. E. Drullinger, T. M. Fortier, J. E. Stalnaker, S. A. Diddams, W. C. Swann, N. R. Newbury, W. M. Itano, D. J. Wineland, and J. C. Bergquist. Frequency ratio of Al$^+$ and Hg$^+$ single-ion optical clocks; metrology at the 17th decimal place. *Science*, 319:1808–1812, 2008.

[10] M. Fischer, N. Kolachevsky, M. Zimmermann, R. Holzwarth, Th. Udem, T. W. Hänsch, M. Abgrall, J. Grünert, I. Maksimovic, S. Bize, H. Marion, F. Santos Pereira Dos, P. Lemonde, G. Santarelli, P. Laurent, A. Clairon, C. Salomon, M. Haas, U. D. Jentschura, and C. H. Keitel. New limits on the drift of fundamental constants from laboratory measurements. *Physical review letters*, 92:230802, 2004.

[11] E. Peik, B. Lipphardt, H. Schnatz, T. Schneider, C. Tamm, and S. Karshenboim. Limit on the present temporal variation of the fine structure constant. *Physical review letters*, 93:170801, 2004.

[12] S. Bize, P. Laurent, M. Abgrall, H. Marion, I. Maksimovic, L. Cacciapuoti, J. Grünert, C. Vian, F. Pereira dos Santos, P. Rosenbusch, P. Lemonde, G. Santarelli, P. Wolf, A. Clairon, A. Luiten, M. Tobar, and C. Salomon. Cold atom clocks and applications. *Journal of Physics B: Atomic, Molecular and Optical Physics*, 38:S449–S468, 2005.

[13] S. Blatt, A. D. Ludlow, G. K. Campbell, J. W. Thomsen, T. Zelevinsky, M. M. Boyd, J. Ye, X. Baillard, M. Fouché, R. Le Targat, A. Brusch, P. Lemonde, M. Takamoto, F. L. Hong, H. Katori, and V. V. Flambaum. New limits on coupling of fundamental constants to gravity using ^{87}Sr optical lattice clocks. *Physical review letters*, 100:140801, 2008.

[14] T. L. Nicholson, S. L. Campbell, R. B. Hutson, G. E. Marti, B. J. Bloom, R. L. McNally, W. Zhang, M. D. Barrett, M. S. Safronova, and G. F. Strouse. Systematic evaluation of an atomic clock at 2×10^{-18} total uncertainty. *Nature communications*, 6:6896, 2015.

[15] M. R. Tarbutt, B. E. Sauer, J. J. Hudson, and E. A. Hinds. Design for a fountain of ybf molecules to measure the electron's electric dipole moment. *New Journal of Physics*, 15:053034, 2013.

[16] D. M. Kara, I. J. Smallman, J. J. Hudson, B. E. Sauer, M. R. Tarbutt, and E. A. Hinds. Measurement of the electrons electric dipole moment using YbF molecules: methods and data analysis. *New Journal of Physics*, 14:103051, 2012.

[17] J. Lim, J. R. Almond, M. A. Trigatzis, J. A. Devlin, N. J. Fitch, B. E. Sauer, M. R. Tarbutt, and E. A. Hinds. Laser cooled ybf molecules for measuring the electron's electric dipole moment. *Physical review letters*, 120:123201, 2018.

[18] J. J. Hudson, D. M. Kara, I. J. Smallman, B. E. Sauer, M. R. Tarbutt, and E. A. Hinds. Improved measurement of the shape of the electron. *Nature*, 473:493, 2011.

[19] A. C. Vutha, W. C. Campbell, Y. V. Gurevich, N. R. Hutzler, M. Parsons, D. Patterson, E. Petrik, B. Spaun, J. M. Doyle, G. Gabrielse, and D. DeMille. Search for the electric dipole moment of the electron with thorium monoxide. *Journal of Physics B: Atomic, Molecular and Optical Physics*, 44:079803, 2011.

[20] M. G. Kozlov and D. DeMille. Enhancement of the electric dipole moment of the electron in PbO. *Physical review letters*, 89:133001, 2002.

[21] K. Beloy, A. Borschevsky, P. Schwerdtfeger, and V. V. Flambaum. Enhanced sensitivity to the time variation of the fine-structure constant and m_p/m_e in diatomic molecules: A closer examination of silicon monobromide. *Physical Review A*, 82:022106, 2010.

[22] C. Chin, V. V. Flambaum, and M. G. Kozlov. Ultracold molecules: new probes on the variation of fundamental constants. *New Journal of Physics*, 11:055048, 2009.

[23] M. G. Kozlov and L. N. Labzowsky. Parity violation effects in diatomics. *Journal of Physics B: Atomic, Molecular and Optical Physics*, 28:1933, 1995.

[24] D. DeMille, S. B. Cahn, D. Murphree, D. A. Rahmlow, , and M. G. Kozlov. Using molecules to measure nuclear spin-dependent parity violation. *Physical review letters*, 100:023003, 2008.

[25] V. V. Flambaum and J. S. M. Ginges. Resonance reactions and enhancement of weak interactions in collisions of cold molecules. *Physical Review A*, 74:025601, 2006.

[26] H. Fesbach. Theoretical nuclear physics: nuclear reactions. *Physics Today*, 45:84, 1992.

[27] C. Chin, R. Grimm, P. Julienne, and E. Tiesinga. Feshbach resonances in ultracold gases. *Reviews of Modern Physics*, 82:1225, 2010.

[28] J. Bochinski, E. Hudson, H. Lewandowski, and J. Ye. Cold free radical molecules in the laboratory frame. *Physical Review A*, 70:043410, 2004.

[29] E. Tiesinga, B. J. Verhaar, and H. T. C. Stoof. Threshold and resonance phenomena in ultracold ground-state collisions. *Physical Review A*, 47:4114, 1993.

[30] P. Courteille, R. S. Freeland, D. J. Heinzen, F. A. Van Abeelen, and B. J. Verhaar. Observation of a feshbach resonance in cold atom scattering. *Physical Review Letters*, 81:69, 1998.

[31] T. V. Tscherbul, Y. V. Suleimanov, V. Aquilanti, and R. V. Krems. Magnetic field modification of ultracold molecule–molecule collisions. *New Journal of Physics*, 11:055021, 2009.

[32] M. Ortner, A. Micheli, G. Pupillo, and P. Zoller. Quantum simulations of extended hubbard models with dipolar crystals. *New Journal of Physics*, 11:055045, 2009.

[33] T. Ohgoe, T. Suzuki, and N. Kawashima. Novel mechanism of supersolid of ultracold polar molecules in optical lattices. *Journal of the Physical Society of Japan*, 80:113001, 2011.

[34] J. Levinsen, N. R. Cooper, and G. V. Shlyapnikov. Topological p x+ ip y superfluid phase of fermionic polar molecules. *Physical Review A*, 84:013603, 2011.

[35] N. R. Cooper and G. V. Shlyapnikov. Stable topological superfluid phase of ultracold polar fermionic molecules. *Physical review letters*, 103:155302, 2009.

[36] S. V. Syzranov, M. L. Wall, V. Gurarie, and A. M. Rey. Spin–orbital dynamics in a system of polar molecules. *Nature communications*, 5:5391, 2014.

[37] B. Yan, S. A. Moses, D. S. Jin, A. M. Rey, J. P. Covey, J. Ye, K. R. A. Hazzard, and B. Gadway. Realizing a lattice spin model with polar molecules. *Nature*, 501:7468, 2013.

[38] R. P. Feynman. Simulating physics with computers. *International Journal of theoretical physics*, 21:467–488, 1982.

[39] A. Micheli, G. K. Brennen, and P. Zoller. A toolbox for lattice-spin models with polar molecules. *Nature Physics*, 2:341, 2006.

[40] L. Carr, D. DeMille, R. Krems, and J. Ye. Cold and ultracold molecules: science, technology and applications. *New Journal of Physics*, 11:055049, 2009.

[41] G. Pupillo, A. Griessner, A. Micheli, M. Ortner, D-W. Wang, and P. Zoller. Cold atoms and molecules in self-assembled dipolar lattices. *Physical review letters*, 100:050402, 2008.

[42] H. P. Büchler, E. Demler, M. Lukin, A. Micheli, N. Prokof'ev, G. Pupillo, and P. Zoller. Strongly correlated 2d quantum phases with cold polar molecules: Controlling the shape of the interaction potential. *Physical review letters*, 98:060404, 2007.

[43] J. Blackmore, L. Caldwell, P. Gregory, E. Bridge, R. Sawant, J. Aldegunde, J. Mur-Petit, D. Jaksch, J. M Hutson, B. Sauer, M. Tarbutt, and S. Cornish. Ultracold molecules: a platform for quantum simulation. *Quantum Science and Technology*, 4:014010, 2018.

[44] R. Barnett, D. Petrov, M. Lukin, and E. Demler. Quantum magnetism with multicomponent dipolar molecules in an optical lattice. *Physical review letters*, 96:190401, 2006.

[45] A. Micheli, G. Pupillo, H. P. Büchler, and P. Zoller. Cold polar molecules in two-dimensional traps: Tailoring interactions with external fields for novel quantum phases. *Physical Review A*, 76:043604, 2007.

[46] M. Ansmann, H. Wang, R. C. Bialczak, M. Hofheinz, E. Lucero, M. Neeley, A. D. O'Connell, D. Sank, M. Weides, and J. Wenner. Violation of bell's inequality in josephson phase qubits. *Nature*, 461:504, 2009.

[47] S. J. Weber, A. Chantasri, J. Dressel, A. N. Jordan, K. W. Murch, and I. Siddiqi. Mapping the optimal route between two quantum states. *Nature*, 511:570, 2014.

[48] I. M. Georgescu, S. Ashhab, and F. Nori. Quantum simulation. *Reviews of Modern Physics*, 86:153, 2014.

[49] L. K. Grover. Quantum mechanics helps in searching for a needle in a haystack. *Physical review letters*, 79:325, 1997.

[50] G. Brassard, I. Chuang, S. Lloyd, and C. Monroe. Quantum computing. *Proceedings of the National Academy of Sciences*, 95:11032–11033, 1998.

[51] A. Steane. Quantum computing. *Reports on Progress in Physics*, 61:117, 1998.

[52] D. DeMille. Quantum computation with trapped polar molecules. *Physical Review Letters*, 88:067901, 2002.

[53] M. Karra, K. Sharma, B. Friedrich, S. Kais, and D. Herschbach. Prospects for quantum computing with an array of ultracold polar paramagnetic molecules. *The Journal of chemical physics*, 144:094301, 2016.

[54] K. Ni, T. Rosenband, and D. D. Grimes. Dipolar exchange quantum logic gate with polar molecules. *Chemical science*, 9:6830–6838, 2018.

[55] S. Yelin, K. Kirby, and R. Cote. Schemes for robust quantum computation with polar molecules. *Physical Review A*, 74:050301, 2006.

[56] Z. Zhang and J. Liu. Quantum correlations and coherence of polar symmetric top molecules in pendular states. *Scientific reports*, 7:17822, 2017.

[57] A. Kantrowitz and J. Grey. A high intensity source for the molecular beam. part i. theoretical. *Review of Scientific Instruments*, 22:328–332, 1951.

[58] G. B. Kistiakowsky and W. P. Slichter. A high intensity source for the molecular beam. part ii. experimental. *Review of Scientific Instruments*, 22:333–337, 1951.

[59] W. Christen, K. Rademann, and U. Even. Efficient cooling in supersonic jet expansions of supercritical fluids: CO and CO^2. *The Journal of chemical physics*, 125:174307, 2006.

[60] R. deCarvalho, J. M. Doyle, B. Friedrich, T. Guillet, J. Kim, D. Patterson, and J. D. Weinstein. Buffer-gas loaded magnetic traps for atoms and molecules: A primer. *The European Physical Journal D-Atomic, Molecular, Optical and Plasma Physics*, 7:289–309, 1999.

[61] S. E. Maxwell, N. Brahms, R. deCarvalho, D. R. Glenn, J. S. Helton, S. V. Nguyen, D. Patterson, J. Petricka, D. DeMille, and J. M. Doyle. High-flux beam source for cold, slow atoms or molecules. *Physical review letters*, 95:173201, 2005.

[62] D. Patterson and J. M. Doyle. Bright, guided molecular beam with hydrodynamic enhancement. *The Journal of Chemical Physics*, 126:154307, 2007.

[63] H. Lu, J. Rasmussen, M. J. Wright, D. Patterson, and J. M. Doyle. Cold and slow molecular beam. *Physical chemistry chemical physics : PCCP*, 13:18986–90, 2011.

[64] N. R. Hutzler, H. Lu, and J. M. Doyle. The buffer gas beam: An intense, cold, and slow source for atoms and molecules. *Chemical Reviews*, 112:4803–4827, 2012.

[65] N. R. Hutzler, H. Lu, and J. M. Doyle. The buffer gas beam: an intense, cold, and slow source for atoms and molecules. *Chemical reviews*, 112:4803–4827, 2012.

[66] H. L. Bethlem, G. Berden, and G. Meijer. Decelerating neutral dipolar molecules. *Physical Review Letters*, 83:1558, 1999.

[67] S. Y. T. van de Meerakker, P. H. M. Smeets, N. Vanhaecke, R. T. Jongma, and G. Meijer. Deceleration and electrostatic trapping of oh radicals. *Physical review letters*, 94:023004, 2005.

[68] A. Osterwalder, S. A. Meek, G. Hammer, H. Haak, and G. Meijer. Deceleration of neutral molecules in macroscopic traveling traps. *Physical Review A*, 81:051401(R), 2010.

[69] S. A. Meek, H. Conrad, and G. Meijer. A stark decelerator on a chip. *New Journal of Physics*, 11:055024, 2009.

[70] S. A. Meek, H. L. Bethlem, H. Conrad, and G. Meijer. Trapping molecules on a chip in traveling potential wells. *Physical review letters*, 100:153003, 2008.

[71] S. A. Meek, H. Conrad, and G. Meijer. Trapping molecules on a chip. *Science*, 324:1699, 2009.

[72] N. Vanhaecke, U. Meier, M. Andrist, B. H. Meier, and F. Merkt. Multistage zeeman deceleration of hydrogen atoms. *Physical Review A*, 75:031402(R), 2007.

[73] E. Narevicius, A. Libson, C. G. Parthey, I. Chavez, J. Narevicius, U. Even, and M. G. Raizen. Stopping supersonic beams with a series of pulsed electromagnetic coils: an atomic coilgun. *Physical review letters*, 100:093003, 2008.

[74] E. Narevicius, A. Libson, C. Parthey, I. Chavez, J. Narevicius, U. Even, and M. Raizen. Stopping supersonic oxygen with a series of pulsed electromagnetic coils: A molecular coilgun. *Physical Review A*, 77:051401, 2008.

[75] E. Narevicius and M. G. Raizen. Toward cold chemistry with magnetically decelerated supersonic beams. *Chemical Reviews*, 112:4879–4889, 2012.

[76] N. Akerman, M. Karpov, L. David, E. Lavert-Ofir, J. Narevicius, and E. Narevicius. Simultaneous deceleration of atoms and molecules in a supersonic beam. *New Journal of Physics*, 17:065015, 2015.

[77] R. Fulton, A. I. Bishop, and P. F. Barker. Optical stark decelerator for molecules. *Physical review letters*, 93:243004, 2004.

[78] A. I. Bishop, L. Wang, and P. F. Barker. Creating cold stationary molecular gases by optical stark deceleration. *New Journal of Physics*, 12:073028, 2010.

[79] P. S. Żuchowski, J. Aldegunde, and J. M. Hutson. Ultracold rbsr molecules can be formed by magnetoassociation. *Physical review letters*, 105:153201, 2010.

[80] D. A. Brue and J. M. Hutson. Magnetically tunable feshbach resonances in ultracold Li-Yb mixtures. *Physical review letters*, 108:043201, 2012.

[81] D. A. Brue and J. M. Hutson. Prospects of forming ultracold molecules in $^2\Sigma$ states by magnetoassociation of alkali-metal atoms with Yb. *Physical Review A*, 87:052709, 2013.

[82] C. Chin, R. Grimm, P. Julienne, and E. Tiesinga. Feshbach resonances in ultracold gases. *Reviews of Modern Physics*, 82:1225, 2010.

[83] C. Wu, J. W. Park, P. Ahmadi, S. Will, and M. W. Zwierlein. Ultracold fermionic feshbach molecules of na 23 k 40. *Physical review letters*, 109:085301, 2012.

[84] M. Heo, T. T. Wang, C. A. Christensen, T. M. Rvachov, D. A. Cotta, J. Choi, Y. Lee, and W. Ketterle. Formation of ultracold fermionic nali feshbach molecules. *Physical Review A*, 86:021602, 2012.

[85] J. J. Zirbel, K. Ni, S. Ospelkaus, J. P. D'Incao, C. E. Wieman, J. Ye, and D. S. Jin. Collisional stability of fermionic feshbach molecules. *Physical review letters*, 100:143201, 2008.

[86] G. Thalhammer, M. Theis, K. Winkler, R. Grimm, and J. H. Denschlag. Inducing an optical feshbach resonance via stimulated raman coupling. *Physical Review A*, 71:033403, 2005.

[87] H. Yang, D. Zhang, L. Liu, Y. Liu, J. Nan, B. Zhao, and J. Pan. Observation of magnetically tunable feshbach resonances in ultracold $^{23}Na^{40}K +^{40}K$ collisions. *Science*, 363:261–264, 2019.

[88] K. Ni, S. Ospelkaus, M. H. G. De Miranda, A. Pe'Er, B. Neyenhuis, J. J. Zirbel, S. Kotochigova, P. S. Julienne, D. S. Jin, and J. Ye. A high phase-space-density gas of polar molecules. *Science*, 322:231–235, 2008.

[89] F. Lang, K. Winkler, C. Strauss, R. Grimm, and J. H. Denschlag. Ultracold triplet molecules in the rovibrational ground state. *Physical Review Letters*, 101:133005, 2008.

[90] J. G. Danzl, M. J. Mark, E. Haller, M. Gustavsson, R. Hart, J. Aldegunde, J. M. Hutson, and H. Nägerl. An ultracold high-density sample of rovibronic ground-state molecules in an optical lattice. *Nature Physics*, 6:265, 2010.

[91] T. Takekoshi, L. Reichsöllner, A. Schindewolf, J. M. Hutson, C. R. Le Sueur, O. Dulieu, F. Ferlaino, R. Grimm, and H. Nägerl. Ultracold dense samples of dipolar RbCs molecules in the rovibrational and hyperfine ground state. *Physical review letters*, 113:205301, 2014.

[92] P. K. Molony, P. D. Gregory, Z. Ji, B. Lu, M. P. Köppinger, C. R. Le Sueur, C. L. Blackley, J. M. Hutson, and S. L. Cornish. Creation of ultracold $^{87}Rb^{133}Cs$ molecules in the rovibrational ground state. *Physical review letters*, 113:255301, 2014.

[93] J. W. Park, S. A. Will, and M. W. Zwierlein. Ultracold dipolar gas of fermionic $^{23}Na^{40}K$ molecules in their absolute ground state. *Physical review letters*, 114:205302, 2015.

[94] M. Guo, B. Zhu, B. Lu, X. Ye, F. Wang, R. Vexiau, N. Bouloufa-Maafa, G. Quéméner, O. Dulieu, and D. Wang. Creation of an ultracold gas of ground-state dipolar $^{23}Na^{87}Rb$ molecules. *Physical review letters*, 116:205303, 2016.

[95] T. M. Rvachov, H. Son, A. T. Sommer, S. Ebadi, J. J. Park, M. W. Zwierlein, W. Ketterle, and A. O. Jamison. Long-lived ultracold molecules with electric and magnetic dipole moments. *Physical review letters*, 119:143001, 2017.

[96] G. Reinaudi, C. B. Osborn, M. McDonald, S. Kotochigova, and T. Zelevinsky. Optical production of stable ultracold $^{88}Sr_2$ molecules. *Physical review letters*, 109:115303, 2012.

[97] D. Wang, J. Qi, M. F. Stone, O. Nikolayeva, H. Wang, B. Hattaway, S. D. Gensemer, P. L. Gould, E. E. Eyler, and W. C. Stwalley. Photoassociative production and trapping of ultracold krb molecules. *Physical review letters*, 93:243005, 2004.

[98] S. Dutta, J. Lorenz, A. Altaf, D. S. Elliott, and Y. P. Chen. Photoassociation of ultracold lirb* molecules: observation of high efficiency and unitarity-limited rate saturation. *Physical Review A*, 89:020702, 2014.

[99] K. M. Jones, E. Tiesinga, P. D. Lett, and P. S. Julienne. Ultracold photoassociation spectroscopy: Long-range molecules and atomic scattering. *Reviews of Modern Physics*, 78:483, 2006.

[100] J. Deiglmayr, A. Grochola, M. Repp, K. Mörtlbauer, C. Glück, J. Lange, O. Dulieu, R. Wester, and M. Weidemüller. Formation of ultracold polar molecules in the rovibrational ground state. *Physical review letters*, 101:133004, 2008.

[101] M. D. Di Rosa. Laser-cooling molecules. *The European Physical Journal D-Atomic, Molecular, Optical and Plasma Physics*, 31:395–402, 2004.

[102] V. Zhelyazkova, A. Cournol, T. E. Wall, A. Matsushima, J. J. Hudson, E. A. Hinds, M. R. Tarbutt, and B. E. Sauer. Laser cooling and slowing of caf molecules. *Physical Review A*, 89:053416, 2014.

[103] L. Anderegg, B. L. Augenbraun, Y. Bao, S. Burchesky, L. W. Cheuk, W. Ketterle, and J. M. Doyle. Laser cooling of optically trapped molecules. *Nature Physics*, n:n, 2018.

[104] H. J. Williams, L. Caldwell, N. J. Fitch, S. Truppe, J. Rodewald, E. A. Hinds, B. E. Sauer, and M. R. Tarbutt. Magnetic trapping and coherent control of laser-cooled molecules. *Physical review letters*, 120:163201, 2018.

[105] L. Anderegg, B. L. Augenbraun, E. Chae, B. Hemmerling, N. R. Hutzler, A. Ravi, A. Collopy, J. Ye, W. Ketterle, and J. M. Doyle. Radio frequency magneto-optical trapping of caf with high density. *Physical review letters*, 119:103201, 2017.

[106] S. Truppe, H. J. Williams, M. Hambach, L. Caldwell, N. J. Fitch, E. A. Hinds, B. E. Sauer, and M. R. Tarbutt. Molecules cooled below the doppler limit. *Nature Physics*, 13:1173, 2017.

[107] J. F. Barry, D. J. McCarron, E. B. Norrgard, M. H. Steinecker, and D. DeMille. Magneto-optical trapping of a diatomic molecule. *Nature*, 512:286, 2014.

[108] E. S. Shuman, J. F. Barry, and D. DeMille. Laser cooling of a diatomic molecule. *Nature*, 467:820, 2010.

[109] E. S. Shuman, J. F. Barry, D. R. Glenn, and D. DeMille. Radiative force from optical cycling on a diatomic molecule. *Physical review letters*, 103:223001, 2009.

[110] J. F. Barry, E. S. Shuman, E. B. Norrgard, and D. DeMille. Laser radiation pressure slowing of a molecular beam. *Physical review letters*, 108:103002, 2012.

[111] M. T. Hummon, M. Yeo, B. K. Stuhl, A. L. Collopy, Y. Xia, and J. Ye. 2d magneto-optical trapping of diatomic molecules. *Physical review letters*, 110:143001, 2013.

[112] A. L. Collopy, S. Ding, Y. Wu, I. A. Finneran, L. Anderegg, B. L. Augenbraun, J. M. Doyle, and J. Ye. 3d magneto-optical trap of yttrium monoxide. *Physical review letters*, 121:213201, 2018.

[113] E. R. Hudson. Sympathetic cooling of molecular ions with ultracold atoms. *EPJ Techniques and Instrumentation*, 3:8, 2016.

[114] P. Soldán and J. M. Hutson. Interaction of $NH(X^3\Sigma^-)$ molecules with rubidium atoms: Implications for sympathetic cooling and the formation of extremely polar molecules. *Physical review letters*, 92:163202, 2004.

[115] M. L. González-Martínez and J. M. Hutson. Ultracold hydrogen atoms: a versatile coolant to produce ultracold molecules. *Physical review letters*, 111:203004, 2013.

[116] J. Lim, M. D. Frye, J. M. Hutson, and M. R. Tarbutt. Modeling sympathetic cooling of molecules by ultracold atoms. *Physical Review A*, 92:053419, 2015.

[117] M. Morita, M. B. Kosicki, P. S. Żuchowski, and T. V. Tscherbul. Atom-molecule collisions, spin relaxation, and sympathetic cooling in an ultracold spin-polarized $Rb(^2S)$-$SrF(^2\Sigma^+)$ mixture. *Physical Review A*, 98:042702, 2018.

[118] S. Hoekstra, J. J. Gilijamse, B. Sartakov, N. Vanhaecke, L. Scharfenberg, S. Y. T. van de Meerakker, and G. Meijer. Optical pumping of trapped neutral molecules by blackbody radiation. *Physical review letters*, 98:133001, 2007.

[119] S. Schlunk, A. Marian, P. Geng, A. P. Mosk, G. Meijer, and W. Schöllkopf. Trapping of Rb atoms by ac electric fields. *Physical review letters*, 98:223002, 2007.

[120] T. Rieger, P. Windpassinger, S. A. Rangwala, G. Rempe, and P. W. H. Pinkse. Trapping of neutral rubidium with a macroscopic three-phase electric trap. *Physical review letters*, 99:063001, 2007.

[121] J. van Veldhoven, H. L. Bethlem, and G. Meijer. Ac electric trap for ground-state molecules. *Physical review letters*, 94:083001, 2005.

[122] J. J. Gilijamse, S. Hoekstra, S. A. Meek, M. Metsälä, S. Y. T. van de Meerakker, G. Meijer, and G. C. Groenenboom. The radiative lifetime of metastable CO ($a^3\Pi$, $v = 0$). *The Journal of Chemical Physics*, 127:221102, 2007.

[123] J. H. Blokland, J. Riedel, S. Putzke, B. G. Sartakov, G. C. Groenenboom, and G. Meijer. Producing translationally cold, ground-state CO molecules. *The Journal of Chemical Physics*, 135:114201, 2011.

[124] D. H. Phelps. *Stark effect on emission spectra of diatomic molecules.* PhD thesis, University of British Columbia, 1966.

[125] B. G. Wicke, R. W. Field, and W. Klemperer. Fine structure, dipole moment, and perturbation analysis of $a^3\Pi$ CO*. *The Journal of Chemical Physics*, 56:5758, 1972.

[126] J. M. Brown and A. Carrington. *Rotational Spectroscopy of Diatomic Molecules.* Cambridge University Press, 2003.

[127] H. Lefebvre-Brion and R. W. Field. *The Spectra and Dynamics of Diatomic Molecules.* Academic Press, 2004.

[128] M. Semenov, S. Yurchenko, and J. Tennyson. Predicted landé g-factors for open shell diatomic molecules. *Journal of Molecular Spectroscopy*, 330:57 – 62, 2016.

[129] J. A. Gray, M. Li, and R. W. Field. Zeeman spectroscopy and deperturbation of the low-lying states of NiH. *The Journal of Chemical Physics*, 92:4651–4659, 1990.

[130] C. Cohen-Tannoudji, J. Dupont-Roc, and G. Grynberg. *Atom-photon interactions: basic processes and interactions.* 1998.

[131] G. Scoles. *Atomic and molecular beam methods.* 1988.

[132] R. C. Campargue. *Atomic and Molecular Beams, the State of the Art 2000.* 2001.

[133] H.G. Bennewitz and G. Buess. Vibrational relaxation in seeded beams. *Chemical Physics*, 28:175 – 185, 1978.

[134] G. M. McClelland, K. L. Saenger, J. J. Valentini, and D. R. Herschbach. Vibrational and rotational relaxation of iodine in seeded supersonic beams. *The Journal of Physical Chemistry*, 83:947–959, 1979.

[135] T. E. Wall. Preparation of cold molecules for high-precision measurements. *Journal of Physics B: Atomic, Molecular and Optical Physics*, 49:243001, 2016.

[136] G. Sanna and G. Tomassetti. *Introduction to Molecular Beams Gas Dynamics.* 2005.

[137] A. J. de Nijs, E. J. Salumbides, K. S. E. Eikema, W. Ubachs, and H. L. Bethlem. Uv-frequency metrology on CO ($a^3\Pi$): Isotope effects and sensitivity to a variation of the proton-to-electron mass ratio. *Physical Review A*, 84:052509, 2011.

[138] S. Marx, D. Adu Smith, M. J. Abel, T. Zehentbauer, G. Meijer, and G. Santambrogio. Imaging cold molecules on a chip. *Physical review letters*, 111:243007, 2013.

[139] S. Marx, D. Adu Smith, G. Insero, S. A. Meek, B. G. Sartakov, G. Meijer, and G. Santambrogio. Measuring and manipulating the temperature of cold molecules trapped on a chip. *Physical Review A*, 92:063408, 2015.

[140] S. A. Meek. *A Stark Decelerator on a Chip.* Phd thesis, Fritz-Haber-Institut, Freien Universität Berlin, 2010.

[141] S. A. Meek, G. Santambrogio, B. Sartakov, H. Conrad, and G. Meijer. Suppression of nonadiabatic losses of molecules from chip-based microtraps. *Physical Review A*, 83:033413, 2011.

[142] R. W. Field, O. Benoist d'Azy, M. Lavollée, R. LopezâDelgado, and A. Tramer. Radiative decay rates from deperturbed v=0–7 vibrational levels of CO $A^1\Pi$ measured using synchrotron radiation. *The Journal of Chemical Physics*, 78:2838, 1983.

[143] A. Hanssona and J. K. G. Watson. A comment on Hönl-London factors. *Journal of Molecular Spectroscopy*, 2333:169, 2005.

[144] W. Rijks and P. E. S. Wormer. Correlated van der waals coefficients. ii. dimers consisting of CO, HF, H_2O, and NH_3. *The Journal of Chemical Physics*, 90:6507–6519, 1989.